School of Physical and Chemical Sciences
University of Canterbury, Private Bag 4800
Christchurch, New Zealand

ASTR 690 MSc Thesis

submitted in partial fulfillment of the requirements for

The Degree of Master of Science in Astronomy

Ca II absorption in the circumstellar disk of β Pic

---

by

Harshil Gulati

Supervisor: Associate Prof. Karen Pollard

June 18, 2019

Abstract

Presented in this thesis is an analysis of absorption features identified in Ca II H & K absorption profiles obtained via observations taken of β Pic at the University of Canterbury Mount John Observatory (UC MJO) using the 1.0m McLellan telescope equipped with the HERCULES spectrograph and the Fairchild 486 back-illuminated CCD in 2017.

This study mainly focused on analysing the absorptions identified across 2017 by analysing the median spectrum for a night. However, for the specific night of the 3^{rd} of December 2017, the sequence of spectra obtained on the night were fitted individually to gain an insight into the variability of the different features throughout the course of the night.

Significant activity was observed, with the bulk of the spectra containing absorptions in a number of different velocity regimes, confirming the clumpy nature of the orbiting gas. A large number of blue-shifted features with a range of velocities were observed, while some features with high blue-shift velocities (< -40 km s^{-1}) were also observed which could last over several successive days. Low velocity features (LVFs; $v < 40$ km s^{-1}), which were responsible for an asymmetric broadening of the stable, deep circumstellar feature, were observed on successive nights. This supported the predictions of the "Falling Evaporating Bodies" (FEB) scenario by Beust et al.(1990) [1] regarding the long possible lifetime of the LVFs (on the order of days). While several high velocity features (HVFs; $v > 40$ km s^{-1}) were identified, only one HVF was identified on two consecutive nights (on the 5^{th} December to 6^{th} December 2017) with sufficiently close radial velocities and widths (measured by the Full Width at Half Maximum (FWHM)). This feature is not well-explained by the FEB scenario. The HVFs identified on the night of 3^{rd} of December 2017 were present throughout the course of the night which supported the FEB model's prediction that HVFs have a lifetime on the order of hours.

The predictions of the FEB scenario were also supported in regards to the expected increase in the FWHM of the features with an increase in radial velocity and also the expected decrease in the depths of the features with an increase in radial velocity. These results agreed well with similar studies carried out by previous authors such as Lagrange-Henri et al. (1996) [2], Petterson et al. (1999) [3] and Persson et al. (1998) [4] as was discussed by these authors. It was found that the LVFs ($v < 40$ km s^{-1}) had the highest depths of the absorption features and also could have very

high coverage of the stellar disk, as shown by the high filling factors (approaching unity). Some features in the velocity regime ($40-60\ \mathrm{km\,s^{-1}}$) were also found to have high depths and filling factors. HVFs with velocities beyond $60\ \mathrm{km\,s^{-1}}$ were found to be restricted mainly to low depths. This agreed with the findings of Petterson et al. (1996) [5] and Persson et al. (1998) [4], but as some HVFs lying in the velocity range of $40-60\ \mathrm{km\,s^{-1}}$ were found to have high depths in this study, this did not agree with the published studies of Lagrange-Henri et al. (1996) [2] and Petterson et al. (1999) [3] who found all HVFs ($v > 40\ \mathrm{km\,s^{-1}}$) restricted to low depths. With the exception of the HVF which lasted on consecutive nights, the FEB scenario well explains most of the variable features observed.

A plot of the absorption depth against the surface ratio,α, produced by Kiefer et al. (2014) [6] claimed that there were two families of exocomets around β Pic. However, perhaps due to insufficient quality data, no major clustering of points was observed in our data based on the two depth regimes ($p_K < 0.4$ and $p_K > 0.4$) and we could not verify this aspect of the analysis by Kiefer et al. (2014).

Due to a predicted β Pic b Hill sphere transit event in 2017, predicted from April 2017 to January 2018 (Wang et al. 2016), Ca II H & K absorption profiles collected within this time period were analysed to look for any effects of this transit. It was hypothesised that the Hill sphere transit could have an impact on the depth of the circumstellar feature due to density variations of circumstellar material, or the frequency of exocometary transits due to perturbations induced by the gravitational field of the planet or the planet's possible satellites. However, no discernible effect was seen on the depth of the circumstellar feature when compared to the study conducted by Barnes et al. (2000) [7], or on the rate of exocometary transits when compared to the studies by Lagrange-Henri et al.(1996) [2],Barnes et al. (2000) [7] and Kiefer et al. (2014) [6] who conducted their studies when a β Pic b Hill sphere transit was not predicted.

Acknowledgements

I would like to thank Assoc. Prof. Karen Pollard for her supervision of this project, proof reading this thesis and helpful suggestions. I would also like to thank my parents for their continued love and support throughout my Master's studies. I would also like to offer my gratitude to Dr. Orlon Petterson for helping me with the necessary software installations on my computer without which this Thesis would not have been possible.

Contents

List of Figures

List of Tables

CHAPTER 1

Introduction

Since time immemorial, humankind has looked at the twinkling lights in night sky and wondered about them. A primary goal of modern astrophysics is understanding the origins and evolution of the sources of these lights called stars. Of particular interest in this thesis is the study of the circumstellar disks of young, low mass (≈ 1 $M_\odot$) stars such as β Pic which have conditions similar to that of the young Solar system, conditions which can allow planets such as the Earth to emerge which can support life as we know it.

1.1 Beta Pictoris

β Pictoris is the title member of the β Pictoris moving group, a group of stars that have roughly the same age and share a common motion through space. The β Pictoris moving group is home to at least 17 star systems with an approximate age of 20 million years [17] located within a distance of 51 pc from Earth, which makes them the closest group of young stars to the Earth. This, coupled with the presence of an assortment of dusty circumstellar disks around many of these stars, many of which have masses similar to that of the Sun, makes these stars, including β Pictoris, prime candidates for study of young stellar systems and for directly imaging extrasolar planets [18].

1.1.1 Evolutionary status and stellar parameters

Since the discovery of β Pictoris as an IR-excess star by the Infrared Astronomical satellite (IRAS) in 1984 [19], its evolutionary status and age has been a source of widespread interest and contention among astronomers. The debate on its age is fuelled by the fact that an observation of IR excess from a star is most likely the result of circumstellar dust, which indicates either a young star approaching or just past the zero age main sequence (ZAMS), or an evolved star at the asymptotic giant branch or at a later stage of its evolutionary life. In order to ascertain its true evolutionary stage, detailed observations and studies of the circumstellar disk have to be conducted. Several studies were initially conducted on the circumstellar disk but no definite conclusions were reached regarding the age of β Pic (Paresce et al. (1991) [20], Gerbaldi et al. (1993) [21], Holweger & Rentsch-Holm (1995) [22], Lanz et al.(1995) [23], Brunini & Benvenuto (1996) [24]). Paresce et al. (1991) [20] conclude that β Pic is a young dwarf A5 star, probably just arrived on the main sequence, and they provide an upper limit on the age of the star of 2×10^8 years ruling out the notion that it is an evolved star with a bipolar nebula [20]. On the other hand, Brunini et al.(1996) ruled out estimates of still relatively young ages for the star ($\approx 10^6$) and instead argued for a more evolved star at which outer giant planets should have almost completed their formation. This conclusion was based on the ability of the circumstellar disk to replenish itself due to the amount of dust produced by the evaporating comets and their analysis of the rate of events within the cometary hypothesis that would have been observed in the Solar system at different evolutionary stages [24].

The Hipparcos satellite (Crifo et al.(1997) [16]) made 102 observations of β Pictoris and the data obtained from the satellite provided a lower limit on the age of the system, while the distance, luminosity, position on the HR diagram, and circumstellar extinction have been more precisely evaluated. Table 1.1 shows the values for some of the parameters obtained by other authors prior to the data obtained using the Hipparcos satellite.

Table 1.1: Table showing the values obtained for some stellar parameters by authors before Crifo et al. (1997) [16]

Authors	π(mas)	σ_π(mas)	d(pc)	M_V
Van Altena et al. (1995)	60.1	10.6	$16.6^{+3.6}_{-2.5}$	$2.74^{+0.36}_{-0.42}$
Lanz et al. (1995)	61	19.4808	16.4	2.78
Hipp (Crifo et al., 1997)	51.87	0.51	$19.28^{+0.19}_{-0.19}$	$2.42^{+0.03}_{-0.02}$

This relatively new evaluation of the distance of β Pic had some consequences with respect to the Bright Star Catalogue value(d_{HR}) as all previous geometrical dimensions had to be multiplied by a factor of $\frac{d_{Hipp}}{d_{HR}} = 1.176$. Moreover, for estimation of the absolute magnitude and comparison with previous data, the flux emitted by the star must be multiplied by a factor of 1.38 as was performed by Crifo et al. (1997). In order to estimate the position of β Pic on the Hertzsprung Russell (H-R) diagram, Crifo et al.(1997) used evolutionary tracks for pre- and post-main sequence evolution by Palla & Stahler (1993) [8] and Schaller et al. (1992) [9](see Figure 1.1). Based on the uncertainties on their estimated values for the stellar parameters (some of which have been slightly improved upon since) and the evolutionary tracks, Crifo et al. (1997) estimated that β Pictoris is at the ZAMS, or extremely close to it, which is widely accepted today [17]. Hence, based on the position of the star on the H-R diagram and their estimated values for the stellar parameters, Crifo et al. (1997) estimated a lower limit on the age of β Pic of 8×10^6 years [16]. Since then, multiple authors (Zuckerman et al. (2001) [18],Ortega et al. (2002) [25],Binks et al. (2013) [26] and others) have attempted to obtain specific values for the age of β Pictoris and the β Pictoris moving group (BPMG) as a whole.

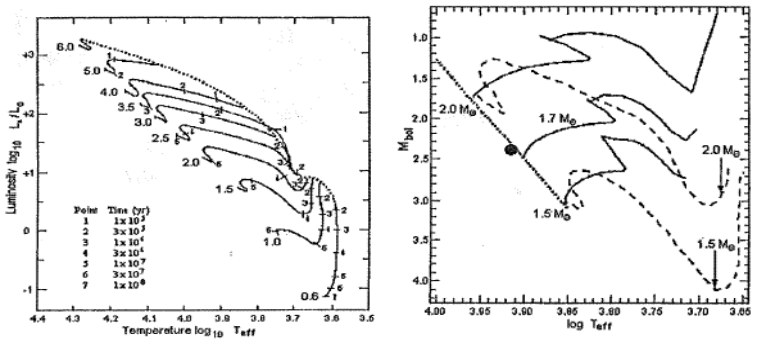

(a) (b)

Figure 1.1: *Plot (a) shows evolutionary tracks in the HR diagram, labelled by their solar masses, for pre-main sequence stars. The tick marks along the track indicate evolutionary times, starting from the birth-line (dotted curve) and ending at the ZAMS [8]. Plot (b) shows the region of (a) corresponding to the position of β Pic, shown as the large filled circle. The solid lines are the post-main sequence tracks [9], and the dashed lines the pre-main sequence tracks [8]*

As stars which are members of a moving group are estimated to have approximately the same age, astronomers have attempted to obtain ages of stars confirmed to be members of the BPMG to provide an approximate estimate on the age of β Pictoris. The various means by which they estimated the age of the BPMG included comparing the stars with known positions on the H-R diagram with theoretical isochrones to estimate their isochronal age [27], utilising obtained values for the Li depletion boundary amongst the different members [28] and also comparison with pre-MS evolutionary models [25]. Table 1.2 lists the various estimates for the age of BPMG obtained by different authors and the method used. The latest value of 22^{+3}_{-3} million years is provided by Mamajek et al. (2014) using a combination of the Li depletion boundary and isochronal age methods [17].

Table 1.2: *Table showing the estimated values for the age of BPMG by various authors [17]*

Reference –	Age (Myr)	Method –
Barrado y Navascués et al. (1999)	20 ± 10 Myr	CMD isochronal age (KM stars)
Zuckerman et al. (2001)	12^{+8}_{-4} Myr	H–R diagram isochronal age (GKM stars) + Li depletion
Ortega et al. (2002)	11.5 Myr	Traceback age
Song et al. (2003)	12 Myr	Traceback age
Ortega et al. (2004)	10.8 ± 0.3 Myr	Traceback age
Torres et al. (2006)	~18 Myr	Expansion age
Makarov (2007)	22 ± 12 Myr	Traceback age
Mentuch et al. (2008)	21 ± 9 Myr	Li depletion
Macdonald & Mullan (2010)	~40 Myr	Li depletion (magnetoconvection models)
Binks & Jeffries (2014)	21 ± 4 Myr	Li depletion boundary
Malo et al. (2014)	26 ± 3 Myr	Li depletion boundary
Malo et al. (2014)	21.5 ± 6.5 Myr (15–28 Myr)	H–R diagram isochronal age (KM stars)
This work	22 ± 3 Myr	CMD isochronal age (FG stars)
Final	**23 ± 3 Myr (1σ)** **[±2 Myr (statistical), ±2 Myr (systematic)]**	Li depletion boundary and isochronal age (FGKM stars)

Following the initial results published by Crifo et al. (1997) based on the Hipparcos data, updated values have since been obtained for the stellar parameters by other authors, while a re- reduction of the Hipparcos raw data by van Leeuwen et al. (2007) has resulted in more accurate values for some of the parameters such as the parallax, the distance to the star and the proper motion. Table 1.2 lists the values for the different stellar parameters along with the corresponding authors.

Table 1.3: Table showing the estimated values for the various stellar parameters of β Pic with the corresponding authors

Stellar Parameters for Beta Pictoris		
Name		β Pictoris
HR		2020
HD		39060
Parameter	**Value**	**Author(s)**
RA	$05^h47^m17.1^s$	Zuckerman et al.(2001)
Dec	-51° 04' 00"	Zuckerman et al.(2001)
Spectral type	A6V	Gray et al.(2006) [29]
Parallax (mas)	$51.44^{+0.12}_{-0.12}$	van Leeuwen, F. (2007) [30]
Distance (pc)	$19.44^{+0.05}_{-0.05}$	van Leeuwen, F. (2007) [30]
T_{eff}	8052 K	Gray et al.(2006)
Age	23^{+3}_{-3}	Mamajek et al.(2014)
Mass	1.7 - 1.8 $M_\odot$	Crifo et al.(1997)
Radius	1.7 - 1.8 $M_\odot$	Crifo et al.(1997)
log g	4.15 cgs	Gray et al.(2006)
Absolute magnitude, M_V	2.42	Crifo et al.(1997)
Bolometric magnitude	2.43	.Crifo et al.(1997)
V	3.85	Crifo et al.(1997)
B-V	+0.17	Crifo et al.(1997)
U-B	+0.10	Crifo et al.(1997)
Proper Motion(RA)	+4.65 mas/yr	van Leeuwen, F. (2007) [30]
Proper Motion(Dec)	+83.10 mas/yr	van Leeuwen, F. (2007) [30]
RV(km/s)	$20^{+0.7}_{-0.7}$	Gontcharov G.A. (2006) [31]
v sin i	130 km/s	Royer F et al. (2007) [32]

1.1.2 Model of the Circumstellar disk

One of the many exciting and largely unexpected discoveries of IRAS (Infrared Astronomical Satellite) has been the detection of disks of gas and dust around nearby stars, similar to what must have been present in the early solar system. β Pic is one of these stars which shows a substantial infrared excess in the IRAS passbands. This has been interpreted as being due to thermal radiation from dust, typically at a temperature of about 100 K, orbiting the star(Negebauer et al.(1984) [19],Aumann et al.(1985) [33]). Modelling of the IRAS data suggested that this disk is made up of particles ranging in

size from the μm domain to the mm domain (see the review by Artymowicz (1990) [34] and references therein). Electromagnetic radiation in the ultraviolet and visible regimes is absorbed by these dust particles causing their temperatures to rise. This warming releases large amounts of infrared radiation, which was easily detected by IRAS.

Follow up observations of β Pic in optical wavelengths by Smith and Terrile revealed that the dust particles are arranged geometrically in a disk seen almost edge on. Their observations also found that the surface density of the dust particles falls off following an inverse square law (r^{-2}), is optically thin, extends inward to about 30 A.U. (roughly the size of our solar system) and is relatively clear inside 30 A.U. By modelling how the surface brightness of the disk decreases as distance from the star (r) is increased, the authors also concluded that the distribution of mass per unit volume within the disk must be proportional to approximately r^{-3} beyond the range of their coronograph masks (r$\geq$ 100 A.U.) [35].

In later observations, Smith and Terrille (1987) [36], also traced the disk out to more than 1000 A.U. (before fading below detectability) and also noted that at about 300 A.U. the disk appears to be 50 A.U. thick. It was proposed by the same authors that the grains could be composed of silicates, carbonaceous material and ices. Indeed silicates were detected within this region ($\approx$ 30 A.U.) in a study conducted by Telesco et al. (1991) [37] who detected a broad 10 μm emission feature within 3" of the star which closely resembles silicate features observed in comets Halley and Kohoutek and in a variety of other sources. This suggested particle sizes of $\leq$ 1 μm close to the the star. After performing 8-13 μm spectroscopy of β Pic, Aitken et al. (1993) confirmed the presence of silicate emission in its infrared excess and placed an upper limit of 2-3 μm on the size of emitting dust particles, which is similar to cometary dust. They also noted that large particle sizes are required for the dust particles for orbital stability against radiation-pressure blow out or Poynting-Robertson drag [38]. However, in a study conducted by Backman et al.(1992), in which they performed infrared observations of β Pic at 10 and 20 microns and produced thermal models of the disk, they found that a significant proportion of the infrared excess is coming from a region between 4" and 8" (75 - 150 A.U.). As large grains yield a too-compact disk, small grains with sizes near 1 μm are required to account for a significant proportion of the infrared excess. Hence, these small particles must be replenished by collisions between larger bodies [39].

As the presence of silicate grains has been confirmed (≈ 3 μm) and coupled with the argument that collisions between larger bodies are needed to replenish the small particles within the disk, the disk must be a relatively evolved one in which large objects such as comets, planetesimals or even fully formed planets could exist. The model results by Backman et. al.(1992) also implied that a simple disk with a single power law spatial distribution is inconsistent with the combined optical and infrared data and they presented models with two structural components,r $>$ 80 A.U. and r $<$ 80 A.U., which were a better match to the observations, while their 10 μm observations implied that the inner component only extends to a limit of between 1 and 30 A.U. from the star, leaving an innermost void. In the outer region of the disk from $\approx$ 100 A.U. to 1000 A.U., polarisation observations ($\approx 17^{+3}_{-3}\%$) [40], as well as the known colours of the disk, suggested the presence of large (≥ 10 μm) dust grains within this region. This grain size is typical of that of cometary dust rather than interstellar dust, indicating that the dust is in some way processed (accretion or conversely evaporation), rather than resulting from stellar formation processes. Additional support for the presence of comets also comes from the detection of carbon monoxide absorption in the UV [41].

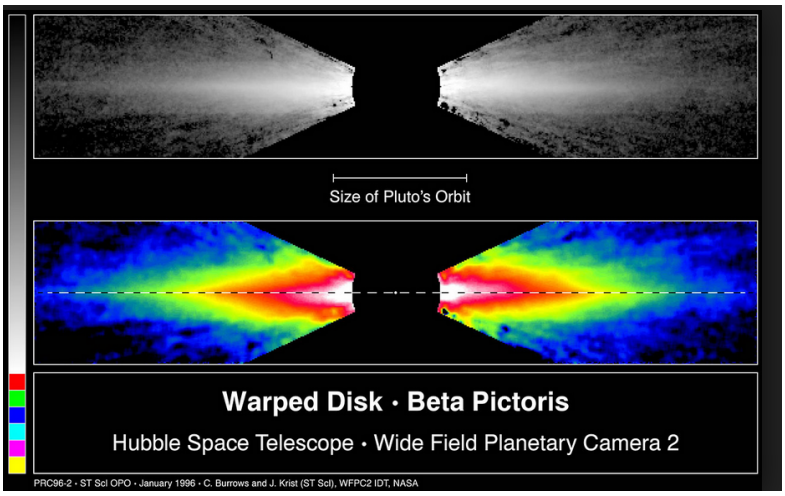

Figure 1.2: HST coronagraphic image of the circumstellar disk of β Pictoris which shows an S shaped warp, which is interpreted as the signature of planets closer to the star. Source:Burrows et al.(1995) [10]

Asymmetries in the circumstellar disk have also been reported in the literature at optical [42, 43] and infrared [44] wavelengths, as well as a 4° warp within 4" of the star

using the Hubble Space Telescope [10, 43, 45]. It has been observed that the disk is oriented in the northeast-southwest direction and the disk has been measured out to 1835 A.U. in the northeast direction and 1450 A.U. in the south west direction, further supporting the asymmetric nature of the disk [46]. The disk has also been found to be rotating, with the northeast part of the disk moving away from the Earth while the southeast part moving towards the Earth [47].

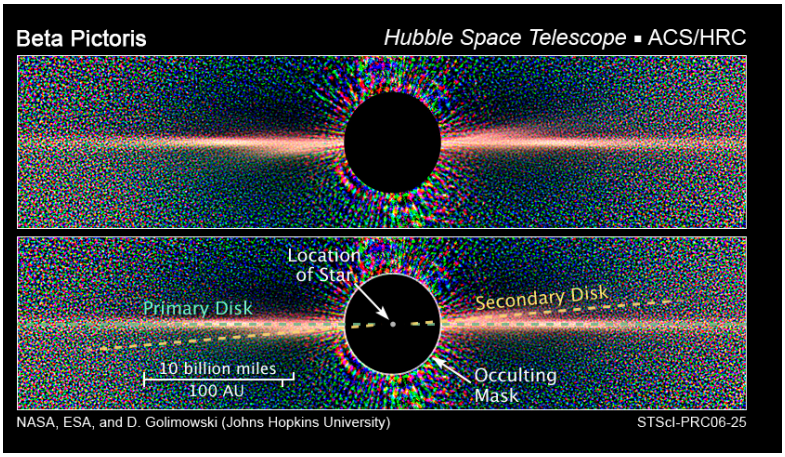

Figure 1.3: Latest Model of the β Pic Circumstellar disk according to HST observations in 2006.(Source: Golimowski et al.(2006)) [11]

Imaging of the system with the Hubble Space Telescope's Advanced Camera for Surveys in 2006, revealed the presence of a secondary dust disk inclined at an angle of about 5° to the main disk and extending at least 130 A.U. from the star. The secondary disk is also asymmetrical with the southwest extension being more curved and less inclined than the northeast [11].The imaging was not clear enough to distinguish between the main and the secondary disks within 80 A.U. of the star but the northeast extension has been predicted to intersect with the main disk at about 30 A.U. from the star. This two disk model for the β Pic circumstellar disk is widely accepted today [48].

1.2 Falling Evaporating Bodies Scenario

For more than thirty years, highly time variable and predominantly red-shifted absorption features have been observed in the absorption profiles of Ca II, Al III, Mg II and other metallic ions in the spectrum of β Pic [49]. These absorption features have since

been explained using the Falling Evaporating bodies (FEB) scenario, which suggested that these variations were the result of comet-like bodies passing our line of sight in front of the star. The edge-on orientation of the β Pic disk, coupled with the assumption that the comets are confined in the plane of the disk, provided credence to this explanation as these factors greatly increase the possibility of observation of a comet passing our line of sight. The explanation was not considered unreasonable as bodies in our own solar system such as the Moon, show evidence of craters and remnants which are due to intense bombardment of comets and meteorites during the early stages of planetary formation. Since the age of β Pic indicates that the system is in such an early stage of planetary formation, it must be undergoing intense bombardment of comets and planetesimals which makes the FEB scenario very appealing [1].

In 1989, Beust et al. developed a model of the FEB scenario to explain the cause of these spectroscopic variations [49]. It proposes that heating of the dust of the cometary body due to the stellar flux and subsequent evaporation and ionisation of the dust is the cause of these variations. As it was observed that the variations are predominantly red shifted, it implied that the orbiting material must be falling in towards the star, away from us, hence the name Falling Evaporating Bodies(FEB) scenario. For the purposes of this thesis, variable absorptions in the absorption profiles of Ca II ions were modelled and analysed, while variable absorptions in the absorption profiles of other moderately ionized metallic ions as Mg II, Al III and Fe II have also been observed which have also been interpreted as being due to infalling comet-like bodies. [50]

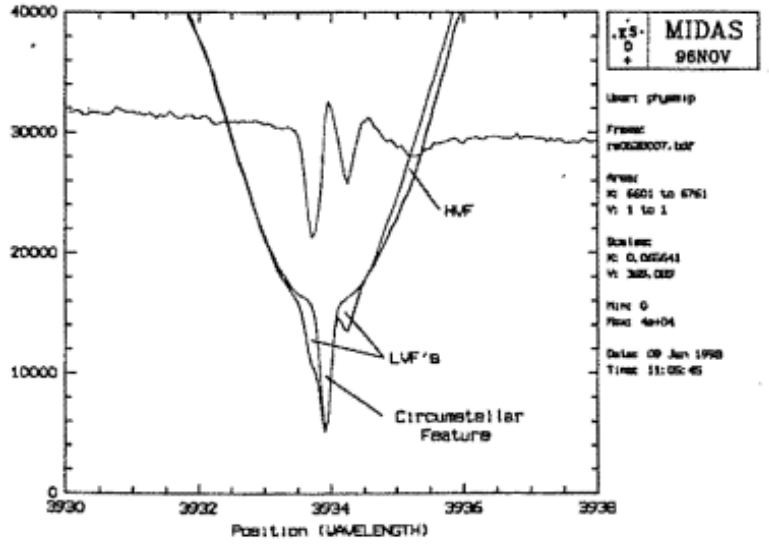

Figure 1.4: Figure showing the different types of variable absorption features observed in the Ca II absorption profiles. HVF and LVF refer to high velocity feature and low velocity feature respectively. Source:Persson et al.(1997) [4]

The three different types of features that have been observed are as follows:

- Central circumstellar feature at the radial velocity of the star;
- Low velocity features(LVFs) which tend to be narrow and deep absorption lines, (close to the central peak and which last from hours to weeks); and
- High Velocity features (HVFs) which tend to be broad and shallow absorption lines, far away from the central peak and which vary rapidly (over hours)

1.2.1 Modelling of the Falling Evaporating bodies scenario

The FEB scenario has been tested and modelled using Ca II profiles as performed by Beust et al.(1989-1991) [1, 49, 51] who simulated the evaporation of comet-like bodies grazing the star on parabolic orbits with a periastron of 5-30 $R_\star$ [49]. It was assumed by the authors that the observed variable features are produced by atoms or ions ejected with a velocity ν_e from the nucleus of the infalling body and moving in a surrounding gas of density n. In a first approximation, they assume that the cometary gas is spherical and there are three kinds of interactions that affect the ions in the gas:

- Gravitation - towards the star ;
- Radiation pressure away from the star due to the stellar flux ; and
- Collisions between the metallic ions and the hydrogen atoms in the cometary gas.

The authors assume that the cometary gas is spherical mainly due to the fact that the radiation pressure is not very efficient on the hydrogen ions, and the lack of appreciable stellar wind in A-type stars. (As stellar winds from normal A-type stars are usually very weak, their effects on ions or atoms are assumed to be negligible.)

One can then consider the density of the cometary gas as a function of four different parameters:

- The distance r between the comet and the star;
- The distance x between the considered point and the nucleus of the comet;
- The outflow velocity ν_e of hydrogen from the nucleus. The value of this parameter was assumed to be constant in their model and as using in situ measurements of comet Halley (Lammerzahl et al. (1987) [52]) in the solar system had given a value of $1^{+0.2}_{-0.2}$ km s^{-1} for water, the authors assumed a similar value for their model; and
- The hydrogen production rate z of the comet.

The authors chose to simulate the orbits of the comet-like bodies as parabolic due to their treatment of the infalling bodies as points that originate from the circumstellar disk which is itself quite distant from the star [1]. As the ions ejected from an infalling body move at relatively small velocities, it can be assumed that, in the absence of any other interactions, they would move towards the star at the free-fall velocity. However, the force induced on the ion or atom due to the stellar flux (radiation pressure) is in all cases larger than the effects of gravity, by a factor of up to 77.2 [1]. This factor has been revised downwards considerably by Lagrange et al.(1998) [53] for Ca II , but it is still much larger compared to other metallic ions. Hence, the ions are repelled away from the star as has been observed in orbiting comets. As the collisions which occur between the metallic ions and the hydrogen atoms can be modelled via the induced dipole effect and

are completely random, they act as an effective force against the velocity [49]. Hence, as a combination of the effects of radiation pressure and collisions, the velocity of the ion relative to the surrounding gas approaches a quantity termed the *limiting velocity* in a characteristic time τ. The expression for the limiting velocity is then applied as a correction by subtracting it from the free fall velocity of the surrounding gas. This correction relies on the assumption that the surrounding gas the ions are moving in is produced by the body itself, and is infalling with it. This assumption is necessary for producing red shifted features, since movement in a non-infalling gas (at low velocity) would only create blueshifted features [49].

By testing a range of values for the gas production rate and the periastron distances, synthetic spectra were produced which were in strong agreement with observed spectra both in the visible and UV wavebands. The only simulations that produced results similar to those observed required an inclination, (the angle between the axis of orbit and the line of sight), of i = $150^{+10}_{-10}{}^{\circ}$, and had periastron values of q = 5-30 $R_\star$ [1].

Low velocity features

The low velocity features (LVFs) are hypothesised to result from comet-like bodies passing through the line of sight at a distance of the order of $\approx 10\ R_\star$ from the star. It was found by Beust et al. (Paper X, 1990) [1] that the low velocity features of the modelled spectra were generally centred at a radial velocity between 0 and ≈ 40 kms^{-1} when using a value of inclination of -150 $^{\circ}$, and are generally narrow and deep.

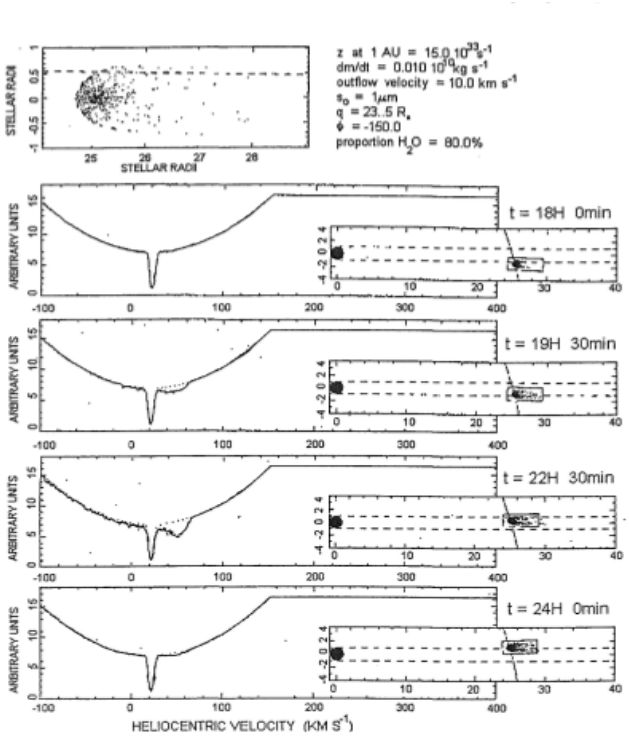

Figure 1.5: *Figure showing the evolution of a LVF as simulated using the specified values for the initial parameters. Each panel on the bottom right corner shows the extent of the ionic cloud as a function of stellar radius as it passes in front of the star.The panel shows that the time of crossing of the ionic cloud in front of the star is approximately equal to 4 hours in this case. Source: Beust et al.(1990) [1]*

Figure 1.5 shows a simulation of the temporal evolution of the line variation caused by a kilometre-sized body, at 23.5 $R_\star$, passing into our line of sight. The first appearance of an absorption occurs at 19H 30 min and by 24 H the depth of the absorption has declined considerably. This gives a typical time for a LVF to cross our line of sight of $\approx$ 4 hours. However many of the LVFs have been observed to last for much longer than 4 hours, on the order of days or even weeks.

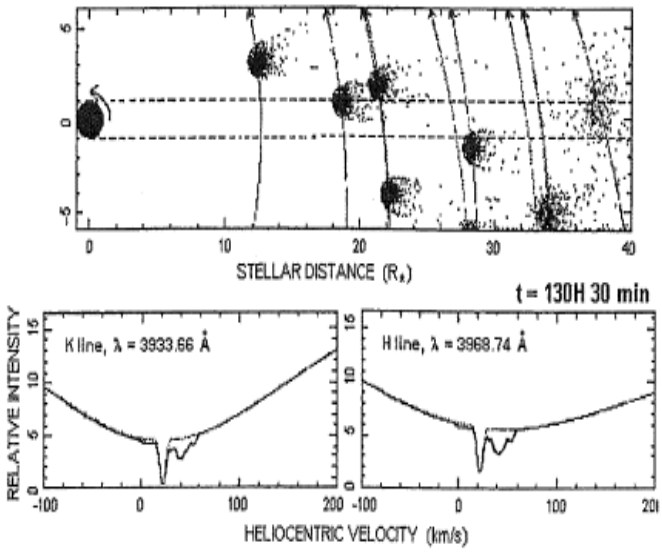

Figure 1.6: *Simulation of a stream of infalling comet-like bodies. The top panel shows a number of comet- like bodies crossing our line of sight (indicated by dashed lines) to the star(dark oval). The bottom panel shows the resulting multicomponent redshifted features, which are similar to those observed, and are due to the effect of several FEBs crossing our line of sight simultaneously.*

As a single infalling body cannot explain this observation, a series of infalling bodies with a range of periastrons was proposed (See Figure 1.6). Under this scenario a successive comet, not necessarily at the same periastron, also enters our line of sight before the remnant tail of the previous comet has been dispersed. This also explains the multiple structure that can be seen in some of the absorption features. These bodies do not need to fall in as a simple queue with the only constraint being the inclination of the line of sight [13]. Figure 1.5 shows the simulation results using a periastron value of 18 $R_\star$ which also matched well with the observed spectra.

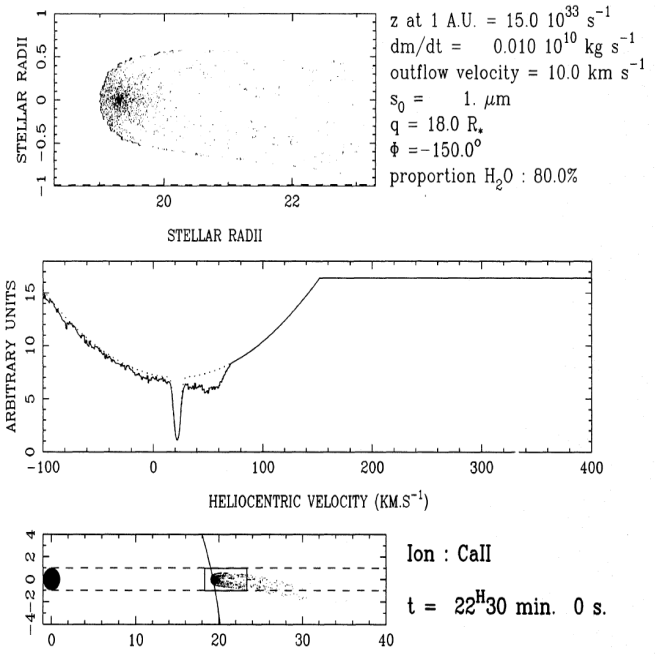

Figure 1.7: *Figure showing the simulation results for a value of q = 18.0 $R_\star$. Note the similar position and nature of the LVF as for the value of q = 23.5 $R_\star$(See Figure 1.5)*

High velocity features

Higher velocity features(HVFs) have also been observed in the absorption profiles of Ca II which are generally broader compared to the LVFs, and a model was developed and tested by Beust et al. (Paper XI, 1990) [51] to account for these features. It was pointed out in an earlier paper (Beust et al.(Paper X,1990)) [1] that the infalling bodies passing through the line of sight at a distance of less than 10 $R_\star$ should not produce detectable absorption features in Ca II lines. The main reason for that was that the much higher value of radiation pressure on Ca II at these stellar distances ($\approx$ 12.5 times stronger at 7 $R_\star$ than at 25 $R_\star$) prevents the Ca II cloud around the nucleus from reaching a large enough projected size on the stellar surface to produce detectable components. However, this assumption could only be partially true, since the production rate of an evaporating body is expected to increase towards smaller stellar distances. Increasing the production rate leads to more efficient collisions between the metallic ions and the H atoms, and therefore to a larger cloud.

In the same paper, the authors also showed that only varying the periastron had a

small effect on the red shift velocity of the Ca II absorption component. However, this was only valid in the periastron range where the absorption components are expected to be observed in Ca II ($10\ R_\star \leq$ q $\leq 30\ R_\star$) and it is due to the rather small variation of the free fall velocity in that range. In contrast, variations of the free fall velocity at smaller distances are more drastic, so without changing the inclination, a body passing through the line of sight closer to the star where the free fall velocity would be larger, could produce features with higher redshifts. As the radiation pressure on Ca II ions is higher at smaller distances and acts more efficiently, it could lead to a higher velocity dispersion for the ions, accounting for the fact that the HVFs are broader than the LVFs.

Finally, it was also argued that as the projected size of the Ca II cloud on the stellar surface would be smaller at the smaller distances and this could account for the smaller depth of the HVFs.

To check this hypothesis, a simulation with a periastron of q $= 5\ R_\star$ and gas and dust production rates four times larger than the values in (Beust et al.(1990)) was run and the synthetic spectrum obtained was found to be very close to the observed one, supporting the authors' hypothesis that the HVFs are the result of comet-like bodies passing our line of sight at periastrons of less than $\approx 10\ R_\star$. Figure 1.8 shows this simulation result with the used values of the initial parameters. Since the HVF absorptions are produced much closer to the star, their evolutionary timescale is much shorter. The smaller distance gives a far greater orbital velocity to the body and as such it crosses the line of sight more rapidly. Hence, the higher the redshift velocity, the shorter evolution timescale of the feature. It is therefore unlikely that another body will enter the line of sight during the crossing-time of the first body. Hence, the infalling shower of comets as proposed to account for the multiple structure of some LVFs, cannot be used to account for the continued presence of HVFs.

Within a distance of $\approx 10\ R_\star$, blue shifted features should also be able to be observed as were reported in late 1989 [13]. There were two different types of blue-shifted features observed: one narrow feature with a small blueshift velocity; and a broad feature at a high blueshift velocity. The narrow feature is the result of a larger inclination angle (angle between the line of sight and the axis of orbit of the comet) approximately equal to 180°.

However, the broad features can be interpreted in a different way. As radiation pressure acts on the Ca II ions, they begin to move away from the star and thus spread towards blueshifted velocities. The authors postulated that the broad features may be the result of absorption effects from the tail of an ionic cloud of an infalling body as it passes through our line of sight, while a deeper and sharper red-shifted component is produced by the head as it falls towards the star. This can be observed in Figure 1.8, which shows a shallow red-shifted feature due to the head of the infalling body moving away from us. If the ejection and dispersion velocities of the Ca II ions are large enough, this can result in the production of visible noisy blue-shifted features [13]. The constraint on the value of the inclination and the predominance of red-shifted features showed that the infalling bodies must be arriving onto the line of sight from a precise direction in the circumstellar disk. As will be discussed briefly in the Section 1.3, it was proposed by the authors [1] that the constraint on the value of inclination can be explained by the existence of planetary sized objects in the disk perturbing the orbits of comets whose orbital parameters must be more randomized.

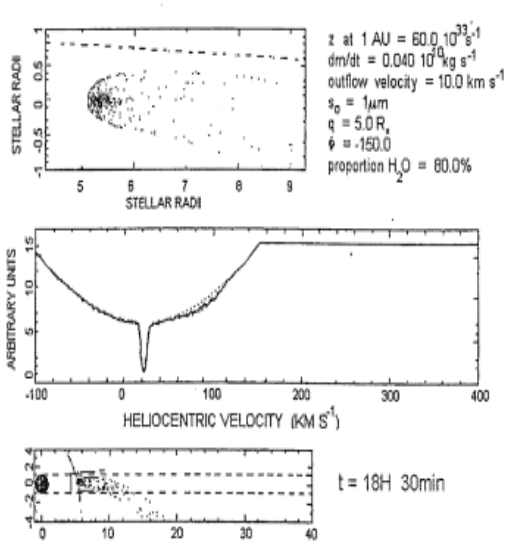

Figure 1.8: *Figure showing the simulation results for a value of* $q = 5\ R_\star$.

1.2.2 Filling Factors

A useful parameter that can be evaluated by simultaneous measurements of the peak depths of the absorption features in both the Ca II H & K lines is the filling factor, α. Even if a line is saturated, it doesnot reach zero intensity because the ionic cloud associated with the exocomet doesnot occult the entire proportion of the stellar disk. For saturated lines, α can be easily and well determined but for weak and unsaturated lines, only a lower limit on the size of the obscuration can be derived. This is due to the different oscillator strengths of the H & K lines. The oscillator strength, also called the f-value, is different for each atomic transition and is related to the atomic transition probability which is the probability of transition of an electron between two specific energy levels [54].

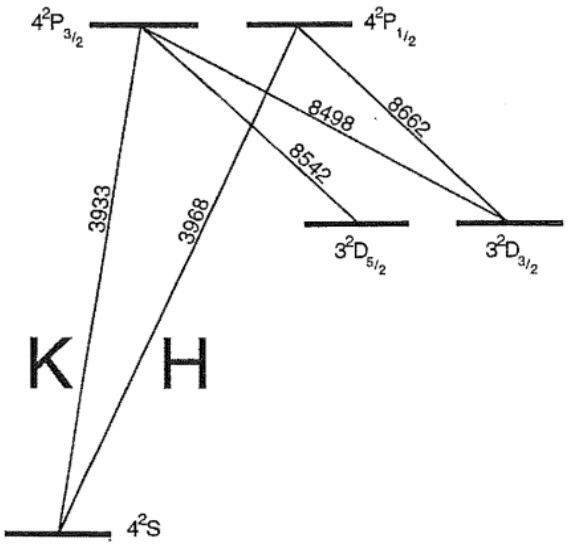

Figure 1.9: *Energy levels of the Ca II H & K lines. The transition wavelengths in Å are indicated. Source: L Haller et al.(1963) [12]*

Figure 1.9 shows the energy level structure for Ca II H & K lines. In Ca II, the ^2D energy level is metastable and atoms typically get there by transitions to the ^2P level, via either an H or K excitation, followed by an infrared cascade down to the ^2D level [12]. The oscillator strength of the K line (0.69) is almost twice as strong as for the H line (0.344) meaning the K transition is twice as likely as the H transition and hence, the

strength of any K line absorption should be twice as that of any H line absorption in the case of optically thin lines. Since the flux decreases exponentially through the ionic cloud, and p_H and p_K are measurements of how much flux has been absorbed at 3968.470 Å and 3933.664 Å respectively, relations can be obtained for p_H and p_K as functions of their optical depths τ_H and τ_K respectively. The optical depths are defined in physics as the ratio of the incident to the transmitted radiant power through a material. As the K line has twice the oscillator strength of the H line, it will have twice the optical depth as the H line, $\tau_K = 2\tau_H$. If α is the ratio of the size of the ionic cloud to the area of the stellar disk (the filling factor), then the depths of the H and K lines can be calculated. Assuming the stellar disk is uniform, the total flux from the star is F_λ and with a cloud of ions occulting the disk, the total transmitted flux of the star, F_t, can be written as :

$$F_t = F_\lambda(1-\alpha) + F_\lambda \alpha e^{-\tau} \tag{1.1}$$

Factorizing the above expression,

$$F_t = F_\lambda(1-\alpha+\alpha e^{-\tau}) \tag{1.2}$$

where τ is the optical depth. Therefore the depths of the H and K lines relative to the continuum can be given by:

$$p = \frac{F_\lambda - F_t}{F_\lambda} \tag{1.3}$$

which upon substitution of the expression for F_t from Equation 1.2 and simplifying reduces into :

$$\begin{aligned} p &= 1 - [1 - \alpha + \alpha.e^{-\tau}] \\ &= \alpha(1 - e^{-\tau}) \end{aligned} \tag{1.4}$$

In terms of the H and K lines, this becomes,

$$p_H = \alpha.(1-e^{-\tau}); p_K = \alpha.(1-e^{-2\tau}) \tag{1.5}$$

where τ is the optical depth of the H line. Elimination of $e^{-\tau}$ from the above two expressions by solving for τ allows an expression for α in terms of the H and K line depths:

$$\alpha = \frac{p_H^2}{2p_H - p_K} \tag{1.6}$$

Rearranging Equation 1.6 and solving for p_K allows an expression for p_K in terms of a fixed value of α and varying values of p_H as shown in the following Equation:

$$p_K = \frac{2\alpha p_H - p_H^2}{\alpha} \tag{1.7}$$

Equation 1.7 allows plotting of iso-α curves for any specific value of α in the (p_H, p_K) plane. Equation 1.5 also allows an expression to be obtained for the ratio p_K/p_H by dividing the two expressions for depths in the two lines, which eliminates α and results in the following expression :

$$\frac{p_K}{p_H} = 1 + e^{-\tau/2} \tag{1.8}$$

Solving Equation 1.8 for τ allows an expression to be obtained for the optical depth resulting in the following expression:

$$\tau \ = -2 \times \ln(\frac{p_K}{p_H} - 1) \tag{1.9}$$

Theoretically Equation 1.6 allows α to be measured in any case. However, a more illuminating approach is to find a graphical solution to α by plotting iso-α curves in the (p_H, p_K) plane by using Equation 1.7 for different chosen values of α from optically thin (weak) to saturated (strong) lines shown by Figure 1.10. The iso-α curves are perpendicular to the iso-optical depth lines and hence each point between the optically thin and thick lines, is a function of the optical depth and the filling factor, with each position corresponding to a unique value of the optical depth, τ and the filling factor, α. The plots are limited by two cases: when $p_H \approx p_K$ in case of strong, saturated lines and when $p_K \approx 2 \times p_H$ for weak, unsaturated lines.

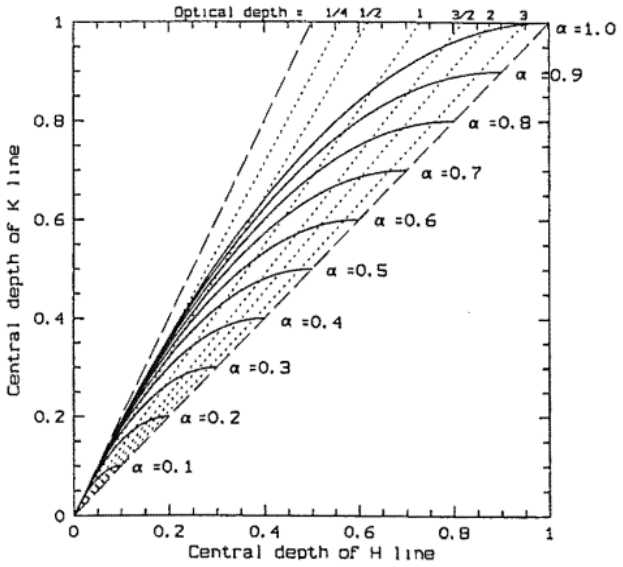

Figure 1.10: *Figure showing the iso-alpha lines in the pH-pK plane plotted between the optically thick and optically thin limits (shown by the dashed lines). The dotted lines between the limits show regions of constant values for optical depths,(τ). Source: Lagrange-Henri et al.(1992) [13]*

As Figure 1.10 shows, α can be easily determined for saturated lines, but not so easily for unsaturated lines, because at low optical depths the iso-α lines are close together. This means it is not possible to distinguish between weak, optically deep lines from a cloud covering a small part of the stellar surface, from optically deeper (higher value for τ), but still weak lines from a cloud covering a smaller part of the star. This serves as an explanation for why it is only possible to obtain a lower limit on the value of α for unsaturated lines.

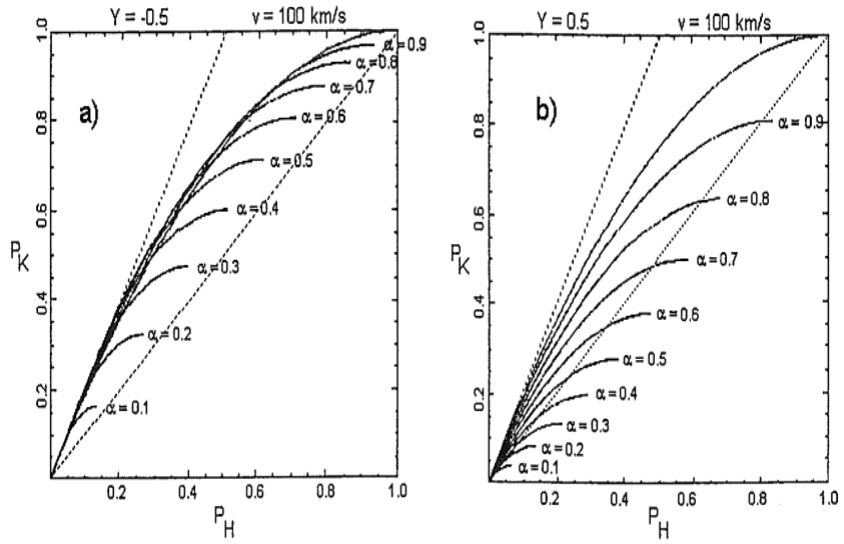

Figure 1.11: *Figures showing the iso-alpha curves taking into account the rotation of the star. Figures 1.11 (a) and (b) show the effect on the iso-alpha curves as a result of the ionic cloud occulting a star rotating towards and away from us respectively. Source: Lagrange-Henri et al.(1996) [2]*

Figure 1.10 shows the iso-α curves for a non-rotating star [2]. However, when consideration is made for the rotation of the star, a number of differences occur as shown in Figure 1.11. Depending on which side of the star the cloud of ions is occulting, differences in the Doppler shifting of the H and K lines arise [14]. When the cloud occults the portion of the star rotating towards us, the wavelengths are shortened (blue-shifted), having the effect of moving the iso-α curves more towards the optically thin ($p_K \approx 2 \times p_H$ region of the graph). In the case of the cloud occulting the portion of the star rotating away from us, Doppler shifting results in longer wavelengths (red-shifted) moving the iso-α curves more towards the saturated $p_K \approx p_H$ region of the graph. This is of particular interest since, as can be seen in Figure 1.11, the curves extend beyond the limit of $p_H = p_K$, therefore implying that p_H can exceed p_K despite the H line oscillator strength being only half that of the K line [14].

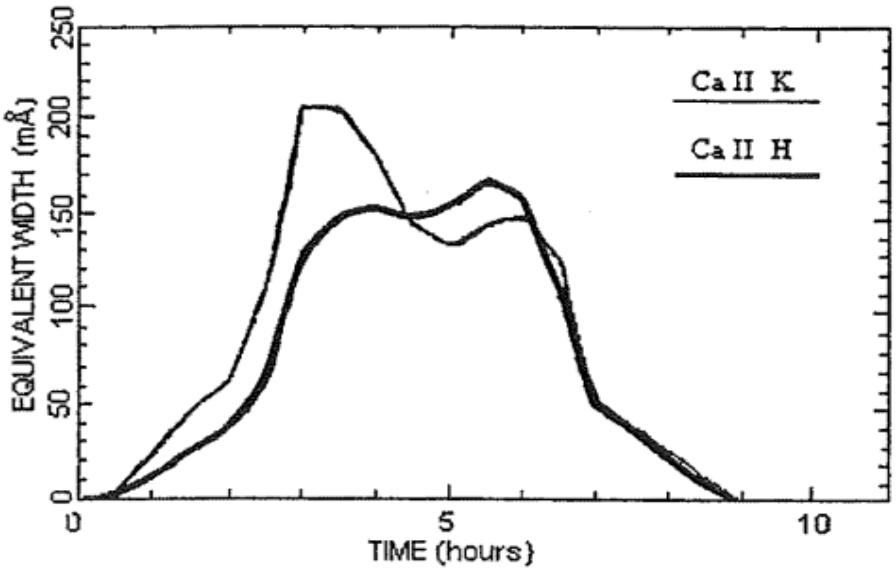

Figure 1.12: *The observed evolution of the E.W.s for the H & K lines as a FEB crosses the line of sight. Note that for a small duration (between 5 and 7 hours), the E.W. of the Ca II H line exceeds that for the K line. Source: Beust and Lissauer(1994) [14]*

Similar behaviour is observed when the evolution of the equivalent widths (E.W.s) of the H and K lines is studied as the FEB crosses the stellar surface. Figure 1.12 shows the evolution of the equivalent widths for the H & K lines as a FEB crosses our line of sight. As is visible on the figure, the equivalent widths of the H line exceeds that of K line for a small duration between 5 and 7 hours of the crossing event.

1.3 Planets in the Circumstellar disk and relation to the Falling Evaporating Bodies scenario

Until the recent discovery [55] of the gas giant planet β Pic b around the star, several arguments had been made for the existence of planetary bodies within the inner region of the β Pic disk by numerous authors. Independent arguments were made by Artymowicz et al. in 1988 and 1989 [56, 57] based on the observed thickness of the disk which suggested the presence of planetary bodies in the inner disk ($\approx$ few A.U.). It was proposed by Beust et al. (1990) [1] that such bodies could explain the simulation results that the inclination of the orbiting comets are constrained to an inclination of q = -

150 ° and are predominantly red-shifted. They argued that such a body would perturb the orbits of the comet-like bodies and some of these bodies may obtain orbits with very close periastria and therefore become our observed infalling bodies. As only an important perturbation (such as a planetary one) can explain the observed orbits of the comets, their argument seemed very appealing.

Later studies conducted by Lecavelier des Etangs et al.(1995) presented intriguing light variations from the disk which they argued was due to disk inhomogeneities produced by a Jupiter-sized planet at > 6 A.U. [58].

As mentioned briefly in Section1.1.2, several assymetries as well as a warp has been detected in the disk in both the optical and infrared wavelengths and Burrows et al.(1995) suggested that an unseen planet could explain the warp in the disk at the supposed region due to the argument that if the warp had been present when the star had formed, it would have been since flattened out unless it is produced and maintained by the gravitational pull of a planet. The authors went on to propose that the planet would lie within the inner clear region of the disk but as the overwhelming brightness of the star rules out direct imaging, the planet is highly unlikely to be detected via direct imaging [10].

Other studies (Mouillet et al.(1997) [45],Gorkavyi et al.(2004) [59],Augereau et al.(2001) [60] and Thebault & Beust (2001) [61]) concluded that the structure of the disk within the inner region is well reproduced by the deformation induced on colliding planetesimals by a giant planet on a slightly inclined orbit within 50 A.U. from the star.

As discussed previously, Beust et al. (1990) [1] postulated that the constraints on the inclination of the orbiting cometary bodies combined with their predominant 'infalling' nature could be explained due to a planetary perturbing body in the inner disk. Investigation into the dynamical mechanisms responsible for the origin of these star-grazing comets led to proposals of a model by Beust et al.(1996) [62] which suggested that the star grazing comets were trapped in a 4:1 and 3:1 mean motion resonance with a Jovian planet on a moderately eccentric orbit ($e \geq 0.05$). This is similar to the trapping of main belt asteroids in the asteroid belt in our solar system in a range of orbital resonances (mostly 3:1) with Jupiter, which results in a gap or dip in the semi major axes of these asteroids termed 'Kirkwood gaps' [63].

In a follow-up study published in 2000, Beust et al.(2000) produced dynamical simulations to test their model, which showed that the gravitational perturbation of at least one giant planet at $\approx$ 10 A.U. and with a moderate eccentricity of $\approx$ 0.05 can account for the observed rate of evaporating bodies and the warp in the disk [64]

Okamoto et al. (2004) performed high-resolution spectroscopic observations in the 10 μm band to identify concentrations of submicron-sized silicate dust at 6.4 A.U., 16 A.U. and 30 A.U. from the star which were interpreted as dust replenishing planetesimal belts at those locations [65]. By carrying out simulations using a range of orbital and planetary parameters of a supposed planetary perturber based on values given by previous authors (Morbidelli et al.(1997) ; Heap et al.(2000)), Freistetter et al. (2007)) concluded that a planet at 12 A.U. with a mass of 2 to 5 M_{Jup} and an eccentricity of ≤ 0.1 can probably already account for three major features observed in the β Pictoris disk (the main warp, two of the inner planetesimal belts and the FEBs). They also suggested that the existence of two additional planets at about 25 A.U. and 45 A.U., with upper limits of 0.6 M_{Jup} and 0.2 M_{Jup} on their masses, seems likely [66].

Discovery of β Pictoris b and its implications

The gas giant planet designated as β Pictoris b was discovered on 18 November 2008 by Lagrange et al. (2008) using the direct imaging method while using data from observations taken in 2003 using the European Southern Observatory's (ESO) Very Large Telescope's (VLT) Adaptive Optics NAOS CONICA (NaCo) instrument located in Cerro Paranal in northern Chile [15]. The observations were taken to benefit from both the high image quality provided by the Nasmyth Adaptive Optics System (NAOS, [67]) at infrared wavelengths and the good dynamics offered by the Near-Infrared Imager and Spectrograph (CONICA; [68]) detector in order to study the immediate circumstellar environment of β Pic. Initial near infrared images of β Pic obtained in 2003 showed a faint (apparent magnitude $L' = 11.2$) pointlike source at $\approx$ 8 A.U. in projected separation from the star, within the northeast side of the dust disk. However, the data were not sufficient to determine whether this faint source was a gravitationally-bound companion or an unrelated background star, whose projected position in the plane of the sky happened to be close to β Pictoris.

A re-reduction of the data conducted in November 2008 revealed the point-like source

to be most likely a gas giant planet with a typical temperature of ≈ 1500 K and mass of 8 M_{Jup} based on its apparent magnitude, while the notion that the source is actually a foreground or a background star lying in the plane of sky was ruled to be extremely unlikely based on the analysis of previous deep Hubble Space Telescope(HST) images [15].

Follow-up observations of the β Pic disk performed using the same instrument in late 2009 and early 2010 confirmed the existence of the planet but on the opposite side (south west) of the star located at a distance of 8 to 15 A.U. from the star [55]. These findings were published in the journal *Science* and represented the closest orbiting planet to its star ever imaged at the time.

Later observations performed in late 2010 and early 2011 allowed scientists to establish an inclination angle of the planet's orbit of 88.5 degrees, nearly edge-on. The location of the planet was found to be approximately 3.5 to 4 degrees tilted from the main disk in this system, indicating that the planet is aligned with the warped inner disk in the β Pictoris system [69]. Also, a much more recent study conducted using the Gemini Planet imager at near infrared wavelengths has provided an estimate on its mass of $12.9^{+0.2}_{-0.2} M_J$, making it a super Jupiter [70].

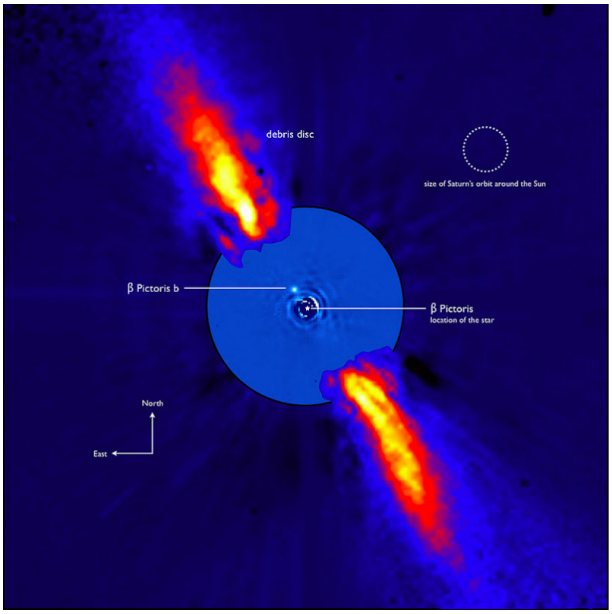

Figure 1.13: *Figure showing the supposed initial location of β Pic b in 2003 relative to β pic and the circumstellar disk (Source: Lagrange et al.(2008) [15]*

Since the discovery of β Pic b, there has been a lot of discussion among astronomers whether this planet is the supposed gas giant planet that has been hypothesised to exist in the inner region of the β Pic circumstellar disk. Within the framework of the FEB and the mean motion resonance model proposed by Beust et al. (1990) [1] and Beust & Morbidelli (1996, 2000) [62, 64], a gas giant planet orbiting between $\approx$ 5 -20 A.U. from the star with a moderate eccentricity of ≥ 0.05 and with a suitable longitude of periastron ($\approx -70^{\circ}{}^{+20}_{-20}$) is required to explain the constraints on the orbital parameters of the infalling evaporating bodies. The model also requires that there is probably no other giant planet orbiting the star within the specified distance and that there is the presence of a planetesimal belt at the locations of the main resonances. β Pic b fulfills the required criteria of size/mass, is highly likely to be responsible for the observed warp in the disk [71] and lies within the range of allowed distances of the expected planet, but its orbital eccentricity and the longitude of periastron are still too badly constrained while the presence or the lack of any inner planets is still unconfirmed [72]. Hence, β Pictoris b is a strong candidate for being the suspected giant planet responsible for causing the observed gravitational perturbations of the FEBs, although more investigations need to be conducted in regards to its orbital eccentricity and longitude of periastron and also

in regards to the presence of any other planets within the system.

1.4 Previous observational studies

Several observational studies have been conducted on the FEB scenario by previous authors such as Lagrange-Henri et al. (1996) [2], Petterson et al.(1999) [3], Persson et al.(1997) [4], Barnes et al. (2000) [7] and more recently, Kiefer et al.(2014) [6]. The study conducted by Lagrange Henri et al. (1996) was done using observations of β Pic taken in a range of wavelengths in December 1992 using a variety of ground sites in Chile, Australia and New Zealand and the International Ultraviolet Explorer(IUE) and the Hubble Space Telescope (HST) in space. The more recent study conducted by Kiefer et al. (2014) was done using spectra taken from 2003 to 2011 using the High Accuracy Radial velocity Planet searcher (HARPS) spectrograph which is attached to the 3.6 m European Southern Observatory (ESO) telescope in La Silla, Chile while the other mentioned studies (Petterson et al.(1999), Persson et al.(1997) and Barnes et al.(2000)) were conducted using observations taken at the UC Mt. John University Observatory and hence, these other studies would serve as good comparisons with the study conducted for this thesis which also relies on data taken at the UC Mt. John Observatory. Of these various studies, Lagrange-Henri et al.(1992), Petterson et al.(1999), Persson et al.(1998) and Barnes et al.(2000) observe the variability of the different absorption features across the course of a night and also between different nights, while the the study by Kiefer et al.(2014) focused on observing the variability of the different absorptions between different nights over a long time period (from 2003 to 2011) by using the median spectrum for a night. This was done by Kiefer et al.(2014) to study the independent absorptions due to different exocomets as opposed to a single exocomet which has a duration of transit of a few hours.

Results from these various studies can be summarised as follows:

- Small variability timescales for HVFs (on the order of hours) as compared to the LVFs(which have a variability timescale from hours to days) which implied that the comets responsible for the HVFs pass at higher orbital velocities compared to the LVFs .

- Predominance of higher FWHM for the features with higher relative velocities as compared to features with lower relative velocities. This resulted in an approximate positive correlation between the FWHM and the redshift velocity.

- While at any velocity, a range of depths are possible, the deepest features are always at a low redshift velocity (close to the circumstellar feature) while the highest velocity features are always shallow.

- Comparison of the H & K line profiles yielded higher values for α for LVFs as compared to HVFs, which showed that the higher velocity absorbing clouds generally occult less of the stellar disk as compared to the LVFs.

- By plotting the depths of the absorption features in the H & K lines against each other, it was found that almost all features fall within the optically thick ($p_K = p_H$) and optically thin($p_K = 2 \times p_H$) regimes with some authors (Lagrange-Henri et al. (1996) [2], Petterson et al. (1999) [3]) finding that some HVFs fall to the right of the optically thick limit implying that p_K was lower than p_H in some cases. This was interpreted by Lagrange -Henri et al. (1996) as being a differential effect of the high stellar rotation, which was pointed out in an earlier paper by Beust & Lissauer (1994) [14]. In defining the HVFs and LVFs for the plot in which the H & K line depths are plotted against each other, Persson et al.(1998) [4] and Petterson et al.(1996) [5] in their MSc. thesis, defined a cut-off value of 60 kms^{-1} for the HVFs and LVFs. This is in contrast to the published studies of Lagrange- Henri et al.(1996) [2] and Petterson et al.(1999) [3] where they used a cut off value of 40 kms^{-1} for dividing the LVFs and HVFs. Hence, plots produced by Petterson et al(1996) and Persson et al.(1997) in their unpublished MSc. thesis are also presented as shown in Figure 1.15. As shown by Figure 1.15 (b), Persson et al.(1998) also found some features which lied beyond the optically thin limit.

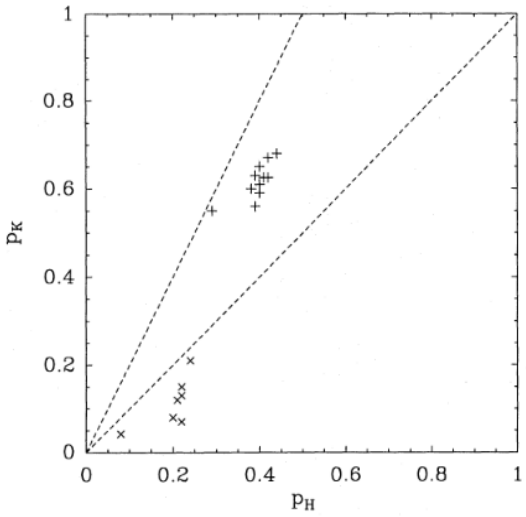

(a) Plot for the Ca II K line peak depths against the H line depths as obtained by Lagrange-Henri et al.(1996). Note the points which lie beyond the optically thick limit. Source: Lagrange-Henri et al. [2]

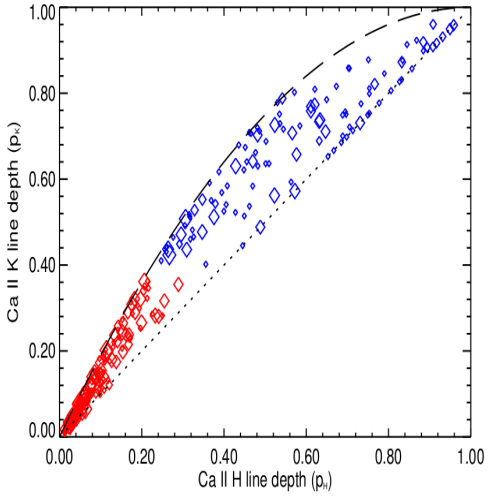

(b) Plot for the Ca II K line depths against the Ca II H line depths for the 252 independent absorption features with $\alpha < 1$. Points plotted in red show the 147 exocomets identified as members of population S($p_K < 0.4$) and those plotted in blue show 105 exocomets of population D($p_K > 0.4$). The dotted line represents the optically thick limit($p_K = p_H$) while the dashed line represents the $\alpha = 1$ limit. Source: Kiefer et al.(2014) [6]

Figure 1.14: Plots of the Ca II K line peak depths as a function of Ca II H line peak depths by Lagrange-Henri et al. (1996) [2]and Kiefer et al. (2014) [6]

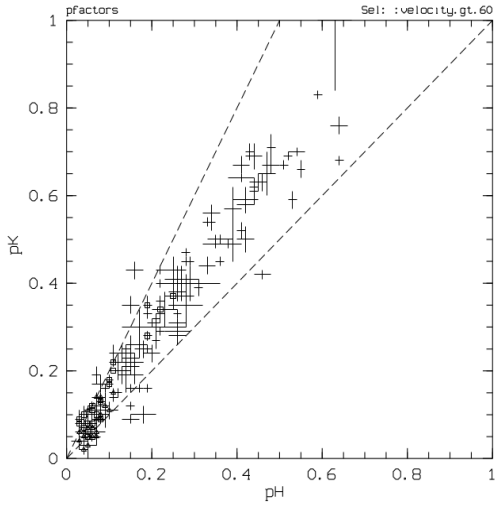

(a) Plot obtained by Petterson et al.(1996) for peak depths in the H & K lines. Squares represent blueshifted features, crosses represent LVFs and triangles represent HVFs. Source: Petterson et al.(1996) [5]

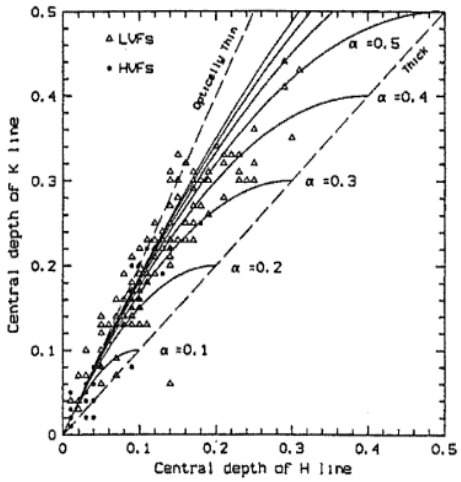

(b) Peak depths in the H & K lines plotted against each other for HVFs and LVFs. Note the high number of features which fall beyond the optically thin limit (predominantly HVFs). Source: Persson et al.(1998) [4]

Figure 1.15: Plots obtained by Petterson et al.(1996) and Persson et al.(1998) for the peak depths in the Ca II H & K lines using a cut off value of 60 kms^{-1} for the HVFs and the LVFs as shown in their unpublished MSc. thesis.

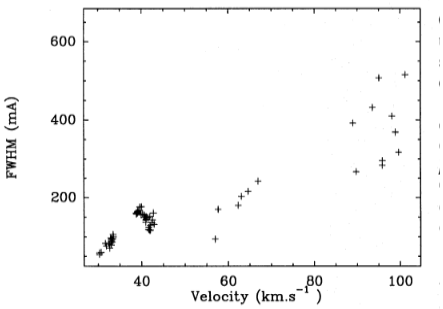

(a) FWHM plotted against redshift velocity(Source: Lagrange-Henri et al.(1996) [2])

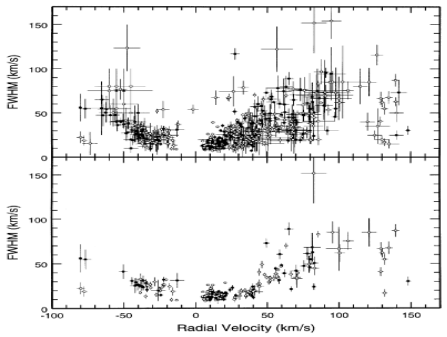

(b) FWHM plotted against velocity for both H line(filled symbol) and K line(open symbol). Bottom panel shows only those absorptions classified as 'gS'. Source: Petterson et al.(1999) [3]

Figure 1.16: Obtained plots for FWHM against velocity by Lagrange-Henri et al.(1996) [2] and Petterson et al.(1999) [3]

It was also found by the authors who also fit the absorptions in the H & K lines independently (Petterson et al.(1999),Persson et al.(1998) [3, 4]) that the radial velocity at peak depth for various absorptions generally agreed with each other strongly in both the H & K lines. Figure 1.16 shows the values obtained by various authors for the radial velocity at peak depth of the different absorptions in both the H & K lines which shows this strong agreement between the two lines. This strong agreement of the radial velocities in the H& K lines was hence assumed by various authors such as Barnes et al.(2000) and Kiefer et al.(2014) [6, 7] who only fitted the absorptions in the H & K lines simultaneously yielding a simultaneous measurement of radial velocity at peak depth for each absorption for both the H & K lines. For the purposes of this thesis as well, the radial velocities of the different absorptions in the H & K lines were assumed to be equal to each other which resulted in a single measurement of radial velocity for each absorption for both the H & K lines.

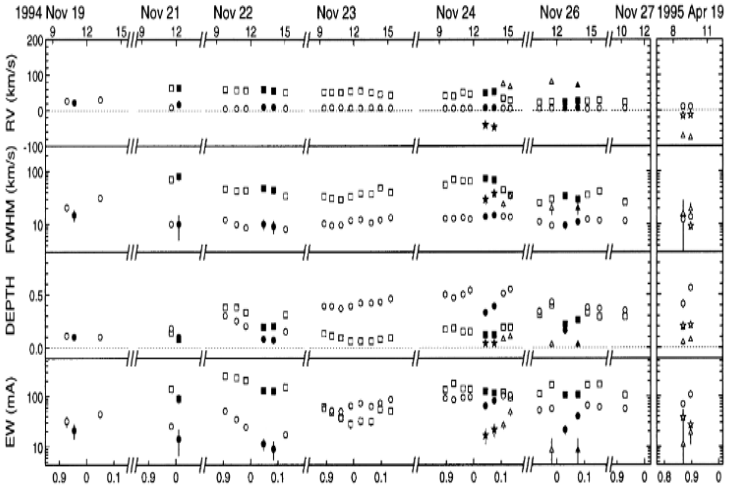

(a) Figure showing the variation in the different fitted parameters across different nights. Note the strong agreement in radial velocities in both the H & K lines as shown in the top panel.Source:Petterson et al.(1999) [3]

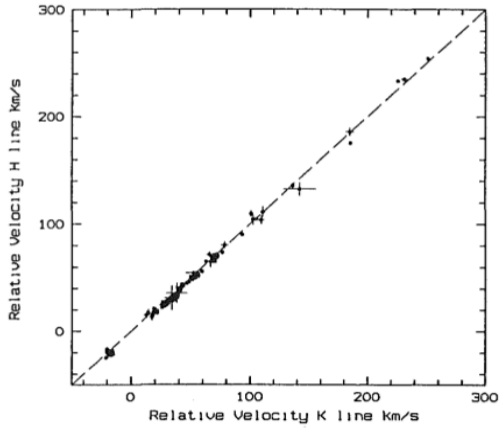

(b) The radial velocity at central depth in the H & K lines plotted against each other.Source: Persson et al.(1998) [4]

Figure 1.17: Figures showing the strong agreement of radial velocity for the different absorptions in both the H & K lines.

The paper by Kiefer et al. (2014) [6] strengthened the argument that the exocomets around β Pic are divided into two distinct families with members of each family being largely responsible for the HVFs and LVFs in the Ca II absorption profiles. By

analysing 1,106 spectra of β Pic gathered between 2003 and 2011, they detected about 6000 variable absorption signatures arising as a result of exocomet transits and 252 exocomets were detected with α <1. They termed these distinct populations of the comets as populations S and D and noted that comets for population S corresponded to small surface ratio ($\alpha \approx 0.1$), produce shallow absorption lines ($p_K < 0.4$) and the second population corresponded to a large surface ratio ($\alpha \approx 0.8$) and produce deep absorption lines ($p_K > 0.4$). They also found that the two populations have different FWHM and radial velocity distributions with population D showing a broader distribution of both radial velocities and FWHM as compared to the population S. Figure 1.18 shows plots of a histogram for each of the obtained parameters which shows the dichotomy of the histograms corresponding to the two distinct exocomet families. Figure 1.19 shows the coma absorption depths plotted as a function of surface ratio of transiting exocomets and confirms the two family hypothesis for the exocomets as shown by the two distinct clusters plotted in blue and red.

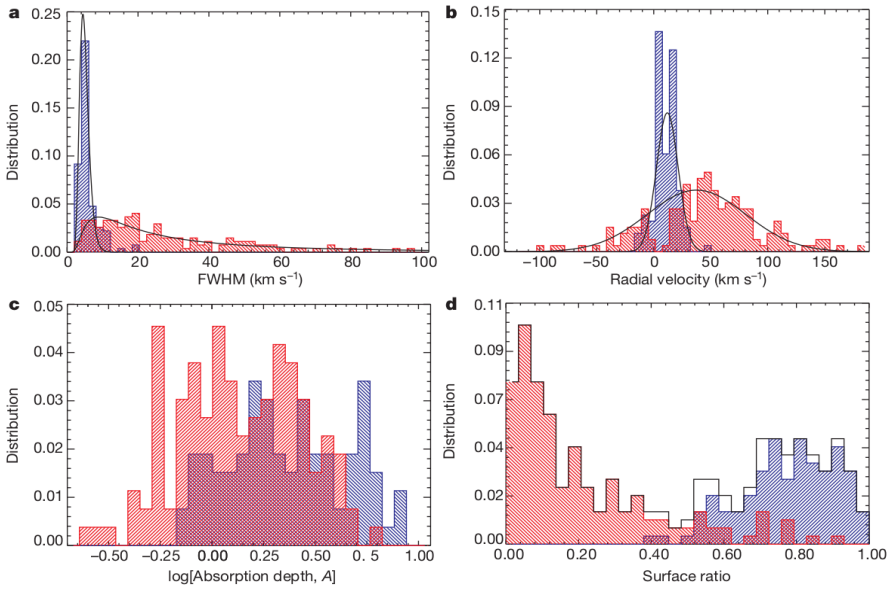

Figure 1.18: ***Figure showing the distribution of the obtained values for the different parameters for the identified independent absorptions corresponding to the 252 exocomets with*** $\alpha < 1$***.*** *Distribution for the parameters for the 105 exocomets corresponding to Population D are shown in blue while the distribution for the 147 exocomets corresponding to population S is shown in Red. Note the dichotomy of the different distributions which further supported the existence of two different families of exocomets around β Pic. Source:Kiefer et al.(2014) [6]*

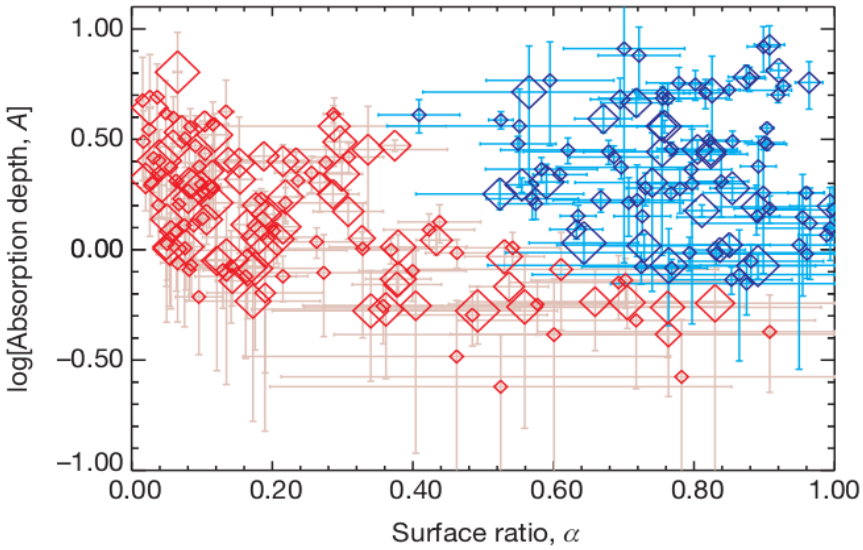

Figure 1.19: ***Coma absorption depths plotted as a function of surface ratio for transiting exocomets.*** *The log of the absorption depths, A, of the 252 detected exocomets with $\alpha < 1$ are plotted against the values of the surface ratio, α. Small symbols correspond to data taken in 2003 and large symbols correspond to 2011 data. Error bars represent the standard deviation. The 147 exocomets of the so called Population S, producing shallow absorption lines ($p_K < 0.4$), are plotted in red, while the 105 exocomets producing deep absorption lines ($p_K > 0.4$), the so called population D, are plotted in blue. The cloud sizes show a bimodal distribution with a deficiency of exocomets with high absorption depths at intermediate sizes. Source: Kiefer et al.(2014) [6]*

1.5 Motivation of thesis

Recently, attempts were made by Wang et al.(2016) [73] to constrain the orbit of β Pic b by performing milliarcsecond astrometry using the Gemini Planet searcher. The most probable orbital parameters (with a posterior probability of 50%) yielded an orbital period of 22.47 years and allowed them to predict that the Hill sphere of β Pic b will transit β Pic from the start of April 2017 till January 2018 for a duration lasting approximately 300 days and with an impact parameter of 20% of the Hill sphere radius. The Hill sphere of an astronomical body is defined as the region around the body within which it dominates the attraction of satellites. For example, for a moon to be retained by a planet, the moon must have an orbit which lies within the Hill sphere of the planet. The moon in turn, has its own Hill sphere and an object which lies within a moon's

Hill sphere is likely to become a satellite of the moon itself rather than the planet. This prediction of a β Pic b Hill sphere transit of β Pic in 2017 prompted our 2017 observational campaign. This thesis is an analysis of the β Pic absorptions in 2017, to examine the variability of the features within the FEB scenario across 2017, and to look for any evidence of the effects of a planetary Hill sphere transit of β Pic. The thesis is also primarily aimed at confirming the relationship between the different parameters of the Gaussian fits to the absorptions (radial velocity at peak depth, peak depth, FWHM and E.W.) as obtained and discussed by previous authors (Lagrange-Henri et al.(1996) [2], Petterson et al.(1999) [3] and Persson et al.(1998) [4]) and understanding the cause of these relationships within the context of the FEB model. Another aim of this thesis is verifying the hypothesis as derived by Kiefer et al.(2014) [6] that the exocomets around β Pic can be divided into two distinct families, by plotting the log of the absorption depths for the different absorptions against their values of the filling factor, α.

CHAPTER 2

Observations

2.1 University of Canterbury Mount John Observatory

All of the data used in this analysis were collected using the Mount John Observatory (UC MJO), situated close to the township of Tekapo in the South Island of New Zealand. It is located at an elevation of 1029 m at geographical coordinates 170°27.9′E 43°59.2′S. The spectroscopic data for this thesis have been collected using the HERCULES spectrograph attached to the 1 m McLellan telescope via an optical fibre [74]. The High Efficiency and Resolution Canterbury University High Resolution Spectrograph(**HERCULES**) is a fibre-fed echelle spectrograph in operation at UC MJO since April 2001 and has a total efficiency dependent on seeing and wavelength [75]. The maximum efficiency at seeing of 1" is just over 20% at a blaze wavelength near $\lambda = 650$ nm while at median seeing conditions (around 2.5"), the spectrograph efficiency is estimated to be approximately 12% [75]. The spectrograph has a resolving power dependent on the connected optical fibre with a maximum resolving power of 82000 when connected to the 50 μm fibre. However, for the purposes of this thesis, the 100 μm fibre was used which has a resolving power of 42000 [74]. The CCD detector system used to record the spectrum incorporates the Fairchild 486 back-illuminated CCD which comprises 4096x4096 15μm pixels which allow echelle spectra over a wavelength range from 380 nm to 880 nm to be recorded in a single exposure [74]. The system was made by Spectral Instruments Inc of Tucson, Arizona, United States and was received in Christchurch in December 2005, and mounted on the spectrograph from early 2007 onwards.

2.2 Observing log

The spectroscopic data for HD 39060 (totalling 1025 spectra) used for this thesis were collected in 2017 from the 12^{th} of January 2017 to the 9^{th} of December 2017. The observations were performed by Mr. Fraser Gunn on the different nights using the previously mentioned optical fibre and the CCD. Table 2.1 lists the different observations that were taken of β Pic within the timeframe.

Table 2.1: Table showing the spectra of β Pic taken over 2017 with the corresponding exposure times

Observing log for β Pic for 2017				
Date	Julian Date	# of spectra	Exposure time	Used for Analysis?
12^{th} January 2017	J7766	14	180 s	✓
14^{th} January 2017	J7768	4	180 s	✓
15^{th} January 2017	J7769	2	180 s	✓
16^{th} January 2017	J7770	6	180 s	✓
7^{th} February 2017	J7792	6	300 s	X
9^{th} February 2017	J7794	5	300 s	X
10^{th} February 2017	J7795	5	300s	X
8^{th} March 2017	J7821	10	300 s	X
9^{th} March 2017	J7822	15	300s	X
14^{th} March 2017	J7827	15	300 s	X
6^{th} April 2017	J7850	5	300 s	✓
7^{th} April 2017	J7851	5	300 s	✓
8^{th} April 2017	J7852	5	300 s	✓
9^{th} April 2017	J7853	5	300 s	✓
10^{th} April 2017	J7854	5	300 s	✓
8^{th} May 2017	J7882	5	300 s	✓
9^{th} May 2017	J7883	5	300 s	✓

Continued on next page

Table 2.1 – continued from previous page

11^{th} May 2017	J7885	5	300 s	✓
12^{th} May 2017	J7886	5	300 s	✓
13^{th} May 2017	J7887	5	300 s	✓
14^{th} May 2017	J7888	3	300 s	✓
15^{th} May 2017	J7889	5	300 s	✓
18^{th} May 2017	J7892	5	300 s	✓
5^{th} June 2017	J7910	10	300 s	✓
6^{th} June 2017	J7911	5	300 s	✓
7^{th} June 2017	J7912	5	300 s	✓
8^{th} June 2017	J7913	5	300 s	✓
9^{th} June 2017	J7914	5	300 s	✓
10^{th} June 2017	J7915	7	300 s	✓
11^{th} June 2017	J7916	5	300 s	✓
13^{th} June 2017	J7918	3	300 s	✓
14^{th} June 2017	J7919	5	300 s	✓
15^{th} June 2017	J7920	5	300 s	✓
3^{rd} July 2017	J7938	5	300 s	✓
4^{th} July 2017	J7939	5	300 s	✓
5^{th} July 2017	J7940	5	300 s	✓
6^{th} July 2017	J7941	5	300 s	✓
7^{th} July 2017	J7942	5	300 s	✓
8^{th} July 2017	J7943	5	300 s	✓
9^{th} July 2017	J7944	5	300 s	✓
13^{th} July 2017	J7948	8	300 s	✓
14^{th} July 2017	J7949	9	300 s	✓
25^{th} July 2017	J7960	10	300 s	✓
27^{th} July 2017	J7962	20	300 s	✓

Continued on next page

Table 2.1 – continued from previous page

28^{th} July 2017	J7963	10	300 s	✓
30^{th} July 2017	J7965	10	300 s	✓
31^{st} July 2017	J7966	10	300 s	✓
2^{nd} August 2017	J7968	5	300 s	X
4^{th} August 2017	J7970	5	300 s	X
5^{th} August 2017	J7971	10	300 s	X
29^{th} September 2017	J8026	30	600 s	✓
30^{th} September 2017	J8027	36	600 s	✓
1^{st} October 2017	J8028	14	600 s	X
2^{nd} October 2017	J8029	34	600 s	X
3^{rd} October 2017	J8030	20	600 s	X
4^{th} October 2017	J8031	23	600 s	X
5^{th} October 2017	J8032	29	600 s	X
7^{th} October 2017	J8034	2	600 s	X
8^{th} October 2017	J8035	8	600 s	X
10^{th} October 2017	J8037	8	600 s	X
30^{th} October 2017	J8057	31	600 s	X
31^{st} October 2017	J8058	45	300 s	X
1^{st} November 2017	J8059	60	300 s	X
4^{th} November 2017	J8062	63	300 s	X
5^{th} November 2017	J8063	48	300 s	X
4^{th} December 2017	J8092	56	300 s	✓
5^{th} December 2017	J8093	60	300 s	✓
6^{th} December 2017	J8094	58	300 s	✓
7^{th} December 2017	J8095	60	300 s	✓
9^{th} December 2017	J8097	18	300 s	✓

2.3 Observational Methodology

During each night of observation, three different types of spectra are recorded. At the start or end of each night of observation, flat-field spectra are taken which are obtained by passing white light from an incandescent tungsten lamp via the spectrograph and obtaining an image on the CCD. Thorium -argon arc calibration spectra were taken at the start of each observing night and preceding and following every stellar observation. These two types of spectra are used for the calibration of the stellar images.

Flat-field spectra are taken to account for pixel to pixel sensitivity variation on the CCD and also to compensate for different dark currents on the CCD. Dark current refers to a relatively small electrical current flowing between pixels on a CCD even in the lack of any illumination due to thermal excitation and this artifact is removed by applying a flat field correction [76] as part of the data reduction process. Flat field spectra are relatively featureless, i.e they have no emission or absorption lines, and are used primarily for spectral order tracing on the CCD and to correct for the CCD intensity response variation (in the flat field processing step of the data reduction process). Flat field images are also used to account for the effect of dust or scratches on the CCD window, and for vignetting by the telescope or camera lens optics [76]. For the observations for this thesis, ten 2-second exposures were taken of the incandescent tungsten lamp to obtain the flat field spectra at the start or end of the observational night.

Thorium-argon spectra were obtained by passing the light of a thorium-argon emission lamp through the spectrograph and recording it on the CCD. Each thorium-argon spectrum contains several thousand emission lines with well-known wavelengths which, in conjunction with the flat-field spectra, can be used to determine the wavelengths of the spectral orders of each stellar observation. To obtain the thorium argon spectra, six 5 second exposures were taken at the start of a night while one 5-second exposure was taken preceding and following every stellar observation.

Stellar spectra (e.g. Figure 2.1) were obtained by passing the light of the target star through the optical path of the telescope and the spectrograph and recording it on the CCD. The exposure time for the target star(HD-39060) varied depending on current

seeing conditions but was usually 300 s with some exposures lasting 240, 180 or 600 s as shown in Table 2.1.

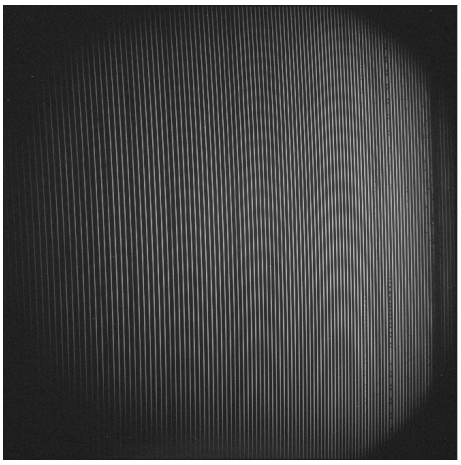

Figure 2.1: *A raw stellar image taken on 12th January 2017 for β pic. The bright white vertical lines represent the different spectral orders while the points at which the lines get dimmer represent the absorptions.*

CHAPTER 3

Data reduction and analysis procedure

3.1 Data reduction step

The raw stellar images have to be converted into a more useful format in order to be analysed. Spectroscopic data reduction is the removal of data artifacts, variables intrinsic to the observational equipment and standardisation of the observations including wavelength calibration.

As each pixel on the CCD can only store a certain amount of charge, overexposing the CCD can lead to an excess of charge buildup in a pixel, leading to charge leaking into the neighbouring pixels. This can result in a 'saturation trail' on the image [77].This is an artifact that is a major problem in Thorium-argon calibration images although not in stellar images. Other examples of image artifacts include dark marks on the images due to the presence of a foreign body entering the CCD housing and finding its way onto the detector or dark doughnut shaped artifacts on the image due to the presence of a dust grain on the filter or the window of the CCD camera causing a shadow on the detector [77].

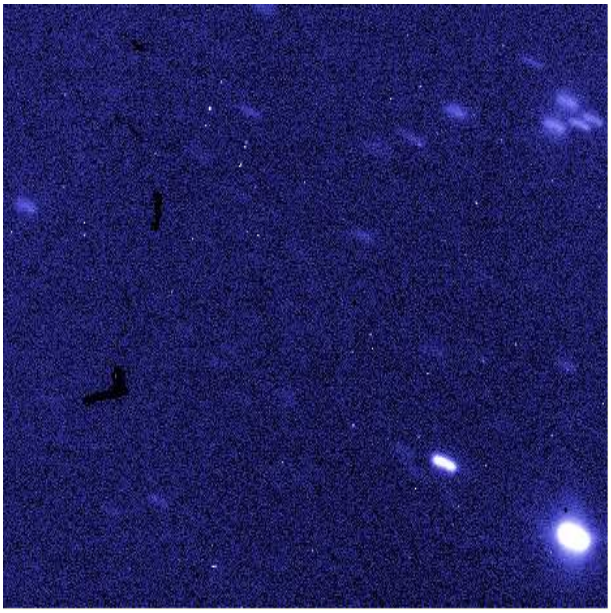

(a) Dark marks on the left side of the image due to the presence of a foreign body entering the CCD housing

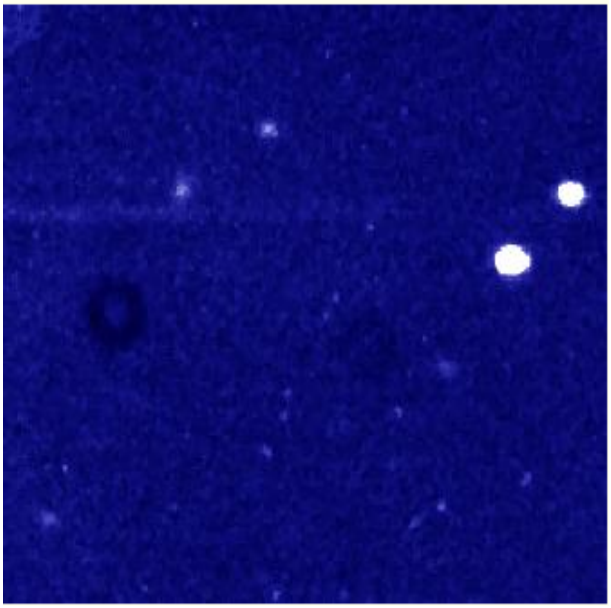

(b) Dark 'doughnut' shaped artifact due to the presence of a dust grain

Figure 3.1: Figures (a) and (b) show image artifacts due to the presence of a foreign body or a dust grain in the CCD housing

It is artifacts such as these which can be partially or completely removed in the data reduction step by applying a flat field correction.

Examples of variables intrinsic to the observational equipment include pixel-to-pixel sensitivity variations on the CCD and the presence of electrical charge on the CCD chip due to thermal excitation in the lack of any illumination (dark current).

The various steps of data reduction were performed through two separate MATLAB code pipelines. The first data reduction pipeline identifies the type of image (either flat-field, thorium-argon arc or stellar) from the headers of the FITS files saved in the archives. This pipeline applies the flat- field correction on the stellar images and in combination with the thorium-argon images, extracts the spectral orders of each observation in a counts vs wavelength format. This MATLAB code pipeline was originally written by Dr. Duncan Wright [78], with usability and efficiency enhancements by Dr. Emily Brunsden [79]. The raw data are archived as FITS images according to the date of the night on which they were recorded. All of the flat-field, thorium-argon arc and stellar images recorded within a specific configuration are processed as a single 'run' of typically one week duration. Hence, the data was reduced on a 'run by run' basis. The second data reduction pipeline was also written by Dr. Duncan Wright with efficiency and usability enhancements by Dr. Emily Brunsden and Mr. Aaron Greenwood [80] and this pipeline rescales all the stellar orders onto the same wavelength scale, performs barycentric correction, performs a continuum fit, removes cosmic rays and after applying the continuum fit and merging all the spectral orders together, produces a normalised spectrum for each stellar observation.

3.1.1 First Data reduction Pipeline

Hercules Matlab Reduction.m

The main script for the reduction is Hercules Matlab Reduction.m. This script allows the selection of the target star for the data reduction, along with the blue data chop value which specifies the number of rows of pixels to remove from a CCD image at the blue end of the spectrum, and other values such as the amount of smoothing on the flat field data and the smoothing on the stellar and flat field background data. The blue data chop value determines the upper bound on the number of pixels that will be extracted

in the order extraction step. The value chosen for this was 500 pixels which allowed the reduction process to extract all orders up to order 150 to include the wavelengths of the Ca II H & K absorption lines. This script also allows the user to control whether to plot the cosmic ray filtering process for the stellar and the flat field images. This script calls all of the relevant functions which perform the various steps of the data reduction process.

Flat field processing

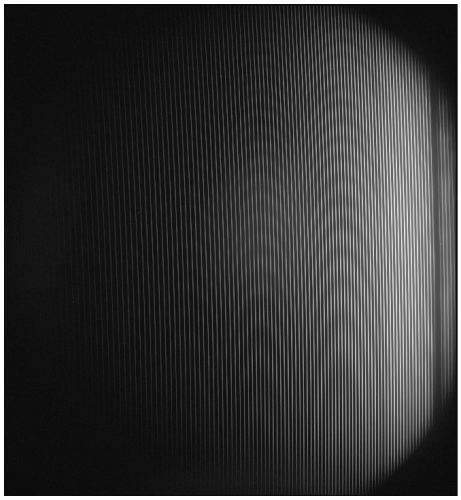

(a) An example of a flat field image taken on 12th January 2017.

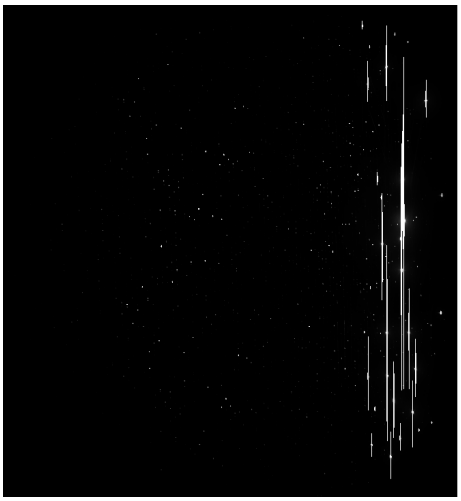

(b) An example of a Thorium image taken on 12th January 2017. The bright spots represent the emission lines while the bright 'streak' on the right represents a saturation trail.

Figure 3.2: Example of a Flat Field and a Thorium-argon arc image

As a first step in this process, the flat field images are manually examined to ensure that there were no overexposed or underexposed images. An automated statistical comparison was performed to ensure that there was no significant variation between the images. Then, the flat field spectra pertaining to each observation were averaged together to produce a master flat field image for a specific night. The blue data chop value specified earlier is used to remove the specific number of rows of pixels from the final flat field, stellar and arc images. The locations and the widths of the different spectral orders were determined from the flat field image for use in spectral order tracing for the thorium argon arc images and the stellar images. The output of this step is a fourth order relation

for each specific order as a function of pixel position along the x axis. Then, the master flat field image is background fitted i.e the background signal is extracted, modelled and subtracted from the master flat field image by performing a cubic spline interpolation in the inter order regions. Cosmic ray removal is also performed to account for the occasional cosmic ray infiltrating the CCD during the 2 second exposures. To account for the intensity response variation across the CCD, the intensity values for each pixel are recorded for use in the stellar processing stage. All of these steps were performed by the script Flat_processing.m.

Thorium Argon processing

After the flat field processing stage is complete, a statistical check was performed to ensure there was no significant pixel to pixel deviations in the thorium-argon arc images. Overexposed, underexposed or incorrectly saved images are removed at this stage. Then a calibration matrix containing the locations of several thousand emission lines is used to locate thorium argon arc emission lines with well known wavelengths as a function of pixel position. The most intense emission lines of the thorium-argon arc lamp were in the infrared region. As such a large portion of the thorium-argon arc image was unavoidably overexposed (see Figure 3.2b), it was not used for calibration. If the number of identified emission lines was below a threshold value of 900, then the user was queried to perform a manual calibration to identify the emission lines. If the number of emission lines identified was satisfactory, then the new calibration matrix was applied to the subsequent images. Once the emission lines for each image were located, a wavelength solution was obtained for each individual order via means of a fourth order wavelength dispersion relation as a function of pixel position. All of these steps were performed by calling the script *processing_all_ThArs.m* from the main script.

Stellar Processing

Once the wavelength solutions for each order of each thorium argon arc image were determined, the specified blue data chop value of 500 pixels was used to remove the blue section of the stellar images that correspond to a specific number of rows of the CCD. After this step, the background signal was modelled, extracted and subtracted for each stellar observation (as per the flat field processing step). Then the spectral orders

for each stellar observation were extracted by using the master flat field information corresponding to the specific observational night and cosmic ray removal was performed.

Now, the wavelength solutions obtained for the various orders for the thorium argon arc images taken before and after each stellar observation were linearly interpolated to obtain the wavelength solution for a specific stellar image. This was necessary as the wavelength solution for a specific image is dependent on the whole telescope/spectrograph/CCD system which can exhibit minute physical deformations due to variations in the temperature and pressure over the course of a specific observational night [81]. The final wavelength solution and the master flat field information was used to calculate the wavelengths across each spectral order. The recorded pixel values across the master flat field image was then used to normalise the intensities of each bin of each stellar spectrum in order to correct for the intensity response variation across the CCD.

At the end of the stellar processing stage, all of the reduced data corresponding to each stellar observation was stored as MATLAB readable .mat files to be processed by the second data reduction pipeline. The script responsible for performing all of these steps was *processing_all_stellar_images.m* which was called by the main script.

3.1.2 Second Data reduction pipeline

Identification of relevant orders for processing

After the spectral orders of each stellar observation were extracted in a normalised intensity vs wavelength format, the orders corresponding to the Ca II H and K absorption lines were identified. The wavelengths used for the Ca II H and K absorption lines were 3968.468 Å and 3933.663 Å respectively and this corresponds to orders 143 (H line), 144(H and K line) and 145(K line).

It was found that for each of these three relevant orders, different runs had different quality of spectra. Although the spectra corresponding to different observations within each run were very similar, spectra corresponding to some runs had very low signal-to-noise ratio, had faulty data or did not span the whole wavelength range of the order. Hence, specific runs were excluded for each specific order to allow better processing of the data. As the excluded runs varied from order to order, the processing of the reduced data was done on an order by order basis.

Order 143 was selected for analysis of the Ca II H line because of spectra in order 144 not spanning the whole wavelength range for the H line and order 144 was selected for analysis of the Ca II K line because of a higher average value of the quantity *weights* (which serves as an estimate of the noise level in a spectrum) as compared to order 145.

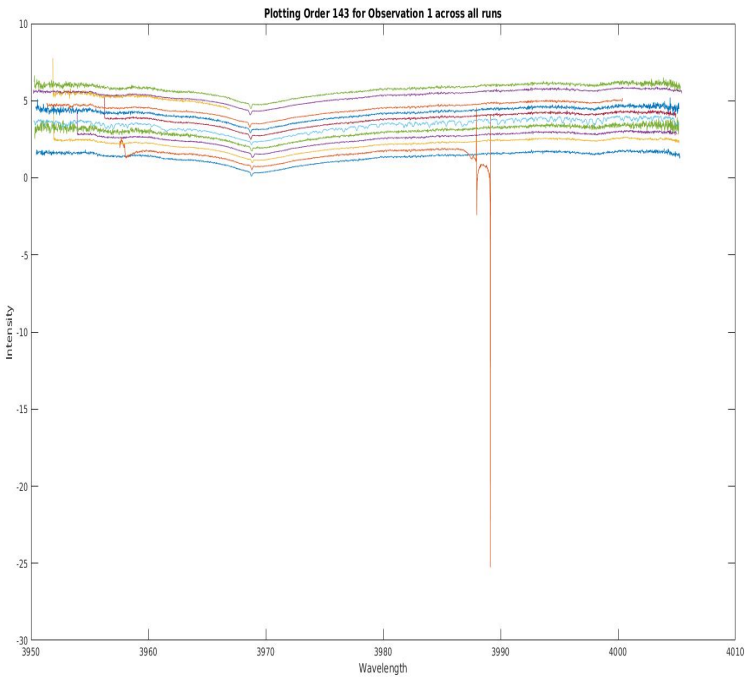

Figure 3.3: *Order 143 plotted across different runs. The runs increase from Run 1 to 12 from bottom to top. Note the faulty Run 10 (corresponding to the third spectrum from the top in yellow) which spans a very small wavelength range which led to its exclusion from the processing step for this order.*

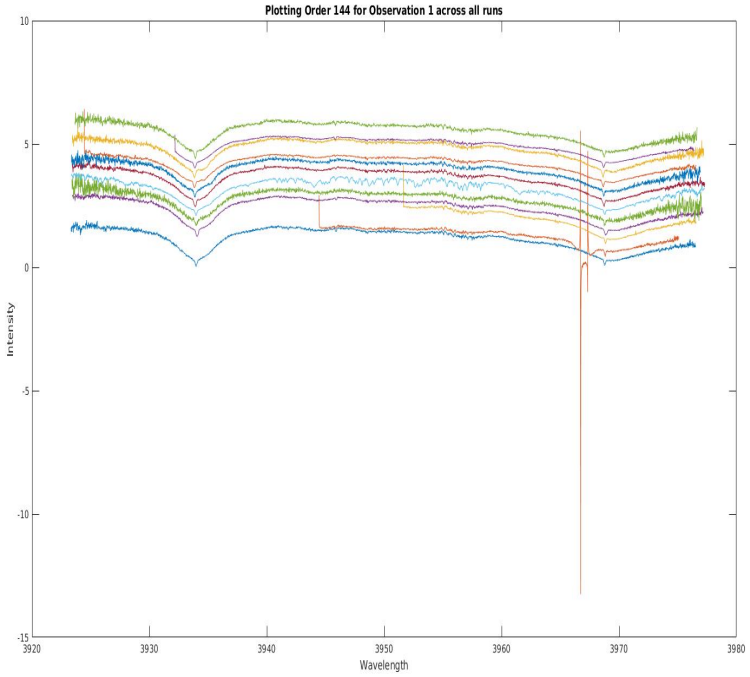

Figure 3.4: *Order 144 plotted across the different runs. The runs increase from Run 1 to 12 from bottom to top. Note the faulty Runs 2 ,3 (corresponding to the* 2^{nd} *and* 3^{rd} *faulty spectra from the bottom in magenta and yellow respectively) and 11(corresponding to the* 2^{nd} *spectrum from the top in purple) which span a small wavelength range which led to their exclusion from the processing step for this order.*

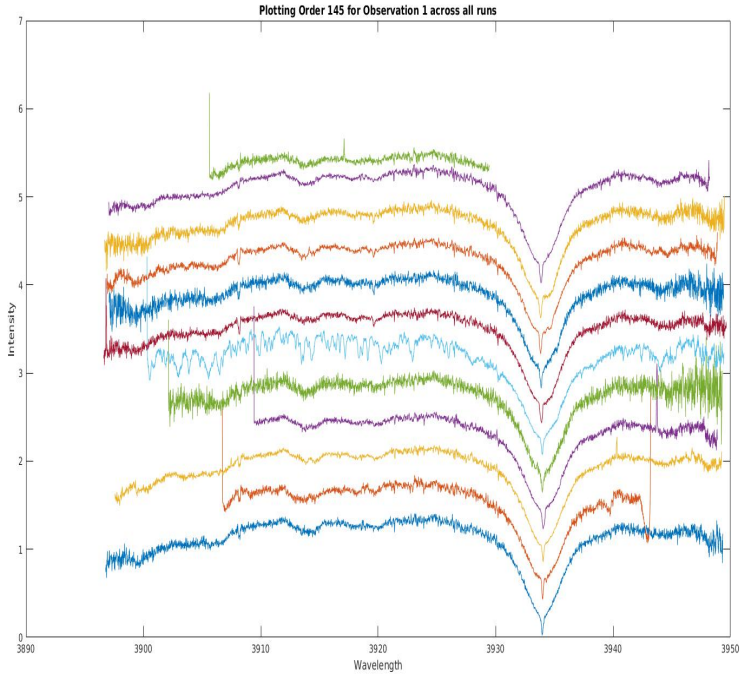

Figure 3.5: *Order 145 plotted across the different runs. The runs increase from Run 1 to 12 from bottom to top.Note the small wavelength range of Run 2 (2^{nd} spectrum in magenta from the bottom) and 12 (green spectrum at the very top) which led to their exclusion from the processing step for this order.*

Begin_processing.m

The Begin_processing.m script is responsible for calling the relevant MATLAB functions. This script allows selection of the range of spectral orders to be processed by specifying a **first** and **last** order. This script also allows the user to specify the stellar parameters corresponding to the chosen star for use in generation of synthetic spectra in the cross correlation step. Finally, the script allows the user to call the cfitting.m script which performs the continuum fit.

The original script also consisted of a call to the script *prepare_for_famiasv2.m* which is responsible for generation of a delta function template for the star, allowing cross correlation of the mean stellar spectrum with the template to produce a mean line profile for a star. However , this step is only useful for studying representative and

cross-correlated mean line profiles for a star and the *prepare_for_famiasvs2.m* was not used in this research.

3.1.3 Wavelength and velocity correction

The first step in the processing of the reduced data is wavelength resampling and velocity calibration. To perform wavelength resampling, the spectral orders are standardised by first loading the .mat files for each observation and examining the overlapping wavelength range for each order. To do this, the observation with the smallest wavelength range for a specific order is identified and the other orders corresponding to other observations are resampled to the same wavelength range by trimming away the wavelength bins of the other orders outside the wavelength range of the smallest order.

As the Mount John Observatory is located on Earth which is in orbit around the Sun, it does not exist in an inertial reference frame. As the motion of β Pictoris around the galactic centre is negligible , it is a reasonable approximation that β Pictoris is in an inertial reference frame. As photons emitted in an inertial reference frame should be ideally collected by a detector in an inertial reference frame, a correction needs to be applied to the photons recieved at UC MJO. A correction called the barycentric correction [82], places the observer at the barycenter of the Solar System and as the motion of the solar system around the galactic centre is also taken to be negligible, this is a reasonable conversion from the reference frame of the UC MJO to an inertial reference frame. After the barycentric correction was performed, the rescaled orders were saved.

Upon the creation of the data1.mat file, the script datawork2.m was used to remove order-to-order differences across the different observations and also to approximately normalise the intensities across each spectral order. The order-to-order differences were removed by dividing the intensities for each wavelength bin for each order for each observation by the median intensity for all observations. To approximately normalise the intensities, the orders were fitted with a variable order polynomial to simplify the continuum fitting process for the next step. Finally, systemic velocity correction was performed on the wavelength axis across each order. This correction allows the wavelength axis across the orders to be Doppler shifted to account for the radial velocity of the star.

Continuum fit and removal of remaining cosmic rays

In this step, the script cfitting.m is called from the main script which performs the different steps of the continuum fitting process. To perform a continuum fit, the continuum level of each order was identified by selecting a set of points at the continuum manually and then fitting these points by means of a piecewise cubic spline interpolation[1]. After a suitable continuum fit has been performed, the script datawork3.m is called from the main script which applies the continuum fit and removes any remaining cosmic rays. The continuum fit is applied by dividing the intensities across each order with the resulting polynomial to produce a resultant normalised spectrum. As a final step, the different orders are usually merged together to create a final normalised spectrum for the star. As the processing for this thesis was done on an order-by-order basis, merging of the different orders was not applicable in this case.

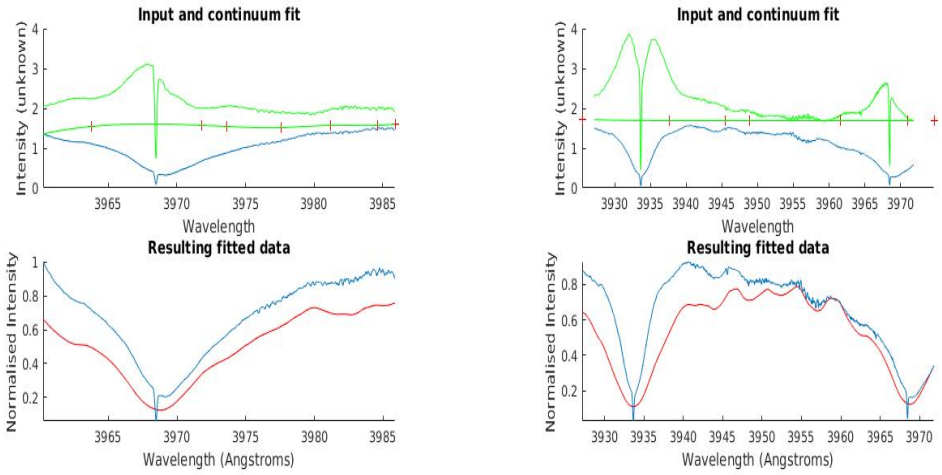

(a) Continuum fit for order 143

(b) Continuum fit for order 144

Figure 3.6: Figures showing the continuum fits for orders 143 and 144. The top subfigure shows the performed continuum fit (green) while the bottom subfigures show the obtained normalised spectra (in blue) and the synthetic spectra (in red)

[1]Piecewise cublic spline interpolation is an interpolation technique in which a cubic polynomial approximation is assumed across each subinterval (in this case between each two points)

3.2 Analysis procedure

3.2.1 Conversion from wavelength space to velocity space

Once the spectra had been normalised, the next step was the conversion of the wavelength axis of the spectra to a velocity axis. This was done by applying the equation for the Doppler effect which allows calculation of the radial velocity of a moving object emitting light of a wavelength λ to be worked out as follows:

$$R.V. = \frac{(\lambda - \lambda_r)}{\lambda} * c \tag{3.1}$$

where λ_r is defined as wavelength of light emitted by the object in its rest frame and c is defined as the speed of light. The value used for c was 299792.458 kms^{-1} while the rest wavelengths used for the K line and H line were 3933.663 Å and 3968.468 Å which are close to the values of 3933.664 Å and 3968.470 Å by C.Moore et al.(1972) [83]. As the wavelength of light received by an observer from a source moving away from the observer are increased in magnitude(red-shifted), the radial velocity of the source is positive, while in the case the source is moving towards the observer, the wavelengths are blue-shifted(decrease in magnitude) which results in negative (blue-shifted) velocities. This conversion of the wavelength axis to a radial velocity axis allows determination of both the magnitude of the radial velocity of the transiting exocomets and their direction of travel with respect to the Earth (from the sign of the computed value of the radial velocity).

3.2.2 Production of a Reference Spectrum

Once the wavelength axis of the spectra had been converted to a velocity axis , the next step was the production of a reference profile for each of the orders 143 and 144. The reference profile serves as an estimate of the stellar profile without variable absorptions and is used to produce normalised profiles for specific observational spectra. In this case, it was decided to not include the circumstellar feature at the radial velocity of the star in the reference profile which is prominent on every spectrum. This was done to also allow analysis of the variability of the circumstellar feature across 2017. The reference profile allows detection of absorption features as any deviations of stellar spectra from the reference profile for a specific observational night are manifested as variable absorp-

tion features in the corresponding normalised profiles. These absorption features allow detection of transiting comets according to the falling evaporating bodies model.

Ideally, a reference profile would be produced using stellar spectra which show little to no evidence of variable absorptions. However, due to the fact that β Pic is an active star, and as there was a lack of any such spectra, it was decided that in order to produce a reference profile, a median spectrum would be produced across all observations for each of the orders and this median spectrum would be fitted via piecewise cubic spline interpolation. In order to perform the cubic spline interpolation, specific points were selected on the median spectrum while ignoring the circumstellar feature and the absorption features and these points were then fitted via cubic spline interpolation. This procedure was repeated multiple times to get the best possible reference profile. Using the initial reference profiles, artificial emission features were visible on various of the normalised profiles corresponding to specific nights indicating an inappropriate reference profile. It was attempted to minimize these emission features by making a reference profile which minimizes or eliminates the emission features of the worst fitted nights.

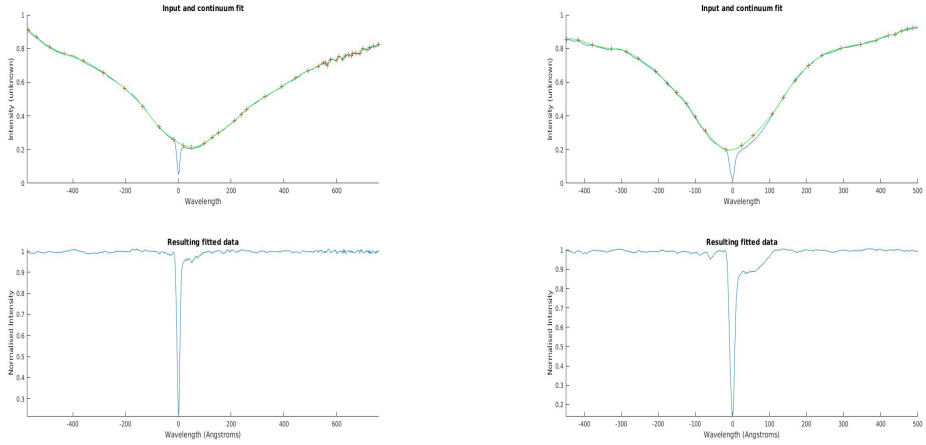

(a) Production of reference profile for H line (b) Production of reference profile for K line

Figure 3.7: Figures showing the production of reference profiles for the Ca II H & K lines by performing piecewise cubic spline interpolation on the median spectrum for orders 143 and 144

Figure 3.8 shows the initial reference profile used for order 144 and Figure 3.9 shows

worst resultant fitted nights showing strong artificial emission features in the region where red-shifted absorption features are expected and corresponding new normalised profiles obtained after applying the new reference profile which show the expected red shifted absorption features.

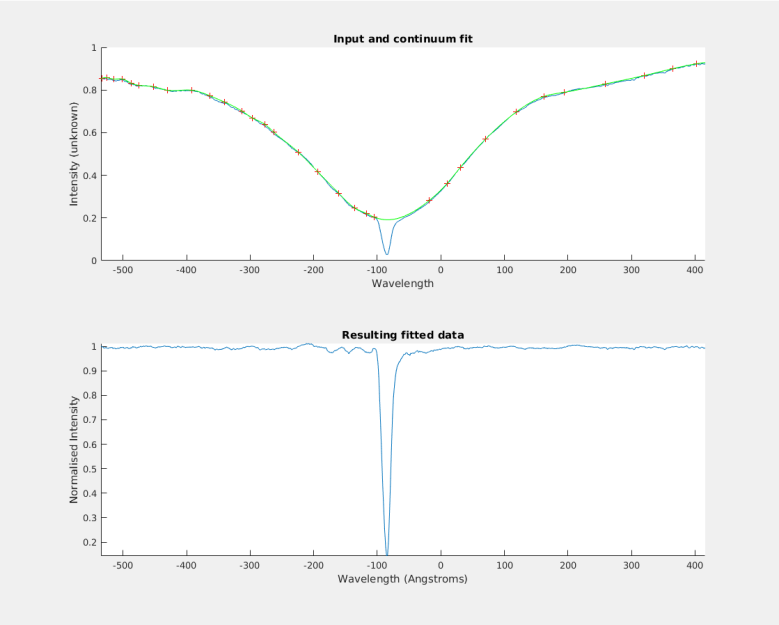

Figure 3.8: Figure showing the performed cubic spline interpolation on the median spectrum for order 144 to produce the initial reference profile with the bottom panel showing the corresponding normalised profile for the median spectrum across all observations.

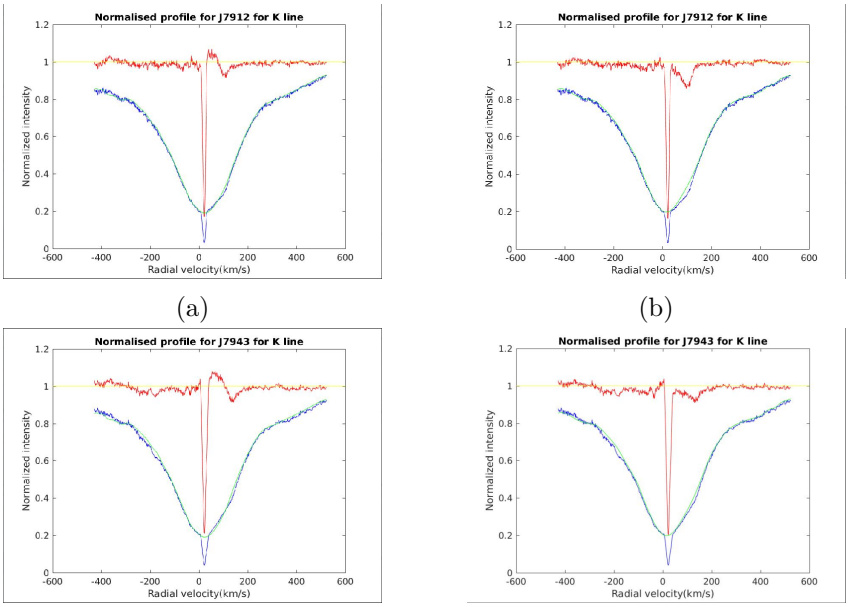

Figure 3.9: Figures (a) and (b) show the K-line normalised profiles for 9^{th} June 2017 obtained after applying the initial and new reference profiles for order 144 and figures (c) and (d) show the K-line normalised profiles for 13^{th} July 2017 obtained after applying the initial and new reference profiles for order 144 .

3.2.3 Production of normalised profiles

In this step, the observed spectra were divided by the correponding reference profile in order to produce normalised profiles. For the purposes of examining the annual variability of β Pic, all the spectra taken on a specific night were grouped together and the median spectrum corresponding to a specific night was produced. This improved the signal to noise ratio of the median spectrum and the long-term evolution of the different absorption features could be examined throughout 2017. However, as a relatively large number of spectra of β Pic were taken on some of the later nights in 2017, the observations for one of these nights were individually fitted to observe the short term evolution of the different features (which generally have an evolutionary time of a few hours). Once the median spectrum for a specific night was divided by the reference profile corresponding to that order, the produced normalised profiles showed evidence of variable absorption features, predominantly red-shifted features as expected.

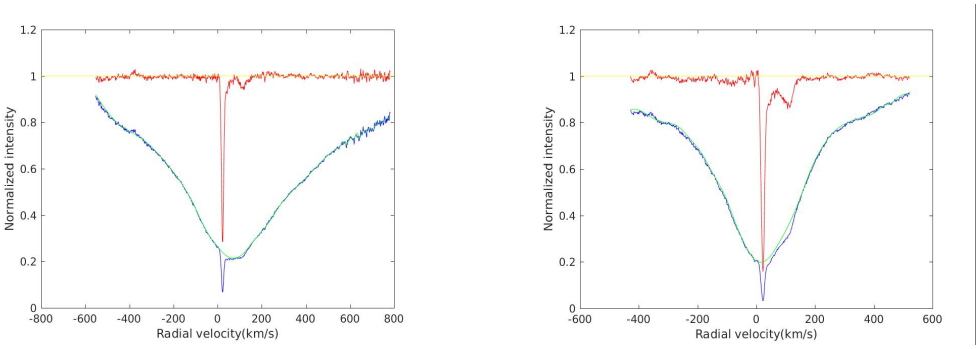

(a) Normalised profile for H line (b) Normalised profile for K line

Figure 3.10: Figures showing the obtained normalised profile(in red) for 5th June 2017 after dividing the obtained median spectrum for the night (in blue) with the reference profile (green)

3.2.4 Fitting the absorption features

Once the normalised profiles had been produced for every night, the next step was fitting the normalised profiles using sums of Gaussians with each Gaussian corresponding to a specific absorption feature. Gaussians were used previously by authors such as Lagrange-Henri et al.(1996) [2], Petterson et al. (1999) [3],Persson (1998) [4] ,Barnes et al.(2000) [7] and Kiefer et al.(2014) [6] and have been found to fit the absorption features adequately. Gaussians were fitted to the H and K lines simultaneously with the radial velocity at peak depth and the FWHM of each Gaussian being shared parameters between the two lines, while the final fitted value for the depth of the Gaussians was allowed to vary between the lines. For the purposes of this thesis only those absorptions which occured in both the H and K lines were modelled.

To perform this procedure, the python package *scipy.optimize.curve_fit* was used which fits a function to the data in a least squares sense. The method used through the package to fit Gaussians to the normalised profiles was the *Trust Region reflective algorithm*, abbreviated as 'trf' which is an algorithm used for bound constrained minimization problems. In order to perform the fit, initial values were provided for the FWHM, radial velocity and the depths of the two lines for the different absorptions from the saved MATLAB .fig files for the different normalised profiles, and these values were iterated over until the best possible Gaussian parameters were obtained for the chosen absorptions. The initial values for the radial velocity and the FWHM for the different absorptions

were provided using the absorptions in the K line, which has a higher oscillator strength compared to the H line.

Once the absorptions were fitted, the individual fitted Gaussians and overall fit (sum of the Gaussians) was overlayed on the spectrum to check the validity of the fit. Figure 3.11 shows an example of a fit performed for a specific night:

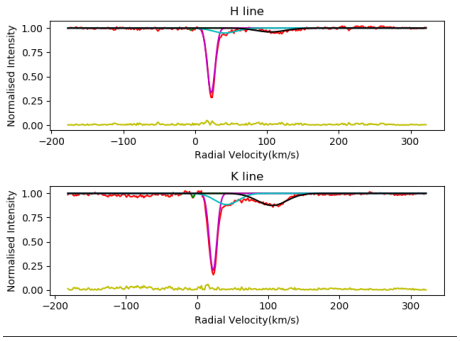

(a) Individual Fitted Gaussians

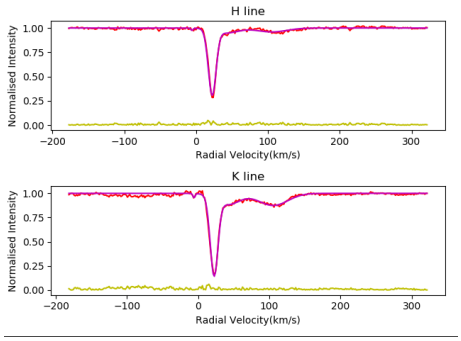

(b) Overall Fit

Figure 3.11: Figures showing the fitted Gaussians to the normalised profile for 5th June 2017

This same procedure was repeated for each individual night and each individual observation for a specific chosen night. The errors obtained on the fitted parameters were estimated from the covariance matrix obtained after performing the fit. As the absolute errors on the intensities are not known and are assumed to be equal to each other('unweighted'), the relative values of sigma on each of the intensities was assumed to be equal to one, and the errors on the parameters were estimated by demanding that the reduced chi squared value of the fit equals unity.

3.2.5 Characterising the absorptions

Once satisfactory fits were obtained, they were quality classified according to how well the python *curve_fit trf* procedure fitted the absorptions and how blended the absorption features were. This follows similar analysis by Petterson et al.(1999) [3], Persson (1998) [4] and Barnes et al.(2000) [7]. The classifications used are shown in Table 3.1 with Figs 3.12 to 3.16 showing examples of the different classifications. With the absorptions all identified and fitted, the next step was the calculation of the equivalent width (E.W.)

of each absorption which serves as an estimate of the strength of each absorption. The equivalent width of a Gaussian is defined as the area of the Gaussian when the height of the Gaussian is measured relative to the local pseudo-continuum. Given the expression of a Gaussian (Equation 3.2), where c is the full width at half maximum (FWHM) and a is the depth, after integrating the Gaussian function from $-\infty$ to $+\infty$ to find the area under the curve, we obtain an expression for the area of the Gaussian in terms of the depth and the standard deviation (Equation 3.3) :

$$Gaussian = a * e^{\frac{-(x-b)^2}{2*\sigma^2}} \tag{3.2}$$

$$\begin{aligned} Areaof Gaussian &= \int_{-\infty}^{+\infty} ae^{\frac{-(x-b)^2}{(2c^2)}} \mathrm{d}x \\ &= a\sigma\sqrt{2\pi} \end{aligned} \tag{3.3}$$

Now from [84],

$$\sigma = \frac{FWHM}{2\sqrt{2\ln 2}} \tag{3.4}$$

Table 3.1: Table showing the classification scheme used for the fitted Gaussians to the different absorptions.

Abbreviation	Description
gS	'Good Single': an absorption that (possibly) no more than slightly overlaps with another and is well-fitted by a Gaussian profile.
pS	'Poorer Single': an absorption that (possibly) no more than slightly overlaps with another and is a poorer fit to a Gaussian profile, either because the spectrum is noisy or because the profile is obviously non-Gaussian.
gB	'Good Blend': an absorption that clearly overlaps with one-or-more others and is well-fitted by a Gaussian profile.
pB	'Poorer Blend': an absorption that clearly overlaps with one-or-more others and is a poorer fit to a Gaussian profile, either because the spectrum is noisy or because the profile is obviously non- Gaussian.
UD	'Uncertain Decomposition': the feature has been fitted by a single Gaussian, but the signal-to-noise ratio is insufficient to determine whether more Gaussians would be a better fit.

Hence, by substituting the value of σ into the expression for the area of Gaussian,we get the expression for E.W of a Gaussian:

$$E.W. = \frac{ac}{2} * \frac{\sqrt{\pi}}{\ln 2} \tag{3.5}$$

The numerical factor here is 1.0645 ac. As a (the depth) is a fraction and hence unitless, the above computed E.W. would be the same units as c in kms^{-1}. However, in order to have the E.W. in mÅ which is the preferred unit, a further numerical factor must be

incorporated into Equation 3.5 as follows:

$$E.W. = 1.0645\frac{\lambda}{c}ac \tag{3.6}$$

Taking $\lambda = 3933633$ mÅ for the K line and 3968468 mÅ for the H line yielded factors of 13.96 for the K line and 14.09 for the H line. Taking a mean of the two values yielded a factor of 14.025 which was used to compute the E.W. for an absorption. Therefore the E.W. in mÅ of a given absorption can be found by:

$$E.W. = 14.025ac \tag{3.7}$$

The full table showing the final results for the different absorptions listing the associated classifications and the obtained values for the different parameters: depth, FWHM, radial velocity at peak depth and E.W. with the corresponding errors can be found in Table A.1 in the Appendix. The errors on the equivalent width was estimated by treating the errors on the depth, a and the FWHM, c as independent and adding them in quadrature.

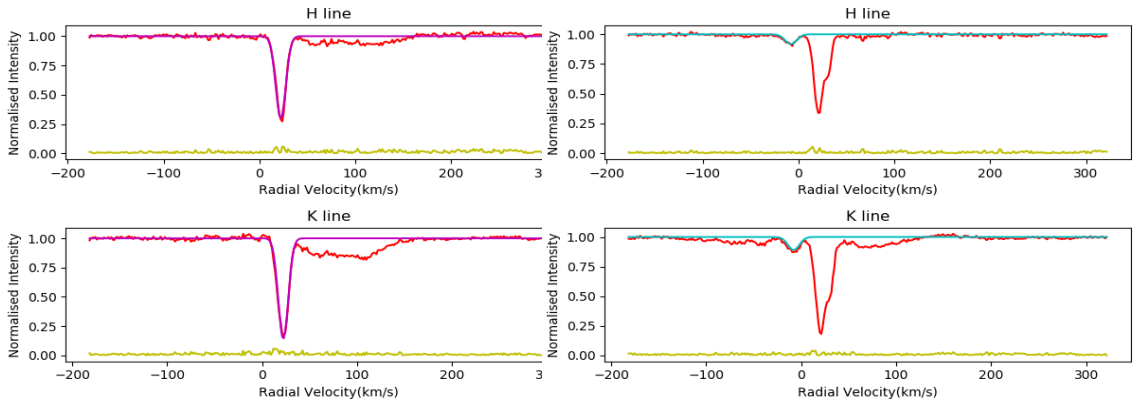

(a) (b)

Figure 3.12: Figures (a) and (b) show examples 'good single' absorptions as obtained on 6^{th} June 2017 and 8^{th} April 2017 respectively.

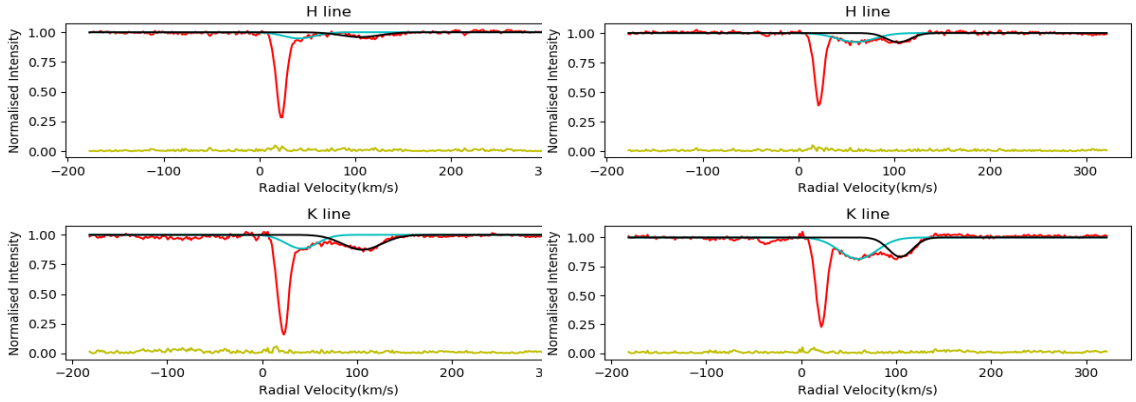

(a) (b)

Figure 3.13: Figures (a) and (b) show examples of 'Good blend' absorptions as obtained on 5^{th} June 2017 and 13^{th} May 2017 respectively.

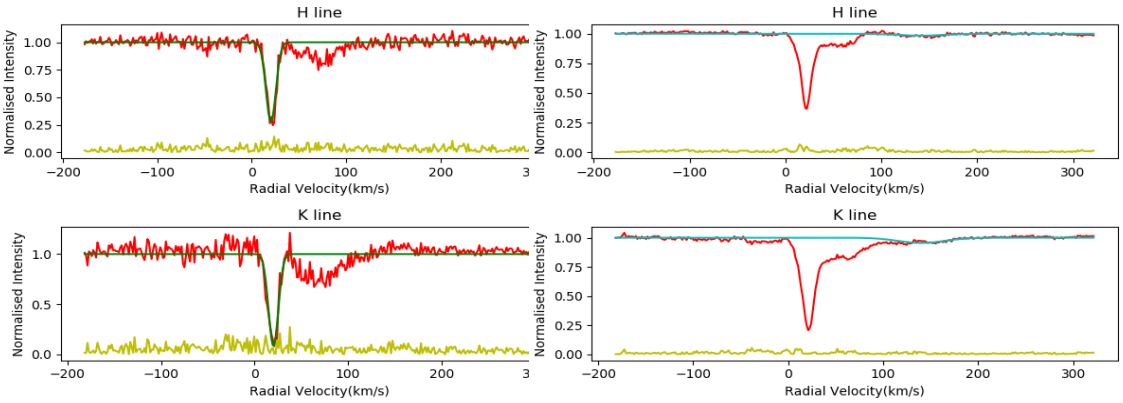

(a) (b)

Figure 3.14: Figures (a) and (b) show 'poorer single' absorptions as obtained on 8^{th} July 2017 and 15^{th} May 2017 respectively. Absorption shown in (a) is classified as 'pS' due to the noisy nature of the circumstellar feature which is poorly fit by the fitted Gaussian. Absorption shown in (b) is classified as such solely due to the Gaussian being a poor fit to the absorption despite the relatively low S.N.R of this profile.

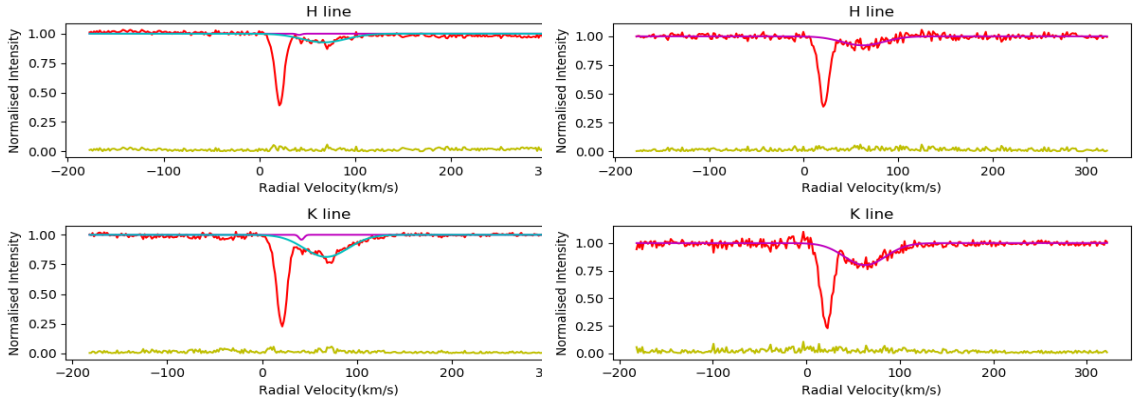

(a) (b)

Figure 3.15: Figures (a) and (b) show examples of 'poorer blended' absorptions as obtained on 12^{th} May 2017 and 14^{th} May 2017 respectively. The absorptions in (a) are classified as such due to the inability of the python *curve_fit trf* procedure to better fit the identified absorptions. Absorption in (b) is blended with the circumstellar feature but is too noisy to be classified as a 'gB' absorption.

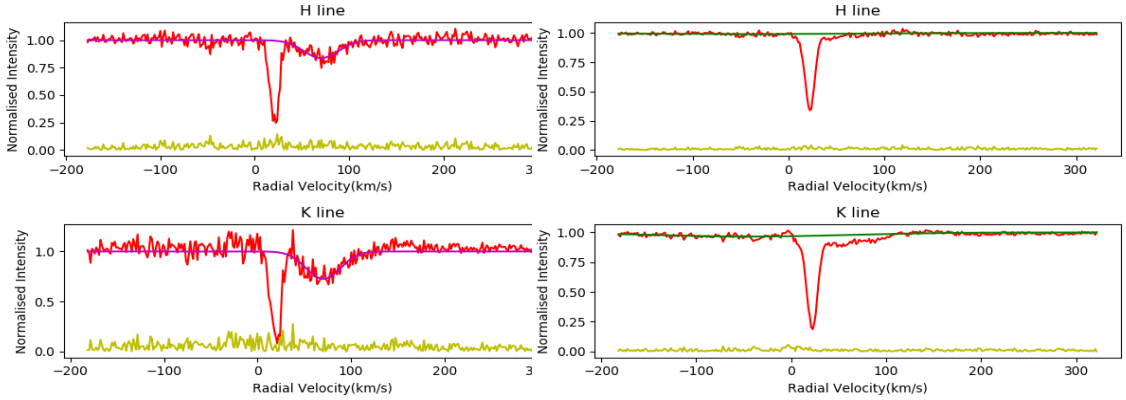

(a) (b)

Figure 3.16: Figures (a) and (b) show absorptions classified as 'uncertain decomposition' absorptions as identified on the 8^{th} of July 2017 and 18^{th} of May 2017. The absorption is (a) is a single absorption but due to its noisy nature it is not clear whether it is a single absorption or multiple absorptions. The absorption in (b) is fitted as a single 'blue-shifted' absorption but due its noisy nature , it is not clear whether it it actually a 'single' absorption or 'multiple' absorptions.

CHAPTER 4

Presentation of Spectra

In this chapter the produced median spectra for the different nights and the individual observed spectra for a list of selected nights is presented along with the corresponding reference profile used. Also, in Section 4.1, the different orders identified as relevant for analysis for the Ca II H & K lines are plotted across all observations.

4.1 Plots of relevant orders across all observations

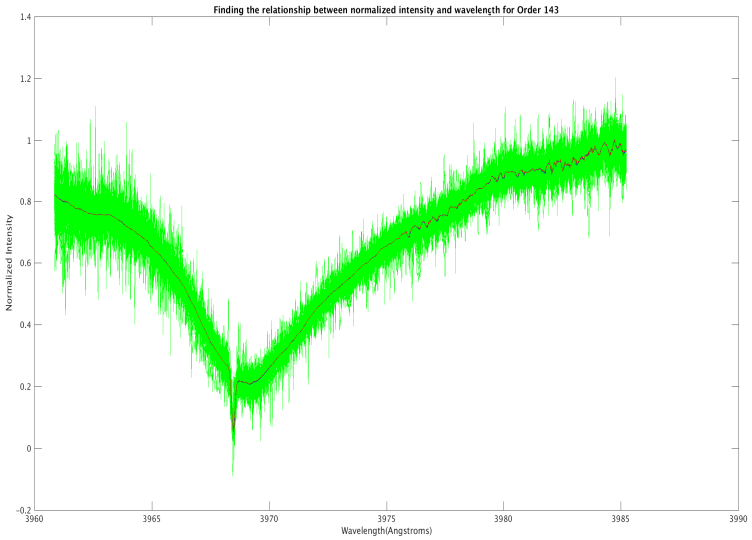

Figure 4.1: Order 143 plotted across all observations (in green). The median spectrum is plotted in red. Note the asymmetric nature of the order which can be attributed to the blending of the Ca II H line with the Hydrogen ϵ line.

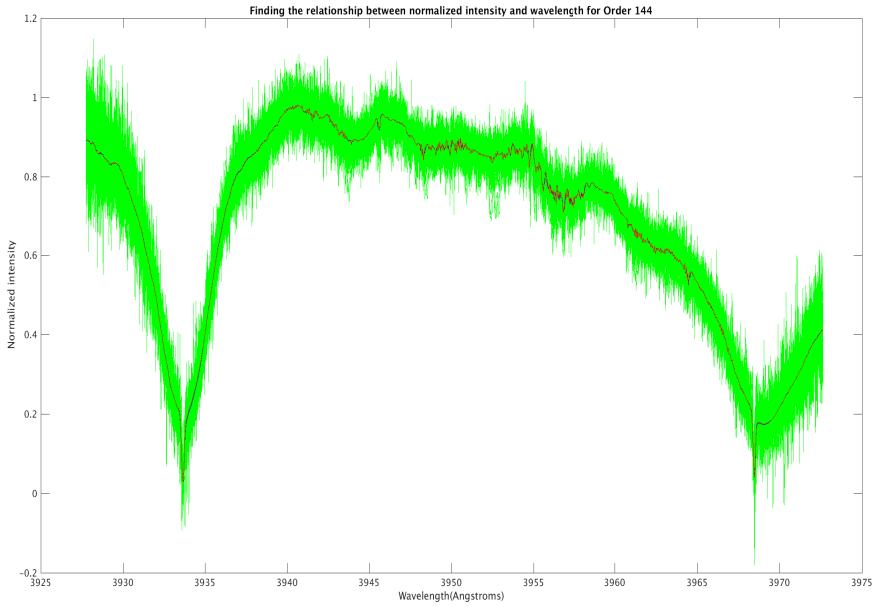

Figure 4.2: Order 144 plotted across all observations (in green). The median spectrum is plotted in red. Note that the data is missing towards the higher wavelengths (H line) which led to the use of this order only for the analysis of the Ca II K line and not for the H line.

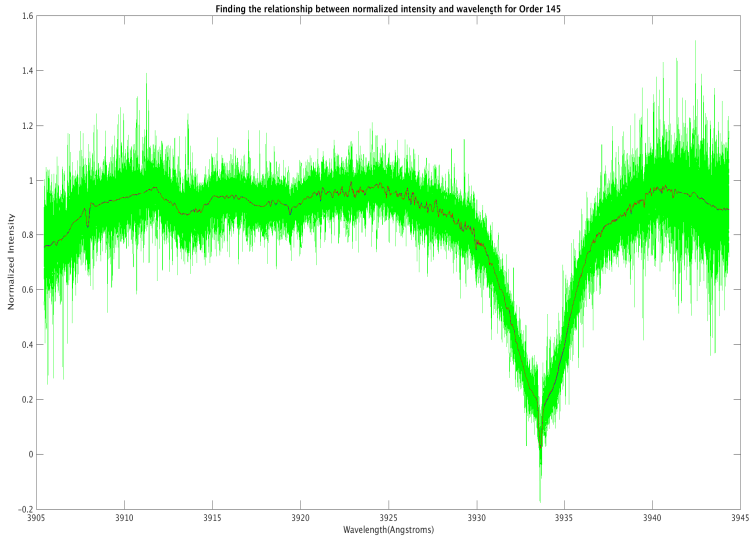

Figure 4.3: Order 145 plotted across all the different observations (in green). The median spectrum is plotted in red. Note the higher noise level in this order which is visible from the greater vertical extent of the observations for this order.

As Figure 4.2 shows, order 144 was selected for analysis of the Ca II K line due to the relatively lower noise level for this order compared to order 145. Although there was no formal calculation of the signal to noise ratio for the different orders, the script *prepare_for_famiasv2.m* estimates a similar quantity termed as *weights* which is calculated by first applying an eleventh order median filtering on the normalised spectra and then taking the inverse of the standard deviation of the corresponding residuals for each observation. This quantity (*weights*) is similar to the S.N.R in that the lower the value of this quantity for a specific observation, the higher the noise level for that specific observation. The average values computed for the weights for orders 143, 144 and 145 were 77.0020, 78.8019 and 60.7614 respectively which supported the selection of order 144 for analysis of the Ca II K line.

4.2 Night median spectra

In this section, the median spectrum for the different nights are plotted on top of each other while the bottom spectrum (in green) represents the reference profile used for the specific line.

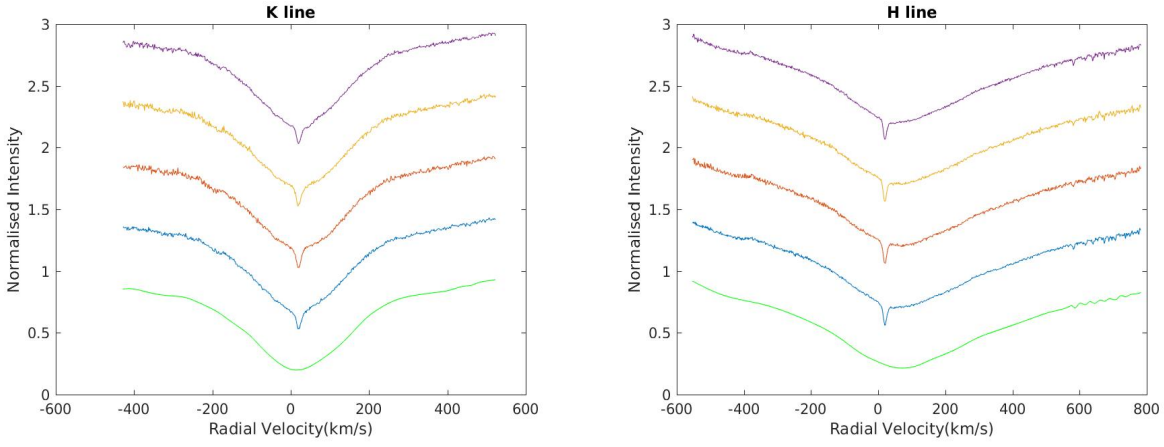

(a) (b)

Figure 4.4: Median Spectra plotted for the first four nights used (12^{th} January 2017 to 16^{th} January 2017) (in increasing chronological order from bottom to top). Figure (a) and (b) show the spectra for K and H lines respectively.See Table 2.1

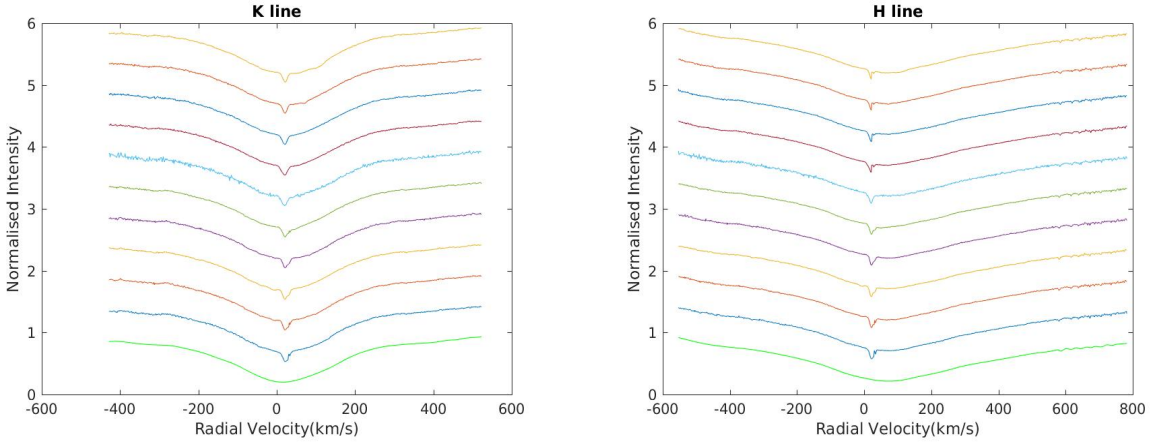

(a) (b)

Figure 4.5: Median spectra for next ten nights used for analysis (6^{th} April 2017 - 14^{th} May 2017) (in increasing chronological order from bottom to top). Figures (a) and (b) show the spectra obtained for the K and H lines respectively. See Table 2.1

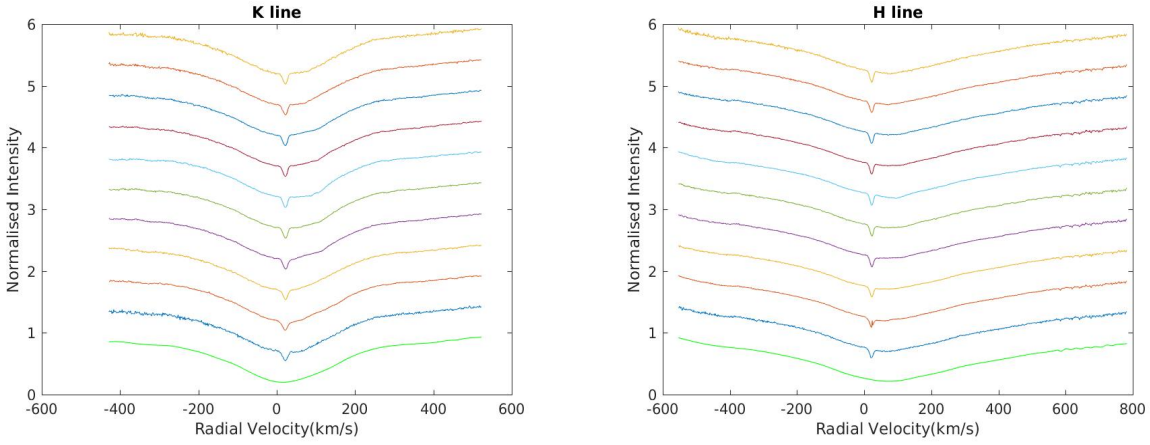

(a) (b)

Figure 4.6: Median spectra for next ten nights used for analysis (6^{th} April 2017 - 14^{th} May 2017). Figures (a) and (b) show the spectra obtained for the K and H lines respectively. See Table 2.1

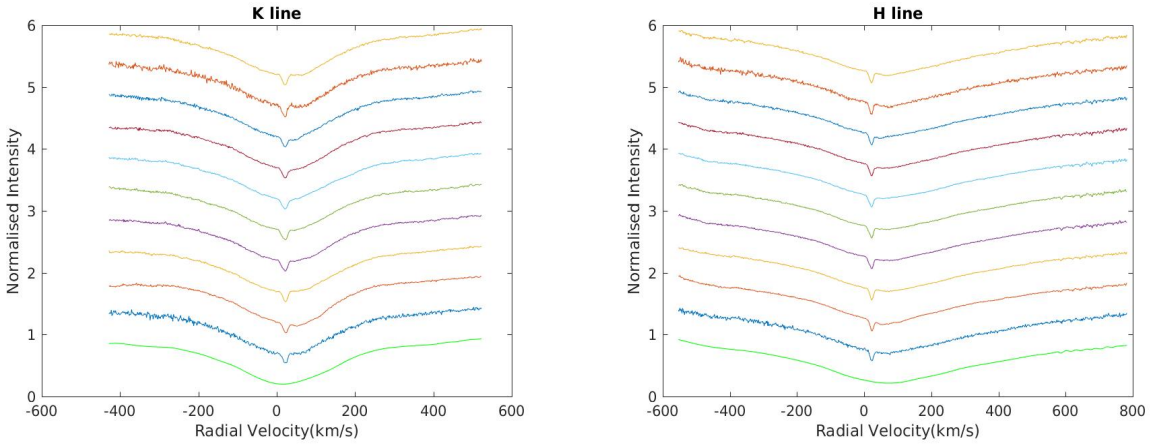

(a) (b)

Figure 4.7: Median Spectra for next ten nights used for analysis (6^{th} April 2017 - 14^{th} May 2017). Figures (a) and (b) show the spectra obtained for the K and H lines respectively. See Table 2.1

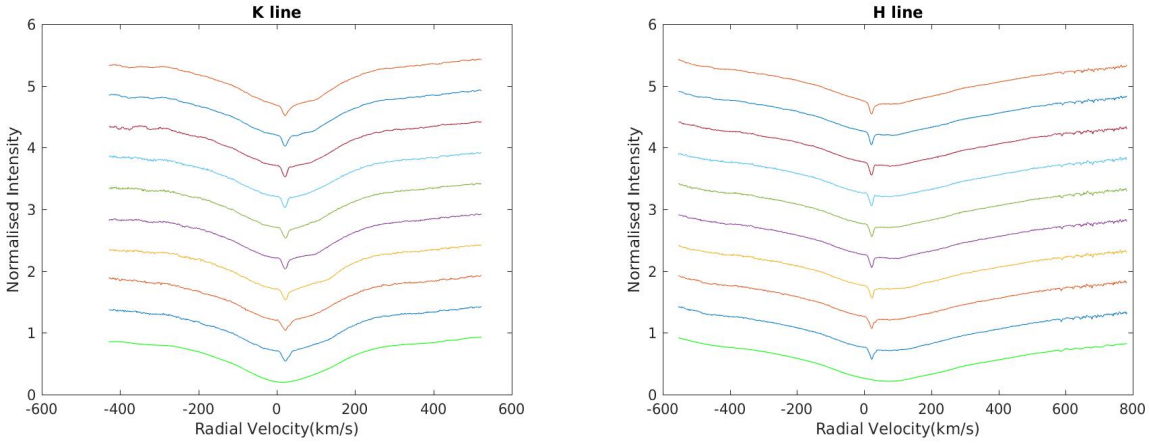

(a) (b)

Figure 4.8: Median Spectra for next ten nights used for analysis (6^{th} April 2017 - 14^{th} May 2017). Figures (a) and (b) show the spectra obtained for the K and H lines respectively.See Table 2.1

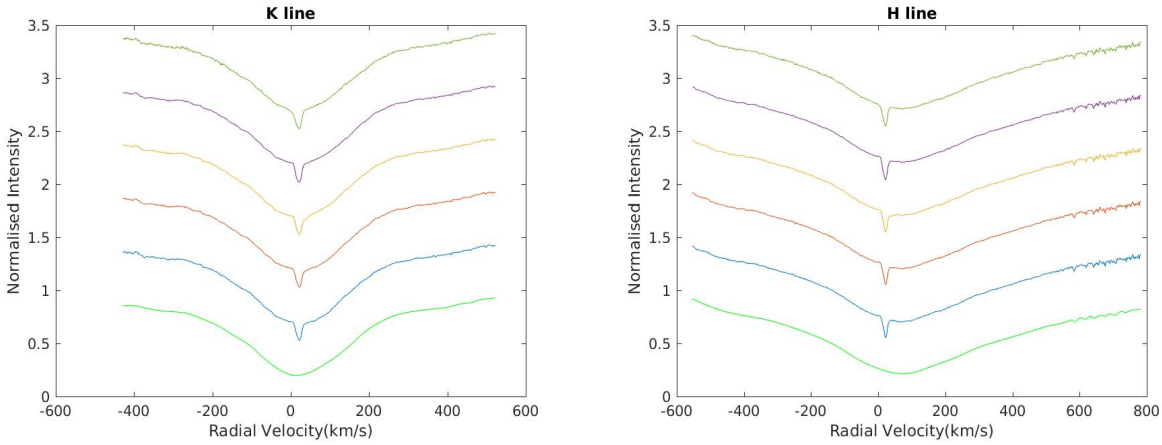

(a) (b)

Figure 4.9: Median Spectra for the last five nights used for analysis (4^{th} December 2017 - 9^{th} December 2017). Figures (a) and (b) show the spectra obtained for the K and H lines respectively. See Table 2.1

4.3 Individual observation spectra

In this section, the individual normalised observational spectra for a range of selected nights are plotted in a time sequence while the reference profile (in green) used for the specific absorption line is plotted at the bottom of each plot.

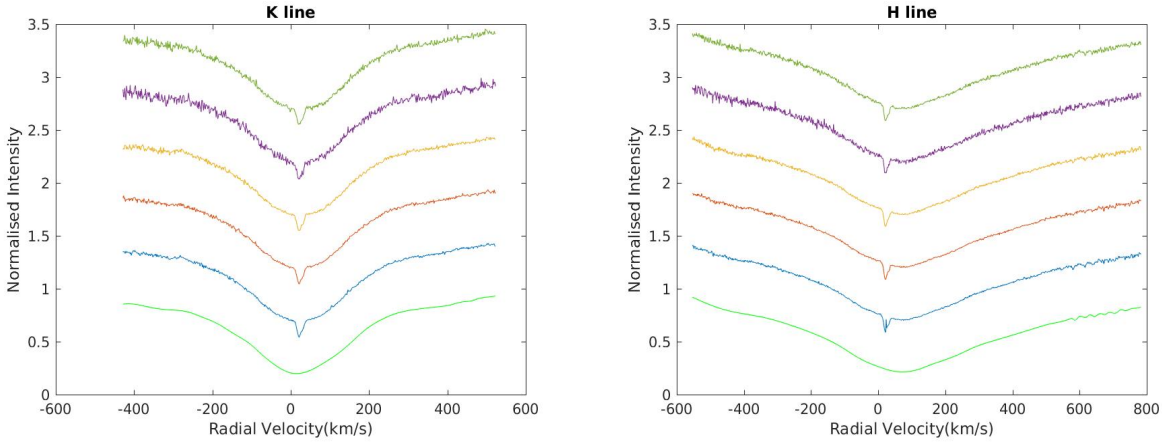

(a) Normalised spectra for H line (b) Normalised spectra for K line

Figure 4.10: Normalised spectra for observations taken on 9^{th} April 2017 (from bottom to top in chronological order).

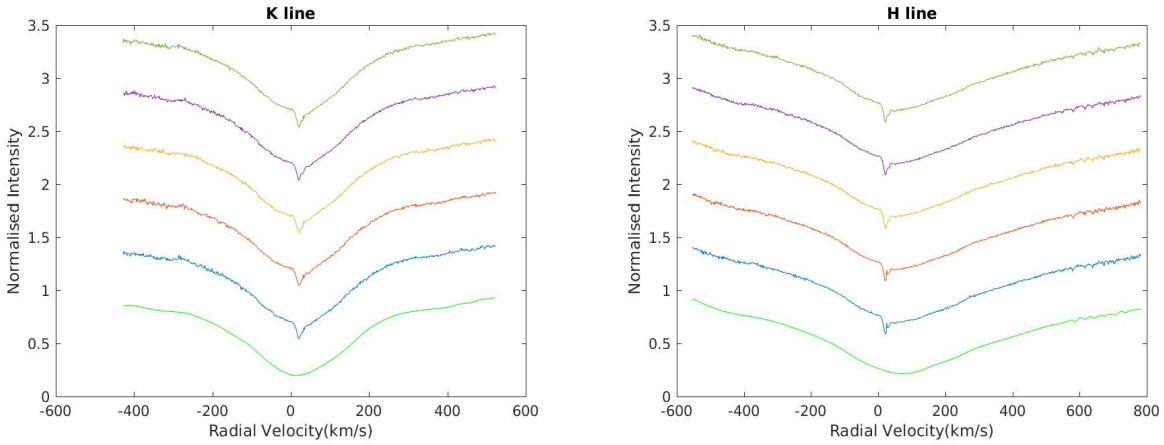

(a) Normalised spectra for H line (b) Normalised spectra for K line

Figure 4.11: Normalised spectra for observations taken on 10^{th} April 2017 (from bottom to top in chronological order).

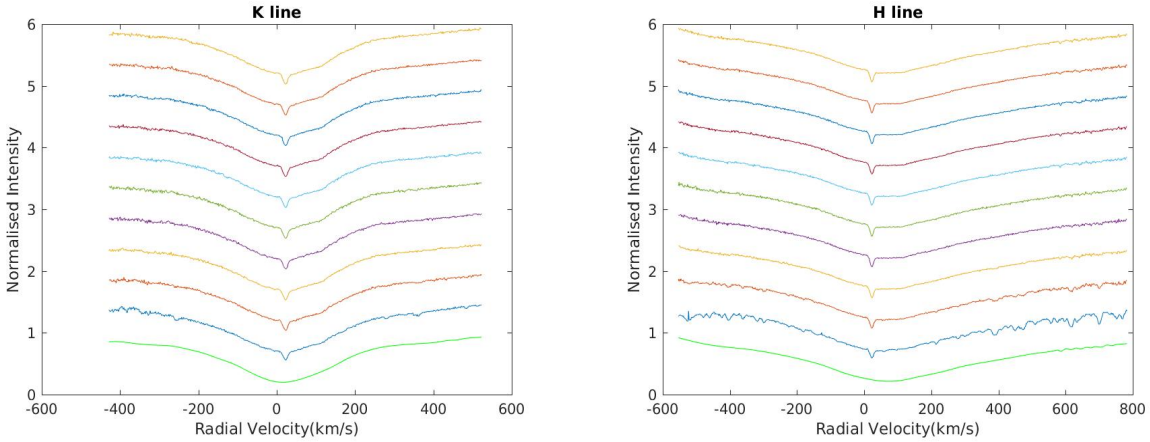

(a) Normalised spectra for K line (b) Normalised spectra for H line

Figure 4.12: Normalised spectra for observations taken on 4^{th} June 2017 (from bottom to top in chronological order)

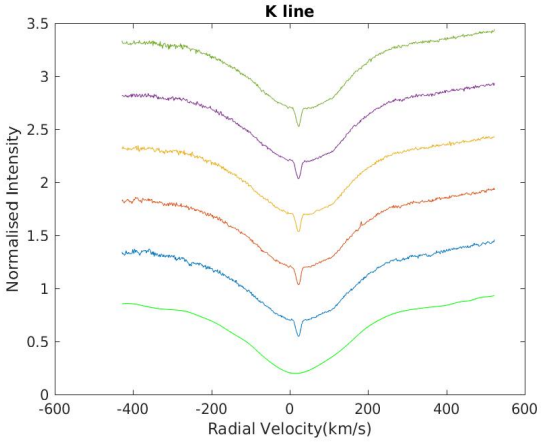

(a) Normalised spectra for K line

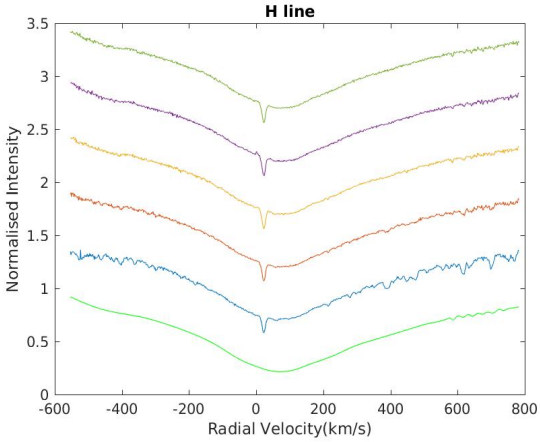

(b) Normalised spectra for H line

Figure 4.13: Normalised spectra for observations taken on 5^{th} June 2017 (from bottom to top in chronological order)

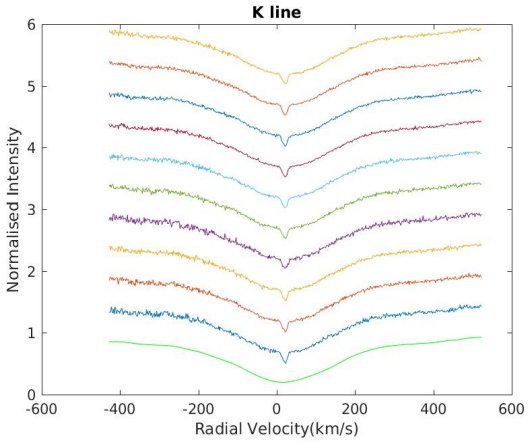

(a) Normalised spectra for H line

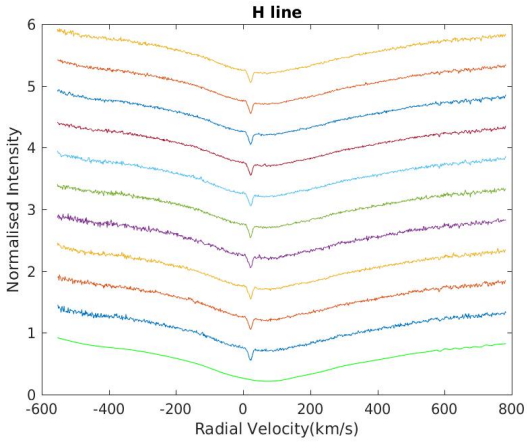

(b) Normalised spectra for K line

Figure 4.14: Normalised spectra for first 10 observations used for analysis taken on 4^{th} December 2017 (from bottom to top in chronological order).

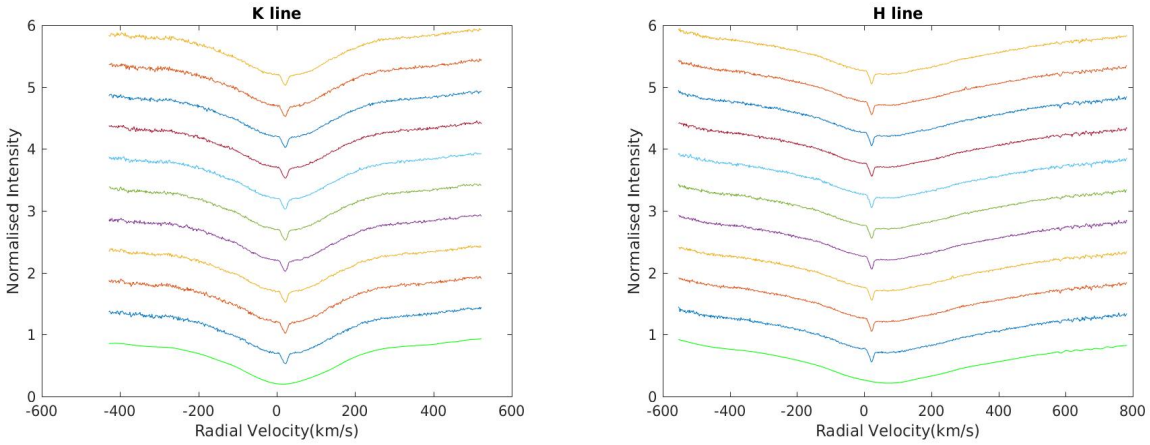

(a) Normalised spectra for H line (b) Normalised spectra for K line

Figure 4.15: Normalised spectra for next 10 observations used for analysis taken on 4^{th} December 2017 (from bottom to top in chronological order).

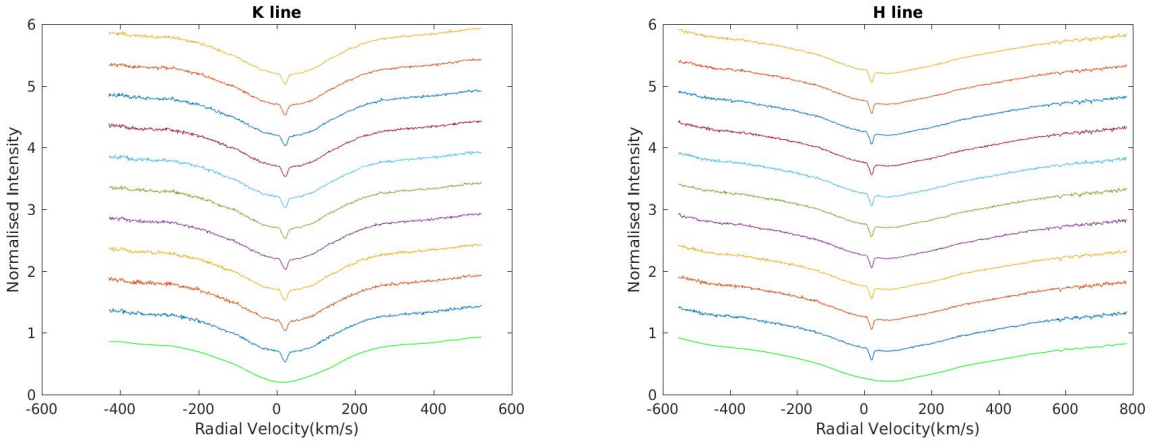

(a) Normalised spectra for H line (b) Normalised spectra for K line

Figure 4.16: Normalised spectra for next 10 observations used for analysis taken on 4^{th} December 2017 (from bottom to top in chronological order).

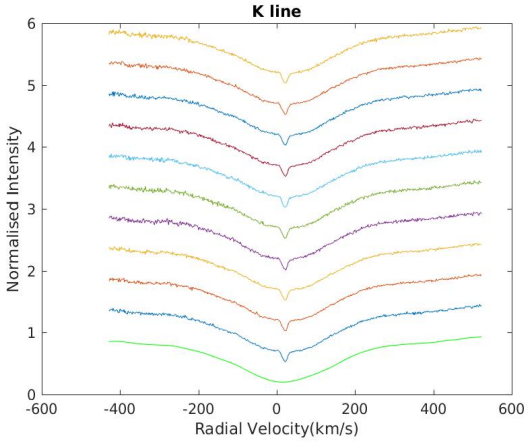

(a) Normalised spectra for H line

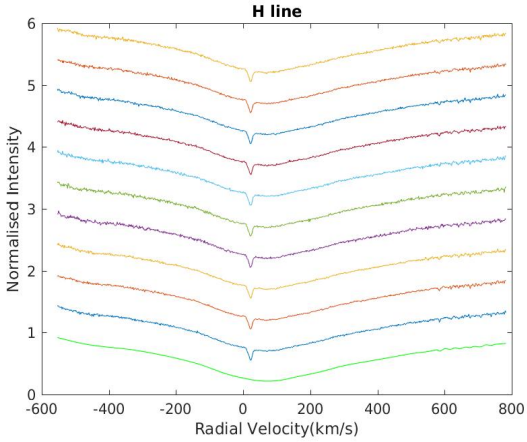

(b) Normalised spectra for K line

Figure 4.17: Normalised spectra for next ten observations used for analysis taken on 4^{th} December 2017 (from bottom to top in chronological order).

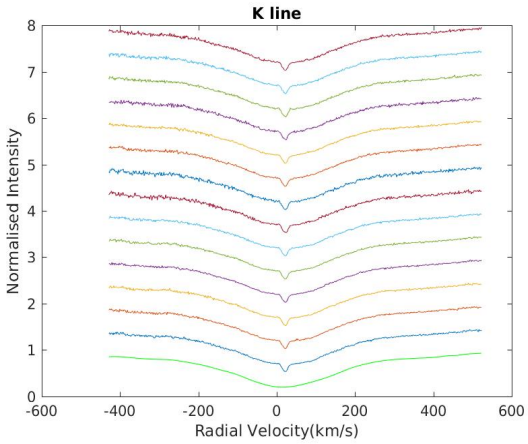

(a) Normalised spectra for H line

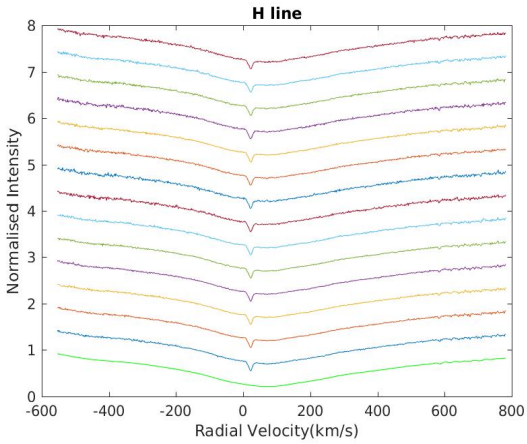

(b) Normalised spectra for K line

Figure 4.18: Normalised spectra for next 14 observations used for analysis taken on 4^{th} December 2017 (from bottom to top in chronological order).

CHAPTER 5

Analysis

5.1 Obtained parameters for all nights

A total of 155 variable absorptions were identified in both the H & K lines for the median spectra for the different nights and were fitted using Gaussians. The complete table showing all the obtained parameters for all fitted absorptions for the different nights across 2017 is shown by Table A.1 in the Appendix. The different absorptions can be characterised as follows :

- 21 absorptions classified as 'Good Singles'
- 80 absorptions classified as 'Good Blends'
- 28 absorptions classified as 'Poorer Singles'
- 24 absorptions classified as 'Poorer Blends'
- 2 absorptions characterized as 'Uncertain decompositions'

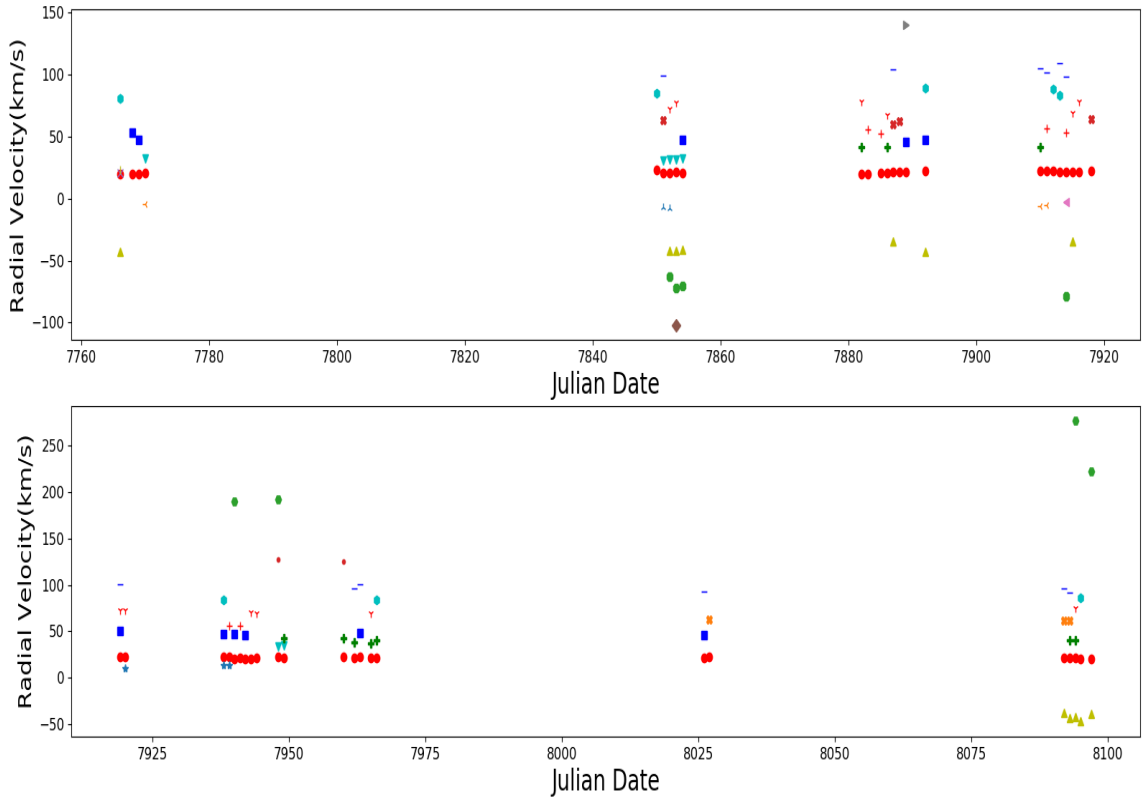

(a)

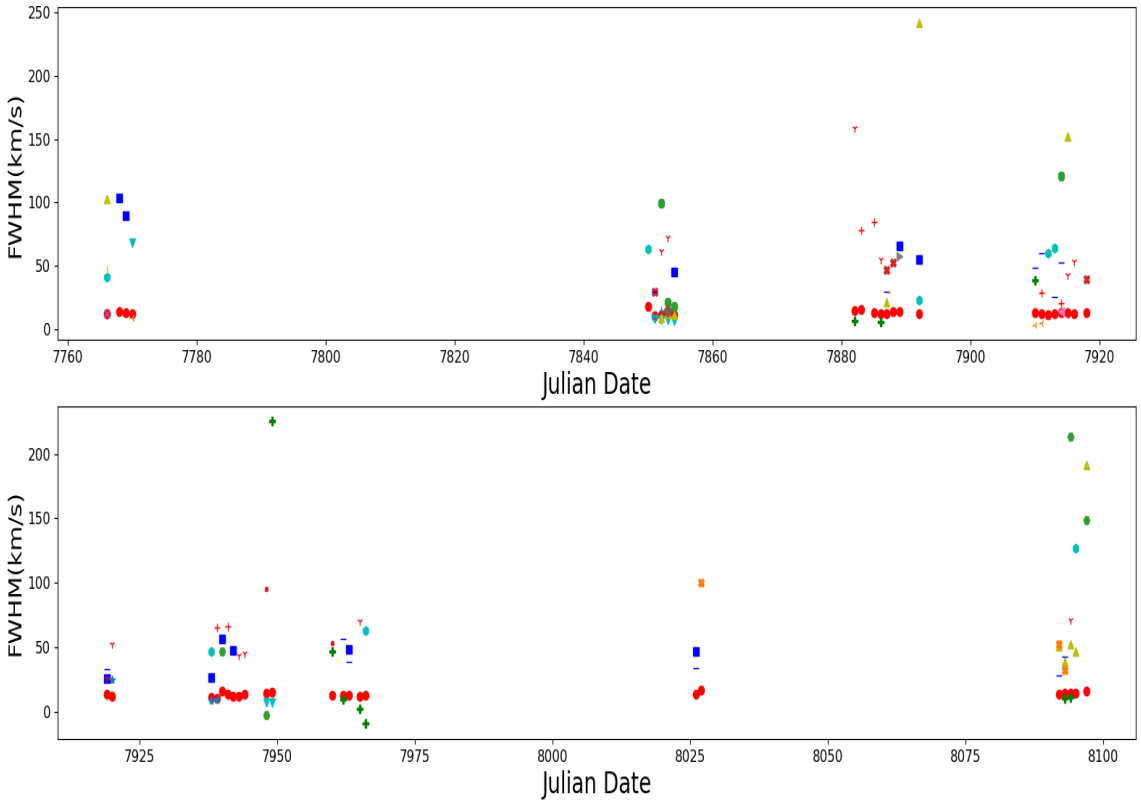

(b)

Figure 5.1: Figures (a) and (b show show the radial velocities and the FWHM of the different features plotted as a function of Julian Date.

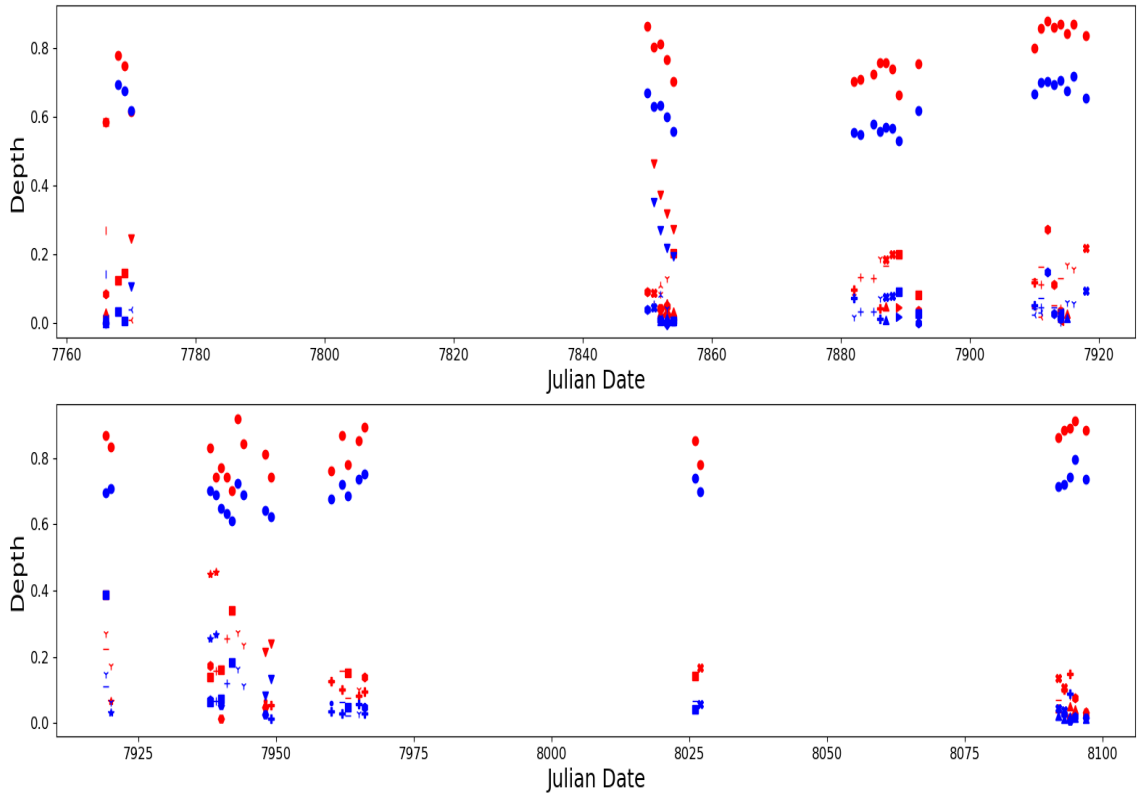

(a)

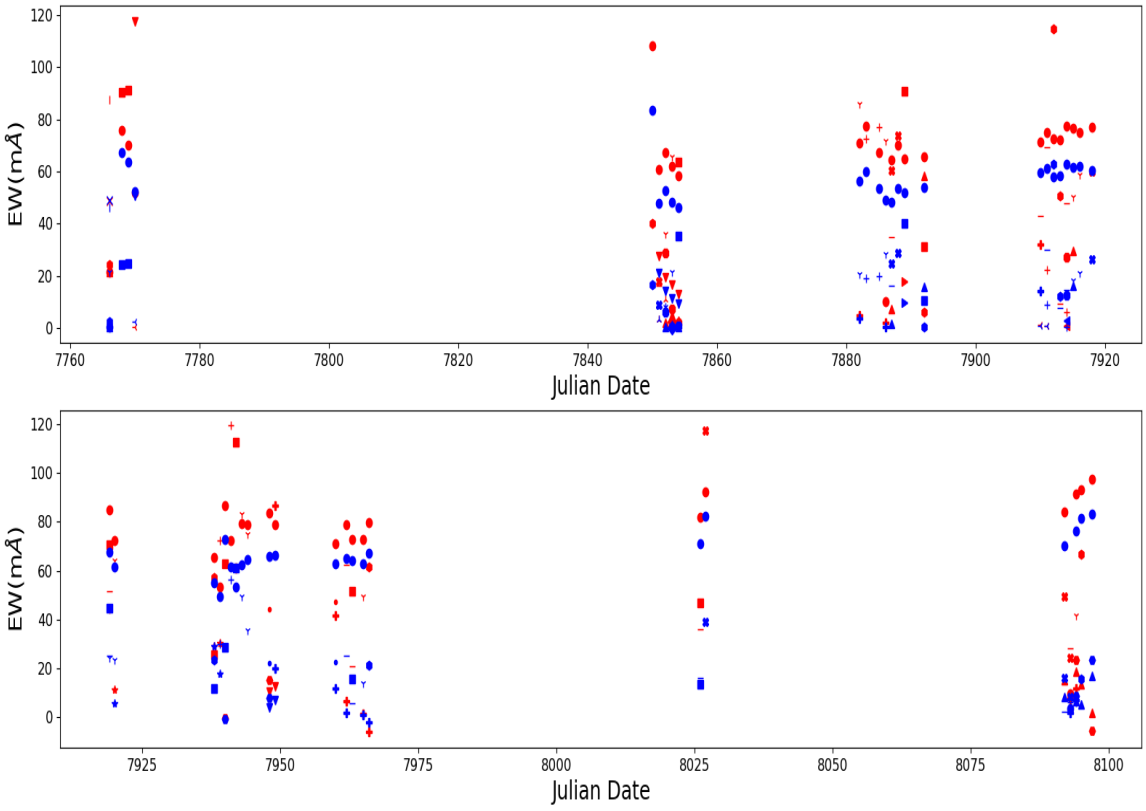

(b)

Figure 5.2: Figures (a) and (b) show the central depths and the E.W. of the different features plotted as a function of Julian Date. Red represents the K line absorptions while blue represents the H line absorptions. Note the K line absorptions have a higher value for the central depth and the E.W. for almost all absorptions.

In order to examine the variability of the absorption features in more detail, the different parameters were plotted and labelled with their respective Julian dates as shown in Figure 5.3.

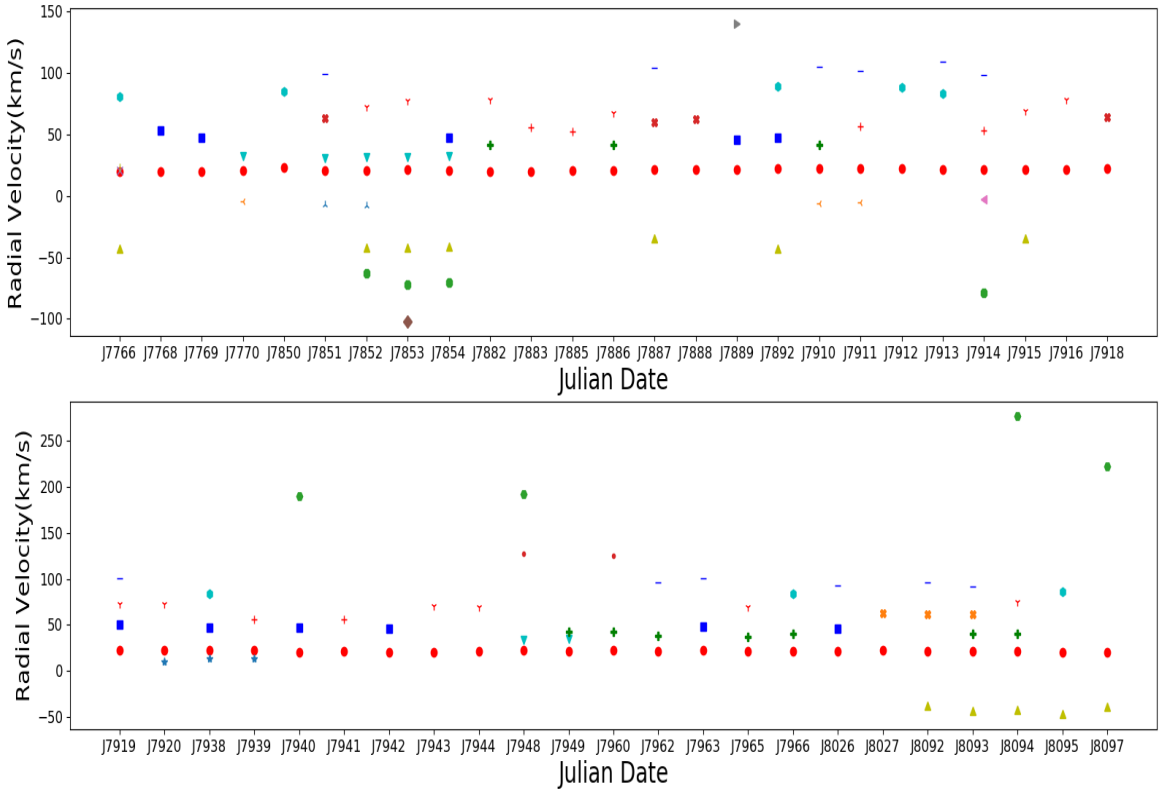

(a)

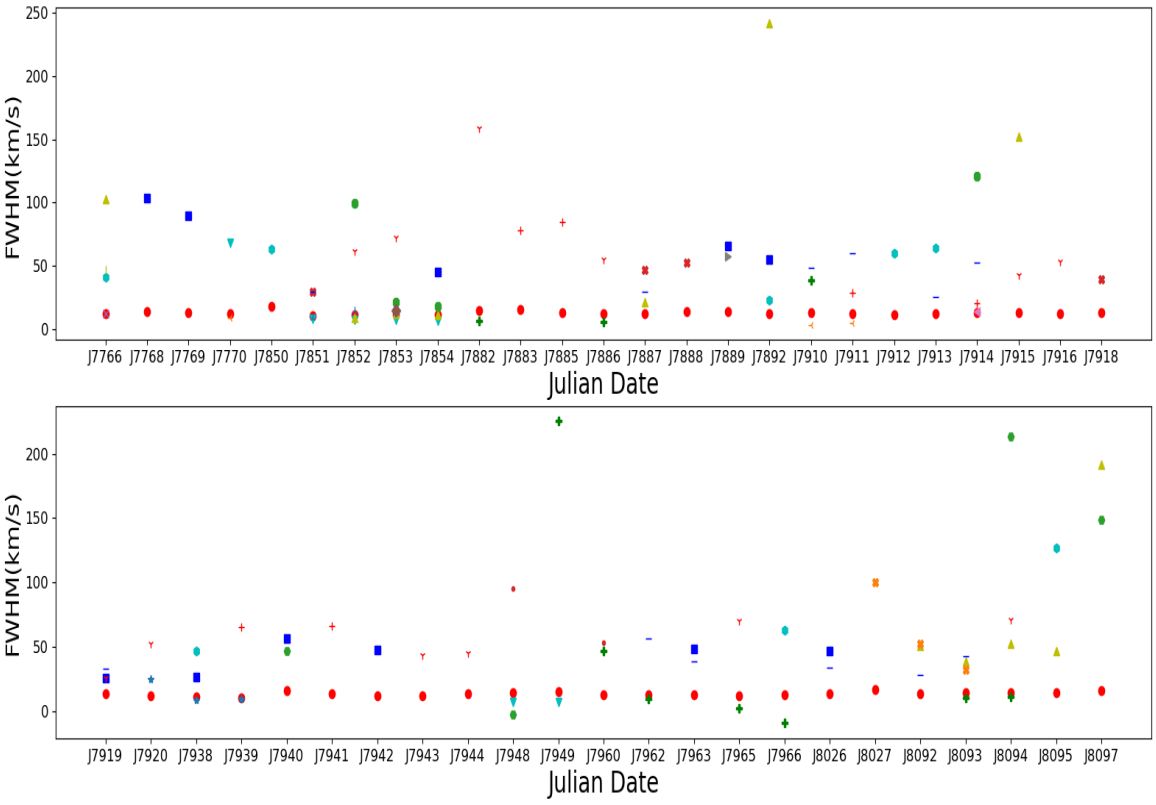

(b)

Figure 5.3: Figures (a) and (b show show the radial velocities and the FWHM of the different features plotted and labelled by Julian Date.

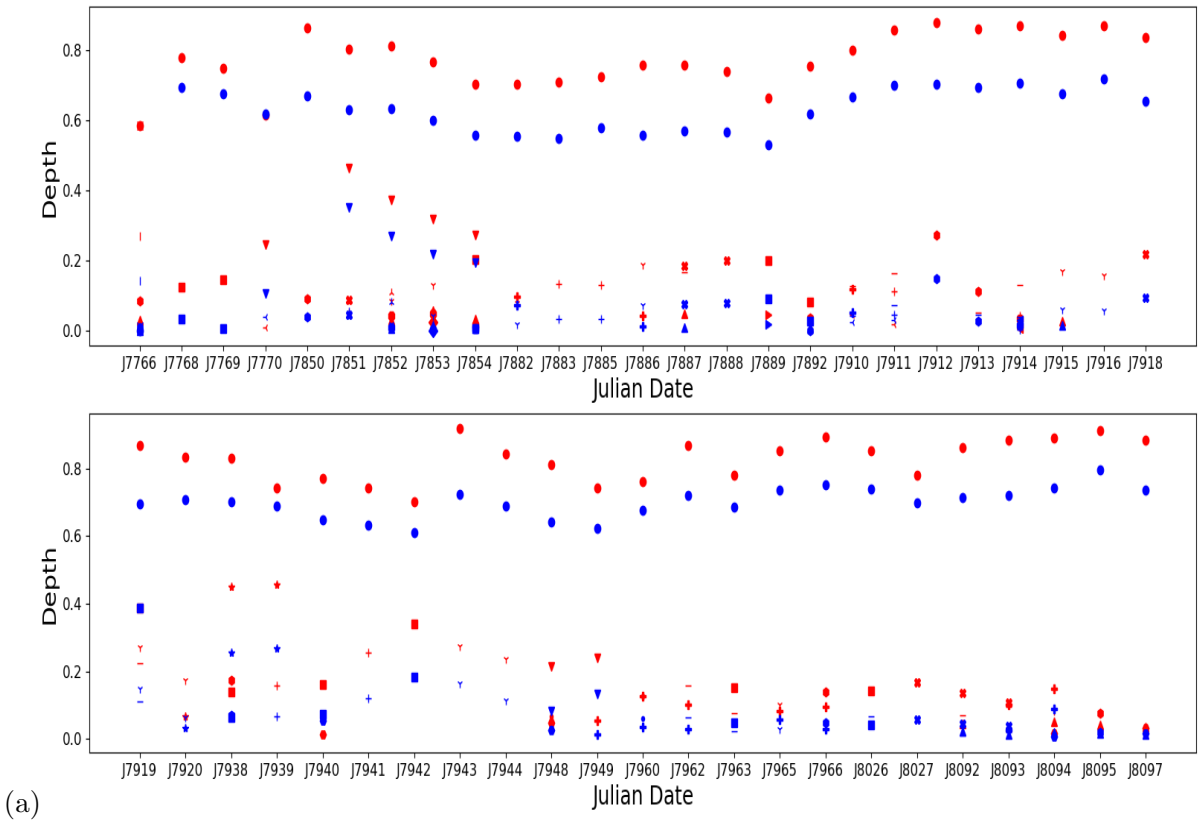

(a)

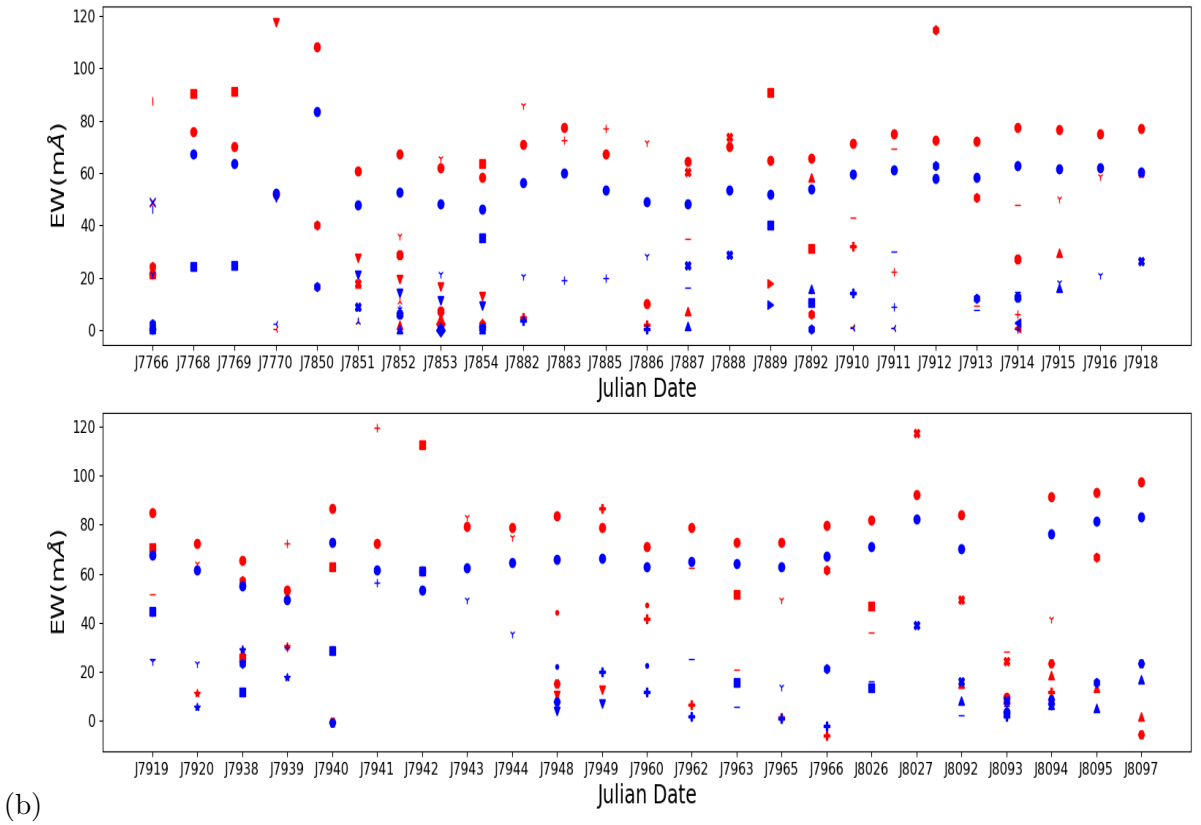

(b)

Figure 5.4: Figures (a) and (b) show the central depths and the E.W. of the different features plotted and labelled by Julian Date. Red represents the K line absorptions while blue represents the H line absorptions. Note the K line absorptions have a higher value for the central depth and the E.W. for almost all absorptions.

5.2 Obtained parameters for a specific night

The spectra collected on the night starting on the 3^{rd} of December 2017 (JD2458092) were analysed on an observation-by-observation basis in order to gain an insight into the variability timescales of the different features across a night. As the absorption features appearing in the median spectrum for the night were already fitted as part of the study of the variability of the features across 2017, the same python script was used to fit each individual spectrum while using the same initial Gaussian parameters for the different absorptions. This allowed us to examine the variation of the different parameters for each feature throughout the course of the night. Due to the fact that each individual observation had a lower signal-to-noise ratio compared to the median spectrum, some of the observations could not be fit with the same number of Gaussians and hence, were instead fitted with a lower number of Gaussians. The obtained parameters were plotted as a function of the Julian date on the specific night as shown in Figures 5.5 and 5.6.

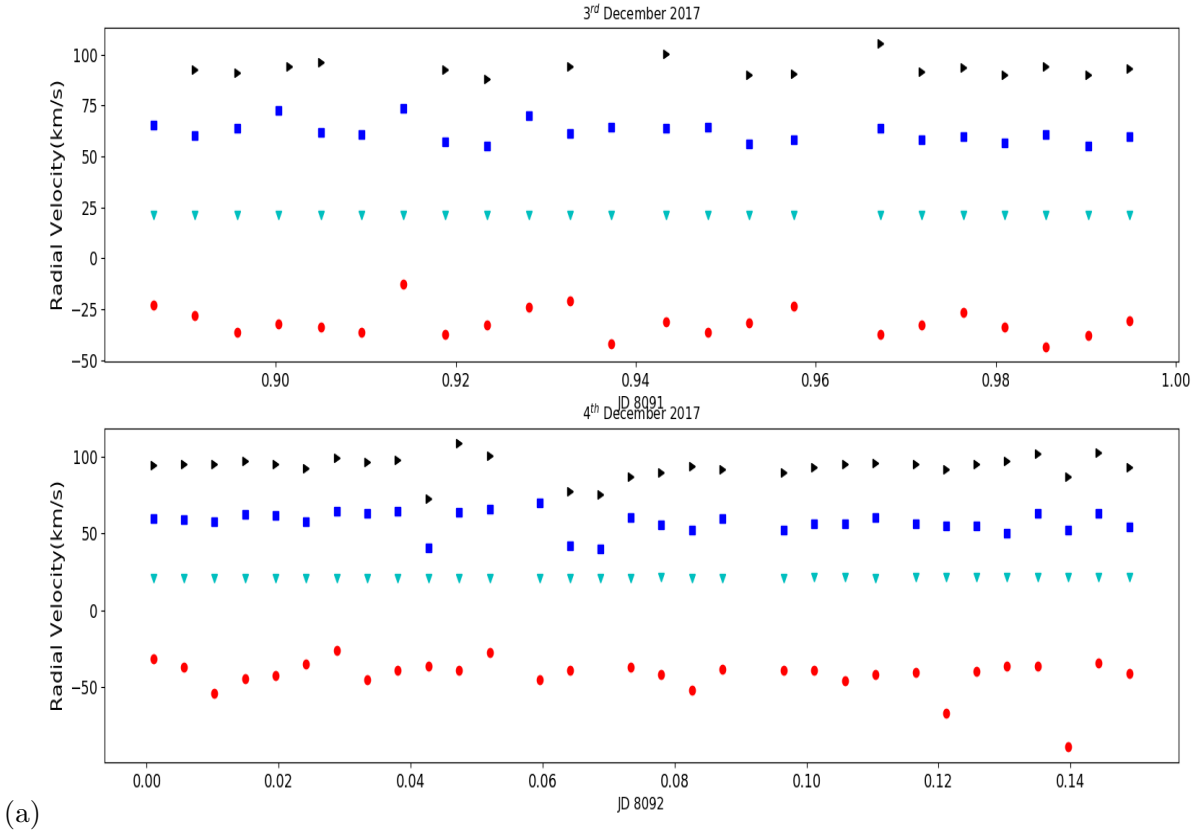

(a)

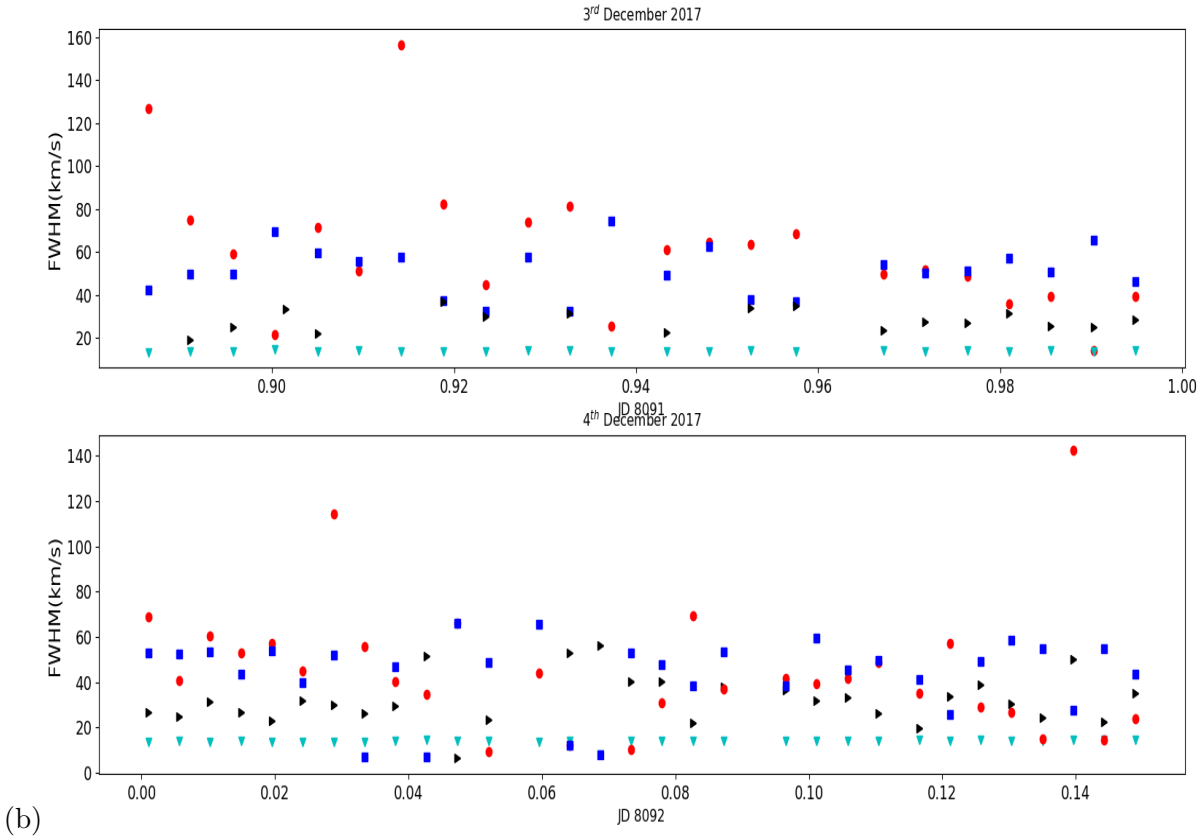

(b)

Figure 5.5: Figures (a) and (b) show show the radial velocities and the FWHM of the different features plotted as a function of the Julian Dates for the night starting on the 3^{rd} of December 2017.

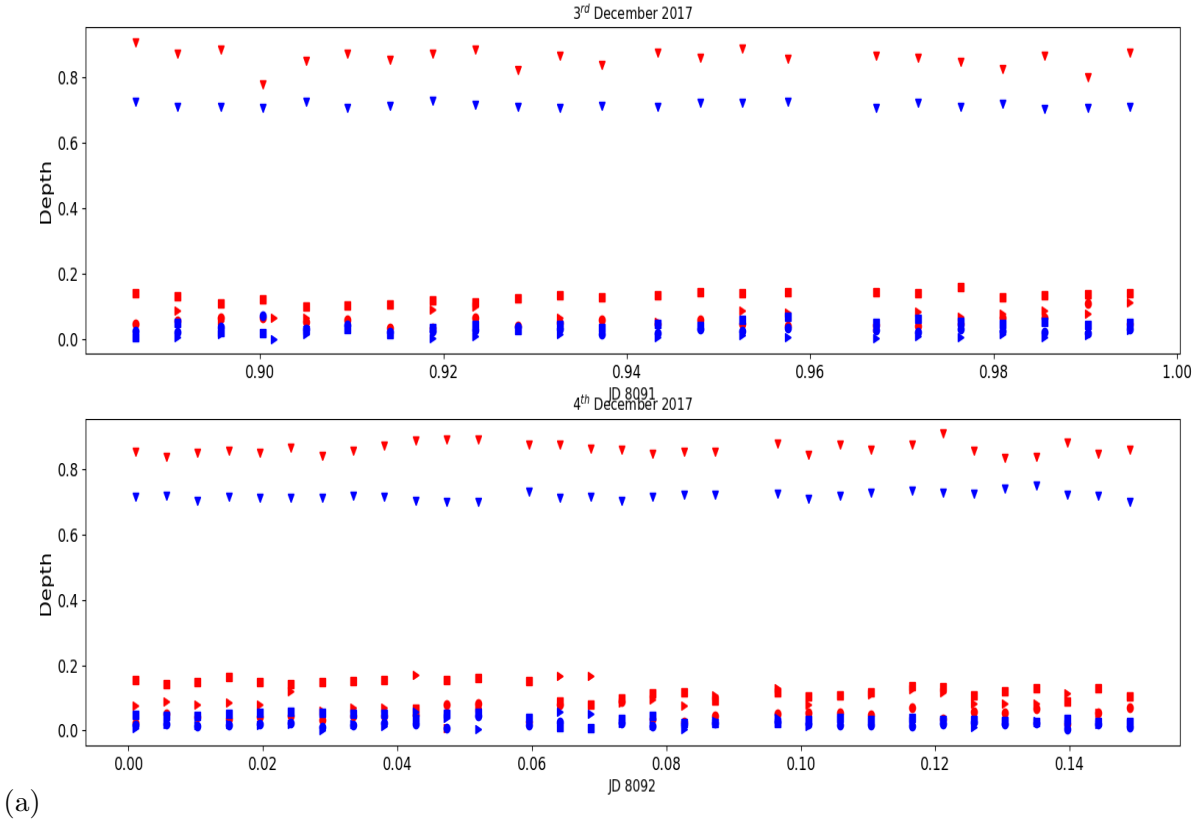

(a)

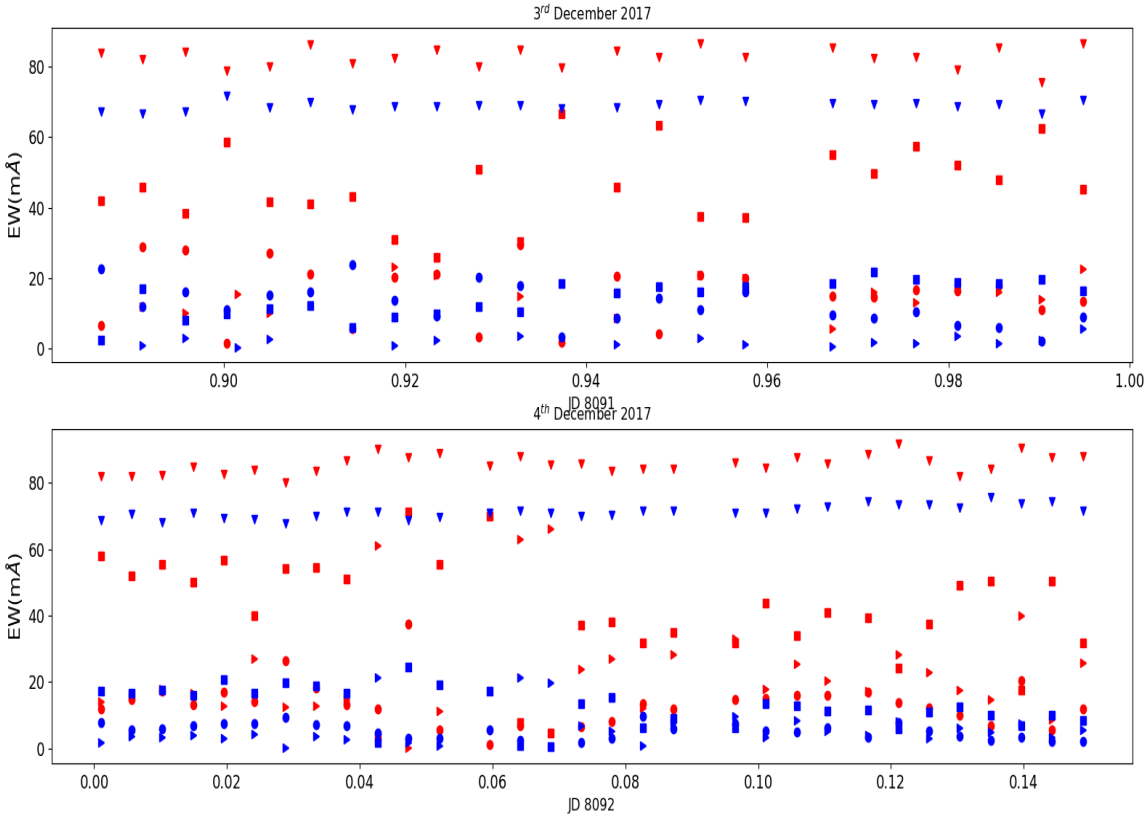

(b)

Figure 5.6: Figures (a) and (b) show show the H & K line depths and E.W. of the different features plotted as a function of the Julian Dates for the night starting on the 3^{rd} of December 2017. Absorptions in K and H lines are plotted in red and blue respectively.

5.3 Velocity features

The different fitted absorptions can be classified as follows in terms of the different velocity regimes:

- 23 blueshifted absorptions
- 48 circumstellar absorptions(at or close to the heliocentric radial velocity of the star)
- 13 red shifted absorptions at < 40 km s^{-1}
- 58 40 - 100 kms^{-1} absorptions
- 39 0 - 60 kms^{-1} absorptions
- 45 $>$ 60 kms^{-1} absorptions
- 13 $>$ 100 kms^{-1} absorptions
- 2 $>$ 200 kms^{-1} absorptions

As stated in Section 3.2.4, the absorptions in both the H & K lines were fitted with Gaussians simultaneously and hence, the velocities at peak depth of the different H & K line absorptions were equal to each other. This was considered a reasonable approximation due to similar studies conducted by previous authors(Persson et al.(1998) [4],Petterson et al.(1999) [3]) which found that the radial velocities at central depth of the different absorptions in the H & K lines generally agree with each other strongly as was discussed briefly in the Section 1.4. As shown in the Figures 5.1(a) and 5.3(a), the different features with radial velocities at peak depth lying relatively close to each other were plotted using the same symbol and hence as a result, do not show much variation between the nights. Blue-shifted features were observed on various nights, specifically on successive nights from 7^{th} of April 2017 to 10^{th} April 2017 (J7851 to J7854), 5^{th} June 2017 to 6^{th} June 2017 (J7910 to J7911) and 4^{th} December 2017 to 7^{th} December 2017 (J8092 to J8095). On the first set of nights, a low-velocity blue-shifted feature centred at a velocity of around -7 kms^{-1} is observed from the 7^{th} of April to the 8^{th} of April which is not present on successive nights, while blue-shifted features centred at velocities of

around -40 km s^{-1} and -70 km s^{-1} are present on subsequent nights in the set. There is also a blue-shifted feature observed only on the 9^{th} of April 2017 which is not present on any other nights in the set. Similarly, the blue-shifted features present from the 5^{th} of June to 6^{th} June (J7910 to J7911) and from the 4^{th} December to 7^{th} December (J8092 to J8095) are centred at velocities of around -5 km s^{-1} and -40 km s^{-1}. The broad blue-shifted features identified are present almost exclusively in cases where there is also a HVF present. This supports the conclusions derived by Beust et al.(1990) [1] who theorised that broad blue-shifted features are produced when the FEB lies at a distance within $\approx 10R_{star}$ from the host star and are the result of Ca II ions being repelled away from the star due to radiation pressure while the infalling head of the FEB produces the HVF. With the exception of a few blue-shifted features on these nights, most of the blue-shifted features on these nights are classified as 'poorer single' or 'poorer blend' and are much more prominent in the K line than in the H line which leads to open questions regarding their credibility. The average value found for the velocity of the circumstellar feature was $21.33^{+0.82}_{-0.82}$ kms^{-1} which lies within the uncertainty range of the radial velocity of β Pic of $20^{+0.7}_{-0.7}$ as estimated by Gontcharov et al.(2006) [31].

Specific LVFs with a velocity just higher or lower than the stellar radial velocity were observed on various nights which were blended strongly with the circumstellar feature resulting in an assymetrical broadening of the circumstellar feature. These are the features with the highest depth among all absorptions resulting from transiting exocomets. From the 7^{th} of April to 10^{th} of April 2017 (J7851 to J7854) and from the 13^{th} July to 14^{th} July 2017 (J7948 to J7949), a feature blended with the circumstellar feature is observed which has a velocity higher than the velocity of the circumstellar feature while a similar feature is observed from the 3^{rd} of July to the 4^{th} of July 2017 (J7938 to J7939) which instead has a lower velocity with respect to the circumstellar feature. Although there were no observations taken following the set of successive nights which had the LVF responsible for broadening the circumstellar feature, the presence of the LVF on successive nights shows the relatively long lifetime of this feature (of the order of days).

Various HVFs have also been observed with a total of 71 features with velocities greater than 40 kms^{-1}. As the lifetime of these features are usually $\approx$ 4 hours or on the order of hours [1], to ascertain whether the HVFs observed on the successive nights with

radial velocities relatively close to each other are the result of a stream of exocomets passing our line of sight on different nights requires more investigation by observation of their FWHM. There are two features present at a radial velocity of > 200 kms^{-1} which occur on the nights of 6^{th} December 2017 and 9^{th} December 2017. However, both of these features are classified as 'poorer single' due to the Gaussians being poor fits to these absorptions, and hence, the credibility of the radial velocity at peak depth of these features is questionable.

The variability of the radial velocities of the different features on the night starting on the 3^{rd} of December 2017(JD2458092) is shown by the Figure 5.5(a). As is shown on the figure, there is a presence of two HVFs with a velocity >60 kms^{-1} for the vast majority of the night (except for cases where a lower number of Gaussians was used to fit the normalised profile due to a very low signal to noise ratio), the circumstellar feature (at or close to the stellar radial velocity) and a blueshifted feature. One of the HVFs lies close to a velocity of 60 kms^{-1} and the other HVF lies at a velocity of around 100 kms^{-1} for the vast majority of the night. Although it was attempted to fit most of the individual spectra with the same number of Gaussians (using the same initial parameters used for the median spectrum), the fact that the python *curve_fit trf* procedure was still able to fit almost all spectra with the same number of Gaussians, albeit with varying parameters, means that there is atleast some confidence that the features existed throughout the course of the night and were real. The length of the observational night was about 6 hours so the fact that these features were present throughout the course of the night and didnot show much variation in radial velocity was not too surprising as the HVFs usually have a lifetime on the order of hours. Also, the presence of the blueshifted feature can be attributed to the presence of a HVF which also fits well within the FEB model developed by Beust et al.(1990) [1]. The predominance of blended features, most of which are redshifted and can be present on successive nights, lends credence to the scenario discussed in Lagrange-Henri et al.(1996) [2] which states that an additional comet, not necessarily with the same periastron, also enters our line of sight before the remnant tail of the previous comet has been dispersed and also supports their conclusions as to the clumpy nature of the gas.

5.4 FWHM of variable features

The variability of the FWHM of the different absorption features across 2017 can be examined by looking at Figures 5.1(b) and 5.3(b). As is visible from the figures, with the exception of the circumstellar feature and some other features, the different absorption features with relatively close radial velocities generally show a variation in FWHM between nights. The average computed value for the FWHM of the circumstellar feature was found to be $13.30^{+1.52}_{-1.52}$ kms^{-1} with a variance of 2.31 which showed that the FWHM of the circumtellar feature didnot show a significant variation among the analysed spectra of 2017.

As the FWHM of an absorption line is inversely proportional to the distance of the exocomet from the host star [2], a general variation in FWHM of the different features between nights suggests that the features are the result of exocomets transiting at a range of distances from the host star. The FWHM of the LVFs which occur on successive nights and are responsible for broadening the circumstellar feature as discussed in the Section 5.3, do not show any discernible variation between nights which supports the hypothesis that these features are likely the result of a stream of exocomets transiting the star at the same periastron between the successive set of nights. Other features which do not show any significant variation in the FWHM between the nights are also observed on nights such as the LVF observed on the nights 8^{th} May 2017 (J7882) and 12^{th} May 2017 (J7886)(represented by the green + symbol) and also the LVF observed on the consecutive nights from 8^{th} of July 2017(J7943) to 9^{th} of July 2017(J7944) (represented by the red Y symbol). There are also HVFs which have similar values for the FWHM which appear on widely separated nights such as the one which appears on the 28^{th} of July 2017(J7963) and the 29^{th} of September 2017 (J8026) (represented by the blue solid square). There is also a HVF which has a velocity just greater than 40 kms^{-1} which appears on consecutive nights on the 5^{th} of December 2017(J8093) to the 6^{th} of December 2017 (J8094). On these and other such nights as well, it is likely that these features are produced as a result of exocomets transiting at periastrons very close to each other.

The variability of the FWHM of the different features on the specific night chosen for analysis on an observation by observation basis which started on the 3^{rd} of December

2017 is shown by the Figure 5.5(b). As shown by the figure, the FWHM of the different features (with the exception of the circumstellar feature) show a variation throughout the course of night. This is however not as expected as the FWHM of the same feature should remain roughly constant throughout the course of the night due the fact that the FWHM allows information to be derived regarding the orbital characteristics of the exocomet and as a single exocomet takes a duration of ≈ 4 hours to transit in front of the star, the FWHM should remain roughly constant atleast for the majority of the night due to the constant periastron of the exocomet. However, previous authors such as Petterson et al.(1999) [3] , Persson et al.(1998) [4] and Barnes et al.(2000) [7] also observed a variation in FWHM of specific features throughout the night (as shown by Figure 1.17(a) by Petterson et al.), however this is dependent on the quality of the performed fits. Similarly, the obtained variation in the FWHM of the different features throughout the course of the night can be explained by the fact that each of the individual spectra have a low signal to noise ratio as compared to the median spectrum and as a result, the fitted Gaussians are generally poor fits to the identified absorptions, leading to questions regarding their credibility. Figure 5.7 shows the FWHM for the various absorptions across 2017 plotted against the heliocentric radial velocity.

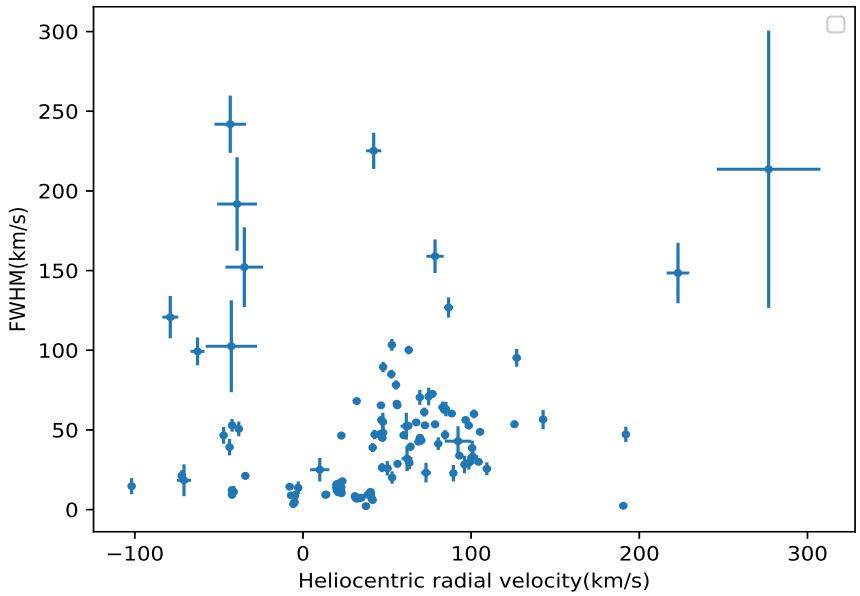

(a)

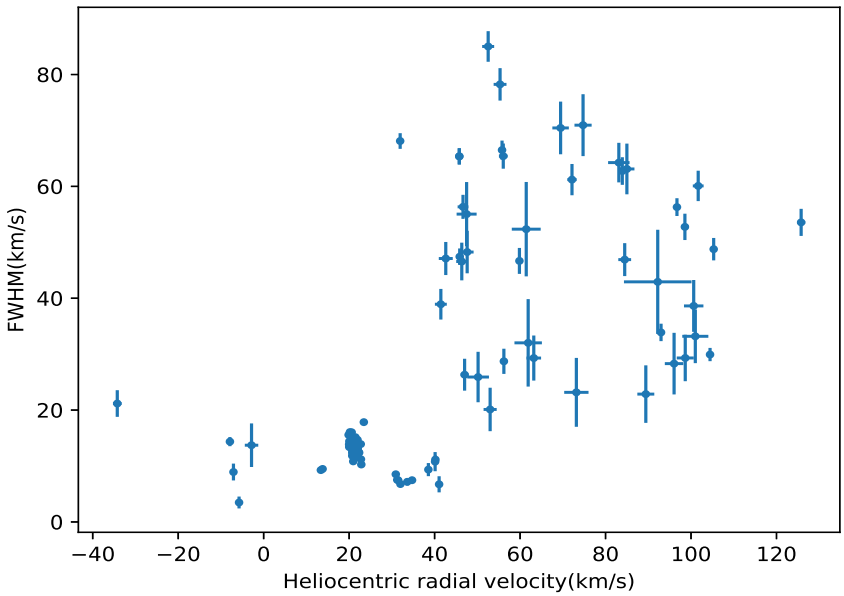

(b)

Figure 5.7: Figures (a) and (b) show the FWHM of the features as a function of radial velocity. Figure (a) plots the FWHM against radial velocity for all absorptions and Figure (b) plots only those absorptions classified as 'gS' or 'gB' respectively.

Figure 5.7 reinforce findings of other authors such as Lagrange-Henri et al. (1996) [2] and Petterson et al. (1999) [3] as shown by Figure 1.16. Although the correlation between the velocity and the FWHM seems to be weak, the following conclusions can be derived :

- Features of any widths can be found at all radial velocities.
- Features with lower relative velocities generally tend to have lower widths.
- Features with higher relative velocities generally tend to have higher widths.

Based on the FEB model developed by Beust et al.([1,49,85]), the HVFs transit the star at lower distances ($< 10R_\star$), while the LVFs transit the star at higher distances ($10R_\star \leq d \leq 30R_\star$). As the FWHM of an absorption is expected to decrease as the distance between the exocomet and the host star increases [2], a generally higher FWHM of the features at high relative velocities compared to the features at low relative velocities supports the hypothesis that exocomets transiting at lower distances are responsible for the production of the features at higher relative velocities. Figure 5.8 shows the FWHM of all features plotted against the central depths of the different absorptions in Ca II H & K lines.

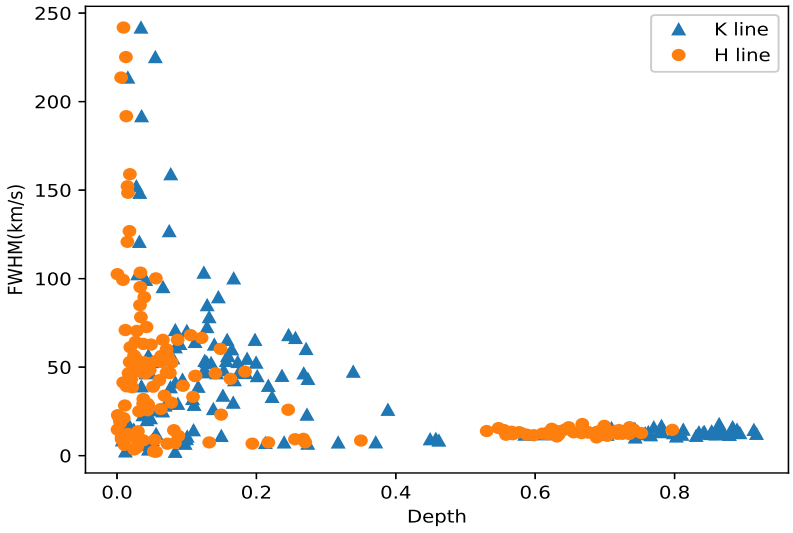

Figure 5.8: FWHM plotted against the Ca II H & K line depths for all features

Figure 5.8 leads to the following observations:

- The deepest features are always narrow features.
- The shallow features may be of any FWHM.
- The broadest features are limited to only the shallow absorptions.

Based on the above trends, it can be implied that the ionic clouds responsible for the deepest features (resulting in high value for the filling factor, α) are also the ones which transit the star at large distances. Also, as the shallow features can be found at any FWHM, this implies that the clouds that occult a small proportion of the stellar disk (lower values for α) can be found at a range of distances from the host star.

5.5 Depth of variable features

The variability of the depths of the different features across 2017 are shown by the Figures 5.2(a) and 5.4(a). In these figures, the depth of the circumstellar feature (represented by solid circles) show an approximate cyclical variation throughout the year i.e. the depth of the circumstellar feature increases and decreases throughout the course of 2017. This is in contrast to its FWHM which does not show much variation throughout the year. It is also visible that the LVF which is blended strongly with the circumstellar feature on the successive nights from the 7^{th} of April 2017 to the 10^{th} of April 2017 (J7851 to J7854) and represented by an upside down triangle, has a depth only below the circumstellar feature and this depth decreases over time in both the H & K lines. Similarly, the LVFs observed on the 3^{rd} of July to the 4^{th} of July 2017 (J7938 to J7939)(represented by blue and red stars) and the 13^{th} of July 2017 to the 14^{th} of July 2017(J7948 to J7949)(represented by an upside down triangle) which also result in a broadening of the circumstellar feature, do not show any significant variation in the depths in both the H & K lines. The average fitted values for the depth of the circumstellar feature in the H & K lines were $0.80^{+0.08}_{-0.08}$ and $0.660^{+0.063}_{-0.063}$ respectively. The uncertainties on these values were estimated using the standard deviation of all the obtained values, so the variances of the obtained values for the depth of the circumstellar feature in the H & K lines were 0.0040 and 0.0064 respectively which shows that the values for the depth of the circumstellar feature in

the H & K lines didnot show much variation across 2017. As the depth in the H & K lines is directly proportional to the filling factor, α (See Equation 1.6), a variation in the depths in the H & K lines between different nights suggested a variation in the degree of stellar disk obscuration by the ionic clouds associated with the exocomets responsible for causing the features, while a general lack of variation between some features suggested that the ionic clouds on these nights occulted a similar proportion of the stellar disk during the transit. The variability of the depths of the different features observed across the specific night chosen for analysis on an observation by observation basis is shown by the Figure 5.6(a). As shown by the figure, the depths of the different features do not show much variation across the course of the night. This is analogous to the change in depths across different nights as shown by Figure 1.17(a) which also shows that the depths across the course of the night doesnot show much variation. Figures 5.9 to 5.11 show the depth of the variable features plotted as a function of the radial velocity at peak depth.

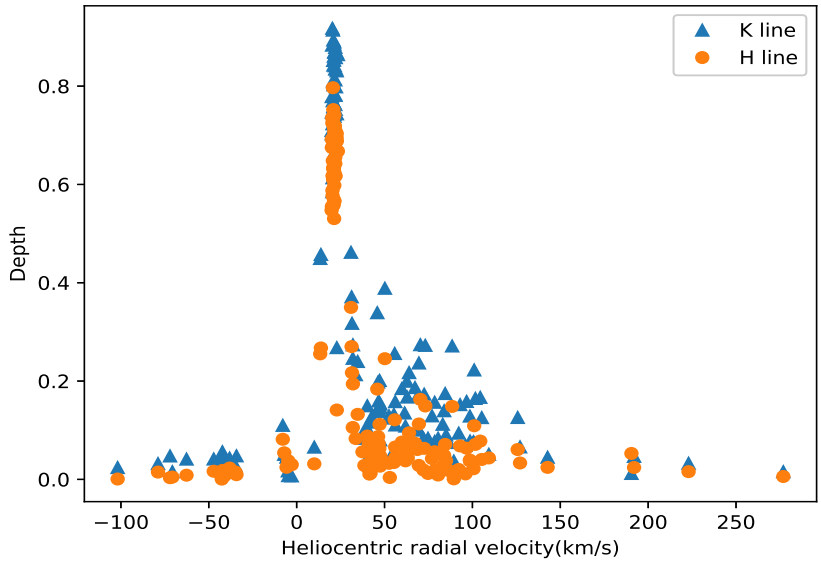

Figure 5.9: *Figure showing the depths of Ca II H & K absorption features plotted against the radial velocity for both the H & K lines.*

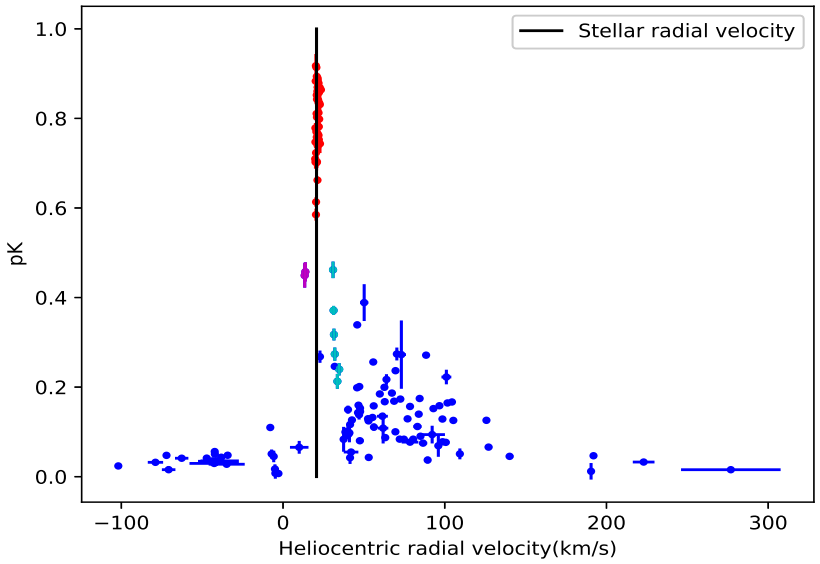

(a)

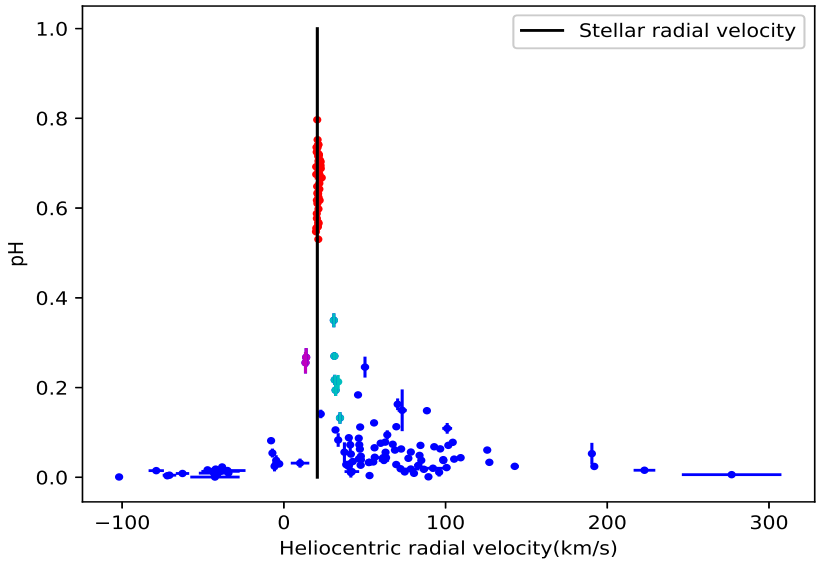

(b)

Figure 5.10: Figures (a) and (b) show the H & K line absorption feature depths plotted as a function of radial velocity. The points plotted in red represent the circumstellar absorptions while the points plotted in magenta and cyan represent the deep LVFs resulting in a broadening of the circumstellar absorption. The stellar radial velocity is indicated by a vertical line.

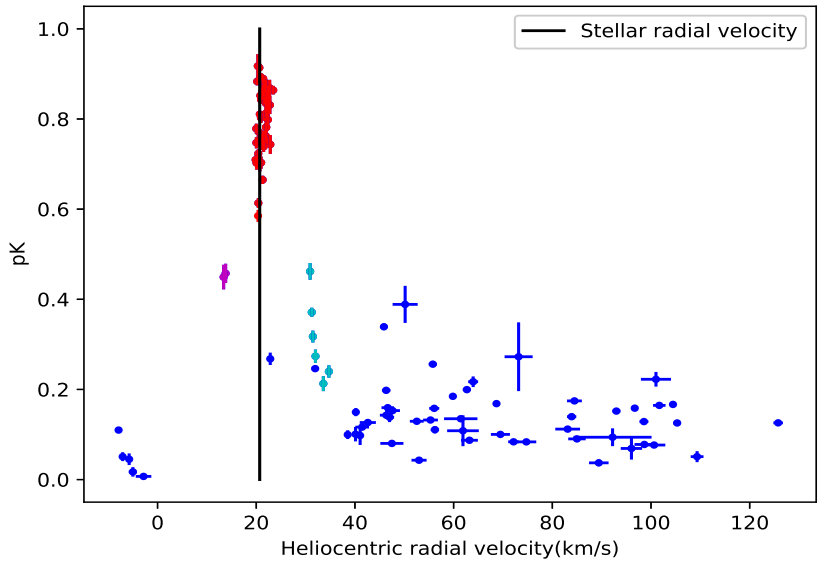

(a)

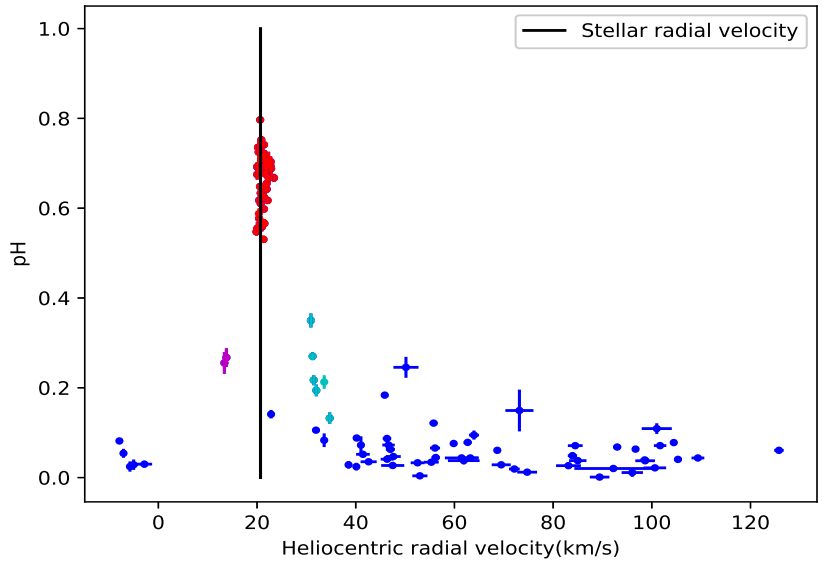

(b)

Figure 5.11: Figures (a) and (b) show the H & K line depths plotted as a function of radial velocity only for absorptions classified as 'gS' or 'gB'.

Figures 5.9 to 5.11 allow the following conclusions to be derived regarding the nature of the peak depth of the absorptions as a function of the radial velocity:

- The deep features are found at low radial velocities.
- Shallow features may be found at any radial velocity.
- Features with lower positive radial velocities($<100\text{kms}^{-1}$) can be shallow or deep features.
- Features with higher positive radial velocities(> 100 kms^{-1}) are limited to shallow depths.

To obtain α, the fraction of the stellar disk being occulted by an ionic cloud associated with an infalling comet, the peak depths of the absorptions in the H & K line must be plotted against each other to obtain graphical solutions for the filling factor, α. Figures 5.12 and 5.13 show such a plot with the iso-α curves overlayed on the plotted points.

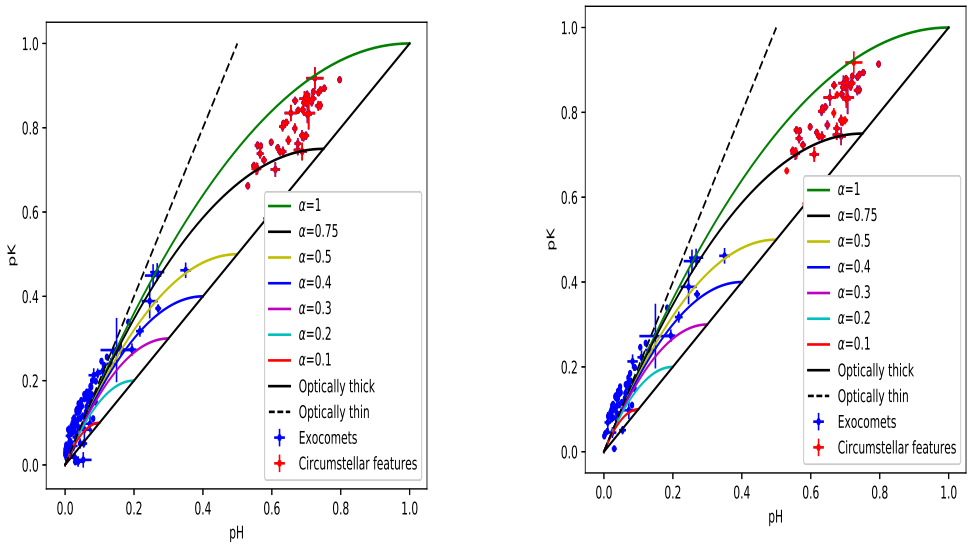

(a) Plot for all absorptions.

(b) Plot for only those absorptions classified as 'gS' or 'gB'.

Figure 5.12: Figures showing the central depth of the H & K line absorptions plotted against each other for all absorptions (including the circumstellar and blue-shifted absorptions).

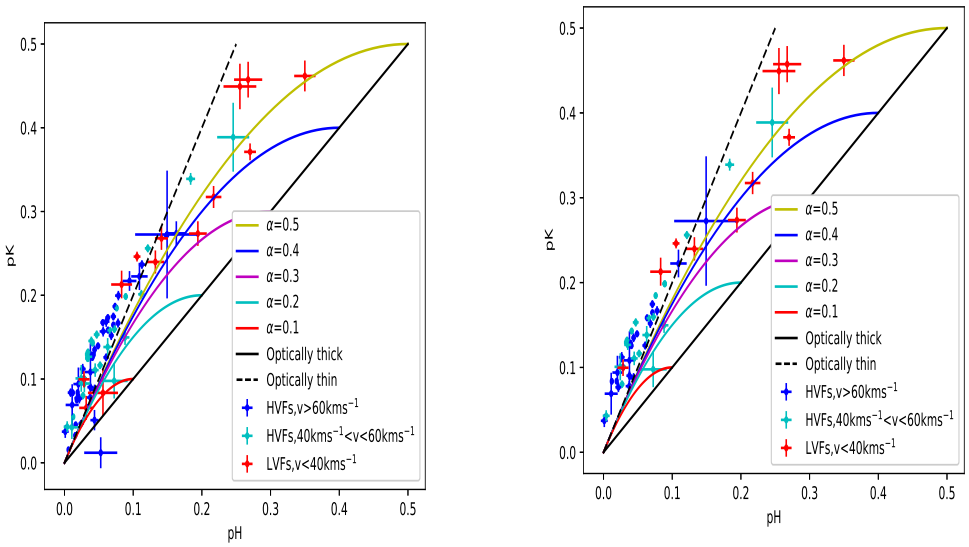

(a) Plot for all red-shifted absorptions.

(b) Plot for only those absorptions classified as 'gS' or 'gB'.

Figure 5.13: Figures showing the central depth of the H & K line absorptions plotted against each other for only red-shifted absorptions resulting from exocometary transits.

In Figure 5.12, which shows the plots for the absorption depth plotted for all absorptions, it is visible that for a small number of nights, the peak depth in the H line is greater than that for the K line. This effect was proposed by Beust & Lissauer(1994) [14] as being a differential effect of the stellar rotation away from us. However, in this case, the specific absorptions responsible for these points were all classified as either 'poorer single' or 'poorer blended' and hence, the credibility of the phenomenon is questionable in this case.

In Figure 5.13, only absorptions due to transiting exocomets are plotted and the absorptions with radial velocities in the velocity regimes (v<40 kms^{-1}, 40kms^{-1} < v<60kms^{-1}, v>60 kms^{-1}) are plotted in different colours. This was done to compare with the findings of Petterson et al.(1996) [5] and Persson et al.(1998) [4] who used a cut-off value of 60 kms^{-1} to divide the LVFs and HVFs in their MSc. thesis. Based on the above plots, the following conclusions can be derived:

- Most of the absorptions lie close to the optically thin limit (on either side of the optically thin line but mostly beyond the optically thin limit), in the region where the iso-α lines are very close to each other. This means that it is hard to distinguish between weak lines resulting from a cloud which covers a large part of the stellar disk (large value for α) from weak lines resulting from a cloud which covers a small part of the stellar disk (small value for α). This supports the hypothesis as discussed briefly in the Section 1.2.2 that it is only possible to get a lower limit on the value of α for weak/unsaturated lines.

- HVFs(v>60 kms^{-1})(plotted in dark blue) with the exception of one outlier are restricted mainly to lower depths and have a lower range of filling factors.

- HVFs in the velocity regime 40 kms^{-1} - 60 kms^{-1}, (plotted in cyan in Figures 5.13) are found at a range of depths but have a depth just below the LVFs. The iso-α line of 0.5 passes close to two of these points which suggests that these absorptions can also have large values for the filling factor. It is also visible in Figure 5.12, that the iso-α line for 1 passes through one of these points which suggests that this point likely has a very large filling factor(close to 1).

- LVFs (defined as having v < 40 kms^{-1}) which are plotted in red in Figures (a) and (b) can be found at any depth. The deepest features are also LVFs and can also have very high filling factors(very close to 1).

Using Equations 1.9 and 1.6, the values for the absorption depths (τ) and the filling factor (α) were calculated for any given combination of depths in the H & K lines (p_K and p_H). Then the log of the absorption depths were plotted against the filling factor to result in the plots as shown in Figures 5.14 and 5.15.

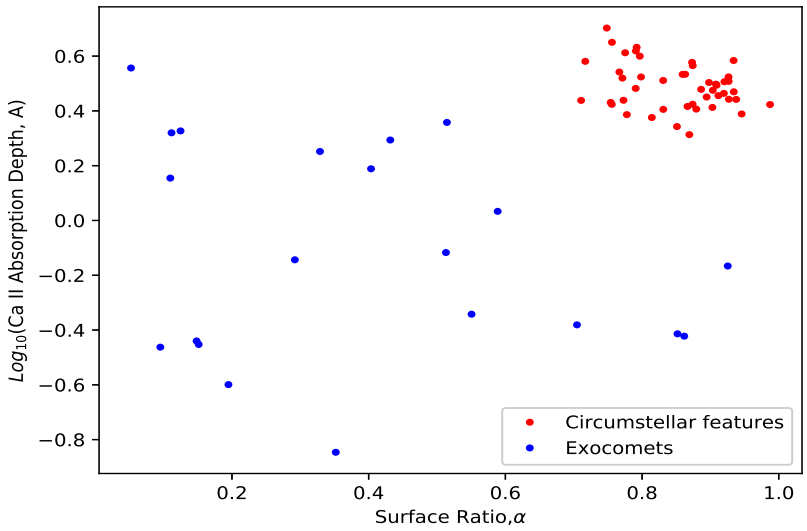

(a)

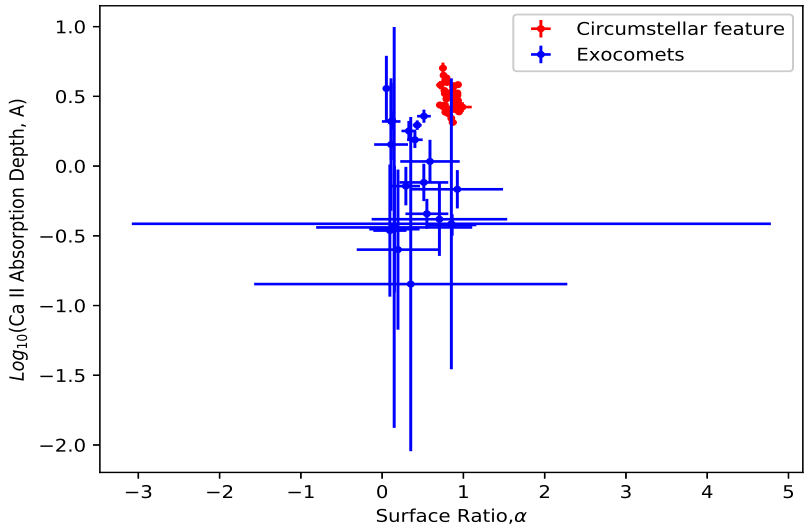

(b)

Figure 5.14: Figures showing the log of the absorption depths,A, plotted against the filling factor, α, for all absorptions with α between 0 and 1. Figures (a) and (b) show the plot without and with errorbars respectively.

To test the two family hypothesis for the exocomets around β Pic as derived by Kiefer et al.(2014) [6], the log of the absorption depth was plotted against the filling factor,α, for the absorptions only due to the transiting exocomets, to observe any clustering based

on the two velocity regimes, v< 40kms^{-1} and v > 40kms^{-1} and the two depth regimes, $p_K > 0.4$ and $p_K < 0.4$, which correspond to the regimes where the two different families of exocomets were concentrated.

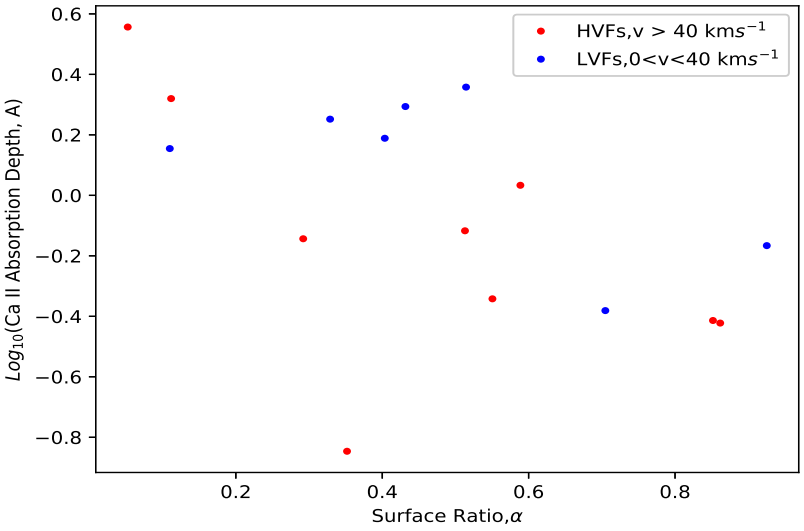

(a)

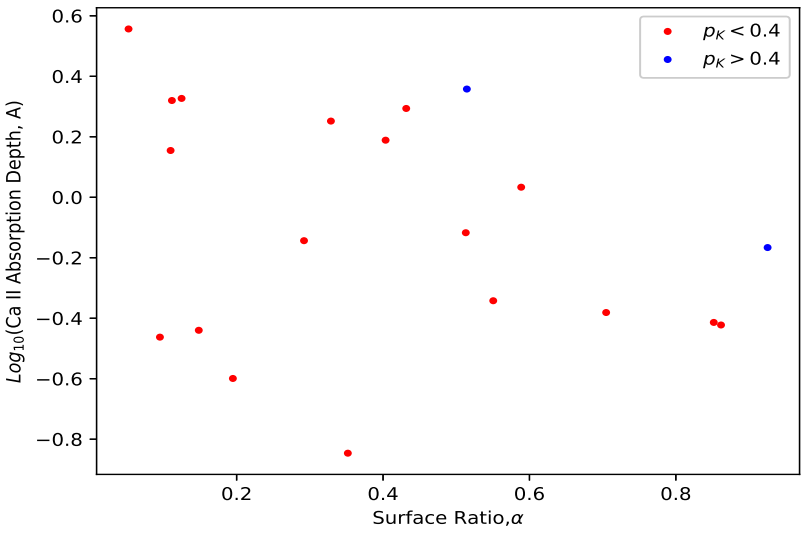

(b)

Figure 5.15: Figures showing the logarithm to the base 10 of the absorption depths, A, plotted against the filling factor, α, for all absorptions due to transiting exocomets with α between 0 and 1.

Figure 5.15(a) shows that no discernible clustering of the points is visible based on the two velocity regimes (0< v< 40 kms^{-1} ; LVF and v > 40 km s^{-1}; HVF) which correspond to the velocity regimes where the two distinct families of exocomets mainly cluster around based on the distribution of radial velocities as shown by Figure 1.18(b). Similarly, no significant clustering of points is seen in Figure 5.15(b) based on the two depth regimes ($p_K > 0.4$ and $p_K < 0.4$). However, Figures 5.14 and 5.15 only considered absorptions with α values which lie between 0 and 1 and this led to the exclusion of multiple absorptions whose computed values for α were found to be either -ve or greater than 1. This was due to the nature of Equation 1.6 which states the expression for α used. As stated in the equation, the expression for α is a fraction which has a denominator $(2\times p_H - p_K)$ which plays a vital role in the exclusion of the majority of absorptions for the plots shown in Figures 5.14 and 5.15. As is visible on Figures 5.12 and 5.13, many absorptions lie beyond the optically thin limit which implied that for these absorptions $2\times p_H$ is less than the value for p_K. Also, for some absorptions, the value for the quantity $2\times p_H$ is only slightly larger than that for p_K resulting in an extremely small value for the denominator, $(2\times p_H) - p_K$, which resulted in a very large value for α, greater than 1. As such values for α are unphysical, they were excluded from the plot and hence, due to the very small amount of data available on the plots as shown by Figure 5.15, no reasonable evidence of clustering of points based on the two distinct families of exocomets as shown on the plot in Figure 1.19 by Kiefer et al.(2014) [6] was found in this case. However, by plotting the filling factor as a function of radial velocity, information can be derived about the degree of the stellar disk obscuration by the ionic clouds which result in the production of the HVFs and the LVFs.

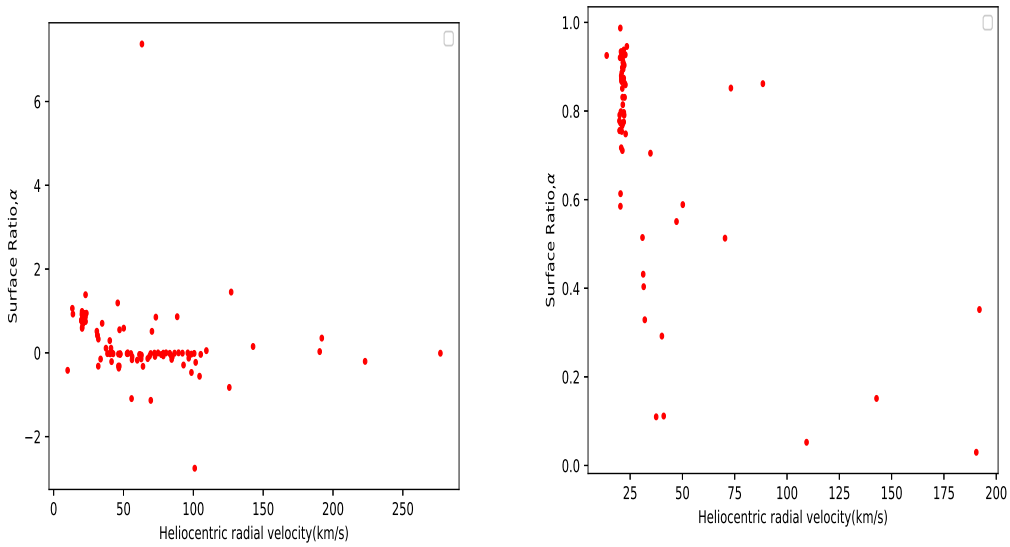

(a) Plot for all red-shifted absorptions

(b) Plot for only those absorptions with values of α between 0 and 1.

Figure 5.16: Figures showing the value of α plotted against radial velocity at central depth for the different absorptions.

As shown in Figure 5.16(b), a general trend of decrease in the value of the filling factor is observed with an increase in red shift velocity. This further supports the hypothesis that the higher velocity features are produced as a result of the ionic clouds associated with the transiting exocomets that occult a smaller fraction of the stellar disk as compared to those producing the lower velocity features.

5.6 Equivalent widths of variable features

The variability of the equivalent widths for the absorptions across 2017 is visible on the Figures 5.2(b) and 5.4(b). As shown by the figures, the E.W. of the circumstellar feature didnot show much variation for the vast majority of 2017. The E.W. of the other features identified as having radial velocities relatively close to each other, generally show a variation in E.W. between nights (with the exception of some features) which shows a corresponding change in the strength of the absorptions between nights. The variability of the E.Ws on the 3^{rd} December 2019 is shown in Figure 5.6(b). With the exception of

the circumstellar feature, the E.W. of the other absorptions showed a general variation throughout the course of the night which can be attributed to the changes in the fitted values of the FWHM and the depth of the different features. Also, a key observation from these figures is that the E.W. of the absorptions in the K line (plotted in red) is in almost all cases higher than the E.W. in the H line (plotted in blue). This is to be expected due to the oscillator strength of the K line being almost twice as that of the H line.

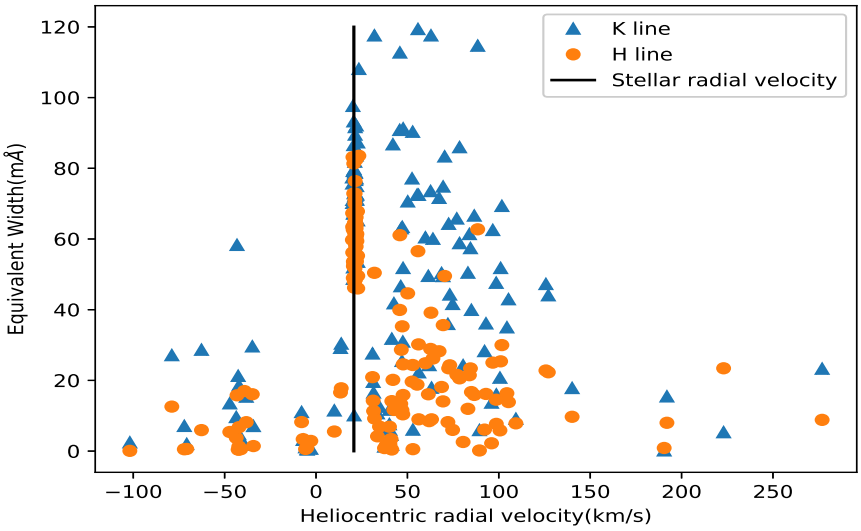

Figure 5.17: *Figure showing the EWs of Ca II H & K lines plotted against the radial velocity. The cluster of points beyond an E.W. of 40 mÅ around the line denoting the β Pic radial velocity denote the circumstellar features.*

The following conclusions can be derived from the Figure 5.17:

- Features with lower positive radial velocities(< 100 kms^{-1}) can be found at a range of E.Ws.
- Features with higher positive radial velocities(> 100 kms^{-1}) are restricted to lower E.Ws.
- The max E.W. at any radial velocity show an overall decrease with an increase in radial velocity..

As the E.W. of an absorption feature was computed using the Equation 3.7, it is a combination of the FWHM and the peak depth of an absorption feature. As was discussed briefly in the section 5.4, Figure 5.7 showed that although the correlation between FWHM and radial velocity was found to be weak, features with higher radial velocities generally tended to have a higher FWHM as compared to the features with lower radial velocities. For the depths of the features (Figure 5.9), that while features with low positive radial velocities (< 100 kms^{-1}) can be shallow or deep features, higher velocity features were limited to shallow depths. It was also observed by Figure 5.9 that the max depth at any radial velocity shows a decrease with an increase in radial velocity. Hence, the overall decrease in E.W. observed in Figure 5.17 with an increase in radial velocity can be explained by the stronger decrease in depth with radial velocity when compared to an increase in FWHM with radial velocity.

CHAPTER 6

Discussion

This thesis contains an analysis of observations of β Pic taken across 2017 at the University of Canterbury Mount John Observatory(UC MJUO) using the HERCULES spectrograph and the Fairchild 486 back-illuminated CCD. The study focused on identifying and analysing variable absorptions in the Ca II H & K absorption lines across 2017 and mainly concerned the analysis of absorption features between nights. Spectra for one night starting on the 3^{rd} of December 2017 were analysed on an observation by observation basis to gain an insight into the short-term variability of the different features throughout the course of a night. The obtained results from this study can be compared with the results from similar studies conducted by other authors and put into the context of the FEB model as follows:

- Variable features with a range of radial velocities and FWHM were observed across 2017, lending support to the idead of a stream of bodies passing the line of sight at different periastrons and radial velocities, and the clumpy nature of the gas.

- Many blueshifted features were observed on various nights and also on various successive nights and most of these features were broad and present almost exclusively with a HVF(v> 40 km^{-1}) which confirmed the conclusions of Beust et al.(1990) [1] regarding the source of these features. Beust et al.(1990) suggested that blueshifted features are produced at distances of the FEB of $\approx 10R_{\star}$, at distances when a corresponding HVF is produced by the infalling head of the FEB

while the Ca II ions in the ionic cloud are repelled away from the star due to radiation pressure to produce the broad blueshifted features.

- Specific LVFs in the velocity regime 0-40 kms^{-1} were observed on successive nights which were responsible for broadening the circumstellar feature and the presence of these features over successive nights confirmed the findings of Lagrange-Henri et al.(1996) [2],Petterson et al.(1999) [3],Persson et al.(1998) [4] and Barnes et al.(2000) [7] who also found various LVFs lasting over a number of days which supported the hypothesis that LVFs can have a variability timescale over the order of days. The LVFs are hypothesised to have a longer variability timescale as compared to the HVFs due to the fact that they are the result of exocomets with lower radial velocity and hence, lower orbital velocity, which increases the duration of the transit as compared to the HVFs. Also, detailed simulations presented in Beust et al.(1996) [85] showed that once the arrival frequency of the FEBs is large enough(> 8 per day), the probability that any given LVF lasts several days becomes high. Hence, the simultaneous arrival of multiple comets at the same periastron can be used to explain the lifetime of some LVFs (including the ones observed in this study) over the order of days.

- A total of 71 HVFs(v>40 kms^{-1}) were observed on the various nights across 2017. HVFs were also observed on the night of 3^{rd} December 2017. It was found that the HVFs observed on this night were present throughout the course of the night which is not too surprising considering the length of the night ($\approx$ 6 hours) as HVFs are expected to have a lifetime over the order of hours. Various HVFs were also observed on widely separated nights with FWHM very close to each other, suggesting that these were the results of exocomets transiting at periastrons very close to each other. There was also a single HVF observed from the 5^{th} of December 2017 to the 6^{th} of December 2017 which didnot show any significant variation in the FWHM between the nights and it is likely that this feature was produced as a result of exocomets with similar orbital characteristics [2]. However, according to the FEB model by Beust et al.(1989-91) [1, 49, 51], HVFs should only have a variability timescale of a few hours, hence, the FEB scenario doesnot well explain this feature.

- Although the correlation between the FWHM and the radial velocity was found to

be weak, a general increase in FWHM with an increase in radial velocity was found as shown by Figure 5.7. This was analagous to the findings of other authors such as Lagrange et al.(1996) [2], Petterson et al.(1999) [3] and Persson et al. [4] as shown in the Figure 1.16 who also found an increase in FWHM of the absorptions with an increase in radial velocity. Beust et al.(1990) [1] hypothesised that the distance from the host star should decrease with an increase in radial velocity and as the FWHM of an absorption line is expected to increase with a decrease in distance from the host star, this is consistent with the idea that HVFs are produced by exocomets transiting at lower periastrons from the star [2].

- Features at positive radial velocities lower than around 100 kms^{-1} were found at a decreasing range of depths while those at higher velocities were restricted to shallow depths (See Figure 5.9). This finding was analagous to that found by other authors (Petterson et al.(1999) [3],Persson et al.(1998) [4]) who also found a decrease in the range of depths with an increase in radial velocity. This also supported the FEB model by Beust et al. (1990) [1] whose simulated spectra also showed that features at low relative velocities were generally deeper and narrower as compared to features with high radial velocities.

- By plotting the depths in the H & K lines against each other (See Figure 5.12), it was found that the majority of absorptions were between the optically thin and thick limits and beyond the optically thin limit. It was found on the plot (see Figure 5.13 that features identified as LVFs(v<40 kms^{-1}) were found at a range of depths but were also the features with the highest depths. It was also found that HVFs lying beyond a velocity of 60 kms^{-1} were mainly restricted to lower depths and had a lower range of filling factors. This finding agreed with the results of Petterson et al.(1996) [5] and Persson et al.(1998) [4] as shown by their unpublished MSc. thesis, however, some HVFs lying in the velocity regime 40 kms^{-1}- 60 kms^{-1} were found to have high depths and filling factors, a result which doesnot agree with the published studies of Lagrange-Henri et al.(1996) [2] and Petterson et al.(1999) [3] who found all HVFs lying beyond 40 kms^{-1} restricted to low depths. Although some features were found to lie beyond the optically thick limit ($p_H > p_K$), the credibility of these features is questionable due to their classification as 'pS' or 'pB'. Hence, it cannot be concluded with certainty that

these features were a consequence of the differential effect of the stellar rotation away from us as was suggested by Beust & Lissauer(1994) [14].

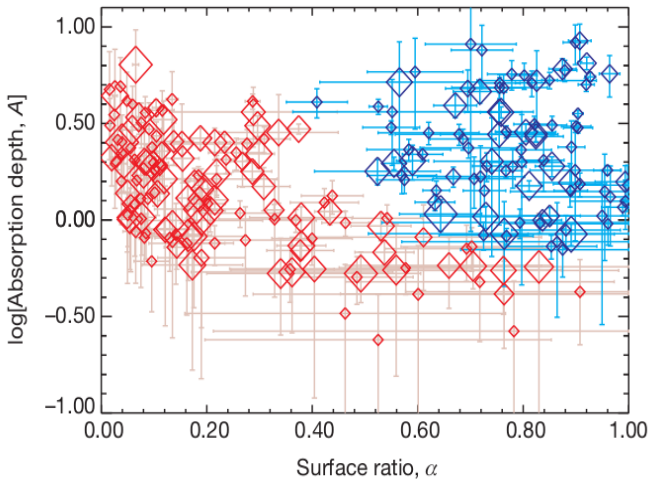

(a) Plot for Log of the absorption depth against the filling factor,α as obtained by Kiefer et al.(2014) for 252 detected exocomets with $\alpha < 1$. Points plotted in blue represent Population S,($p_K < 0.4$) and points plotted in red represent Population D (($p_K > 0.4$).Source: Kiefer et al. (2014) [6]

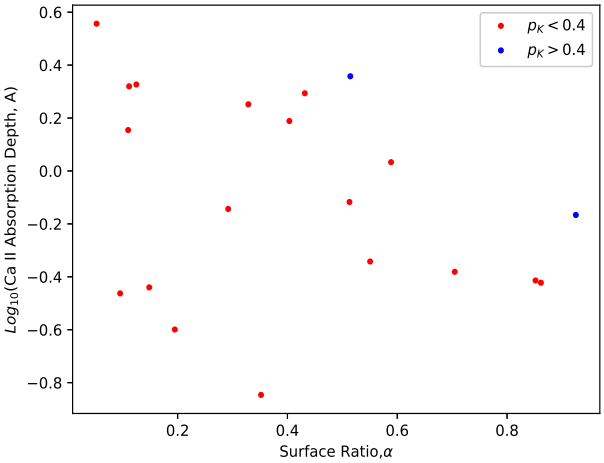

(b) Obtained plot for the log of the absorption depths against the filling factor, α, for those absorptions due to transiting exocomets obeying $0 < \alpha < 1$. Note the lack of sufficient amount of points which didnot allow to reinforce findings of Kiefer et al.(2014) regarding the two distinct populations of exocomets around β Pic.

Figure 6.1: A comparison of the plot obtained by Kiefer et al.(2014) of the log of the absorption depths against the filling factor,α, with the plot obtained as part of this study.

- By computing a value for the filling factor, α and the absorption depth, τ, for each combination of depths in the H & K lines, the log of the absorption depth was plotted against the filling factor to examine any clustering of points based on the two velocity regimes($0 < v < 40$ kms^{-1} and $v > 40$ kms^{-1}) and the two depth regimes ($p_K > 0.4$ and $p_K < 0.4$). These different regimes were chosen to compare with the plot obtained by Kiefer et al.(2014) [6] who found clustering of points in the plot based on the hypothesis that the transiting exocomets around β Pic can be divided into two distinct families with one of these families (termed as Population D) clustering at radial velocities below 40 kms^{-1} and having high depths ($p_K > 0.4$) while the other family (termed as Population S) although had a higher range of velocities, were in highest concentration at velocities greater than 40 kms^{-1} and had shallow depths($p_K < 0.4$). The obtained plot (Figure 5.15), however, didnot show any significant clustering of points based on the two velocity or depth regimes mainly due to the lack of a high quantity of absorptions with a value of α lying between 0 and 1.

It was predicted by Wang et al.(2016) that the Hill sphere of the gas giant planet β Pic b will transit β Pic from the start of April 2017 till the end of January 2018 [73], lasting a duration of approximately 300 days. As all observations in 2017 taken from the 6^{th} of April 2017 fall within this predicted duration of the transit, Ca II H & K absorption profiles from this period can be analysed to look for any effects of this predicted hill sphere transit. Simulations of moon formation within circumplanetary disks predict that in 80% of the time, gas giant planets will have four to six moons (Heller et al. (2014) [86]). Although these exomoons have not yet been detected , the possibility of their existence leads to the possibility that depending on their orbital parameters, they will transit β Pic during β Pic b's Hill sphere transit of β Pic . These moons could then, depending on the sizes of their Hill spheres, result in clearing out regions of the circumstellar disk via accretion of some circumstellar material, resulting in the introduction of gaps or density variations in the disk [87]. Even if the planet has no satellites which is unlikely, the transit of β Pic b's Hill sphere could still result in accretion of atleast some material towards β Pic b , which would lead to clearing out of some regions in the disk. As the circumstellar feature observed in all Ca II absorption profiles is the result of absorption of radiation by Ca II ions, with the singly ionized form of carbon (which is overabundant in the disk)

acting as the braking agent(Roberge et al.(2006) [88],Brandekar et al.(2011) [89]), an effect of clearing out of parts of the circumstellar disk could have an effect on the depth of the circumstellar feature in the Ca II H & K line profiles.

Another consequence of the Hill sphere transit could be an increase in perturbation of the orbits of the exocomets around β Pic which could result in either a significant increase or decrease in exocometary transits, leading to a significant increase or decrease in the number of identified absorptions in the Ca II H & K absorption lines within the duration of the Hill sphere transit as compared to the case when there is no Hill sphere transit. The average depth found in the K line for the circumstellar feature in the spectra collected between the 6^{th} of April 2017 and the 9^{th} of December 2017 (within the duration of the predicted transit) was $0.81^{+0.07}_{-0.07}$ with a variance of 0.0049 which shows that the depth of the circumstellar feature in the K line didnot show much variation within the duration of the predicted transit. The average value lies within the uncertainty range of the computed value for the average depth of the circumstellar feature in the K line ($0.68^{+0.08}_{-0.08}$) for the analysed nights which lie outside the duration of the predicted transit (from the 12^{th} of January 2017 to the 16^{th} of January 2017). The value also agrees with the values obtained by Barnes et al. (2000) [7] for data collected in 1998 when a β Pic b Hill sphere transit was not predicted by Wang et al.(2016). The values obtained for the depth of the circumstellar feature in the K line by Barnes et al.(2000) clustered around a value of 0.8 as can be seen in Figure 6.2 by the third panel from the top which shows the variation in the depth of the various features across the nights.

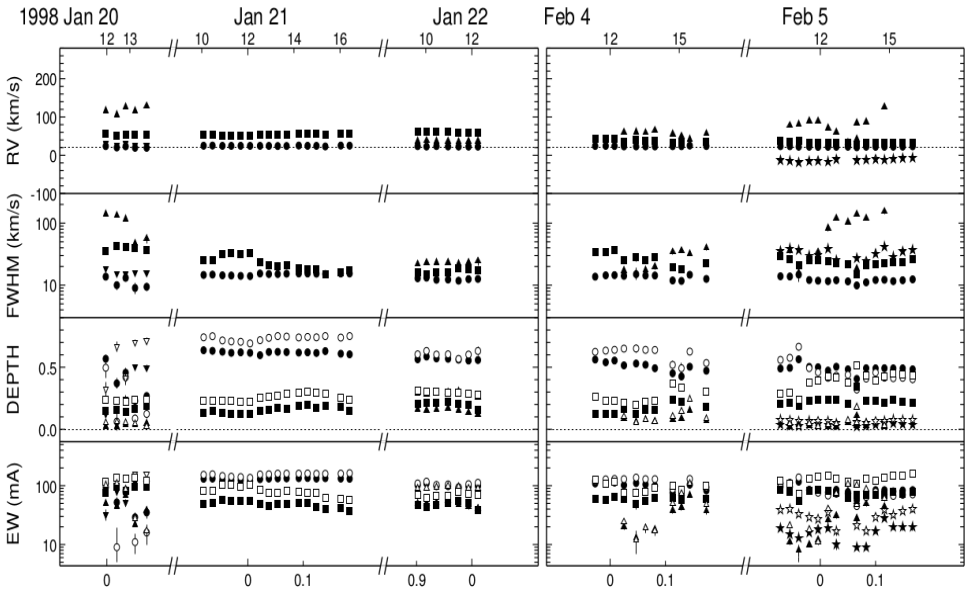

Figure 6.2: *Figure showing the variation of the obtained parameters for the different absorptions within and between different selected nights by Barnes et al.(2000) using data collected in 1998. Note the depth of the circumstellar feature in the K line as shown by the empty circles which cluster around a depth of 0.8.*

Hence, it can be concluded that no discernible significant variation in the depth of the circumstellar feature was seen during the supposed β Pic b Hill sphere transit in 2017. In regards to the frequency of observed events, the observed rate of exocometary transits in this study appears to be within the range of exocometary transits observed by other authors (Lagrange-Henri et al.(1996) [2],Barnes et al.(2000) [7] and Kiefer et al.(2014) [6]), who conducted studies using data collected when there was no prediction of a β Pic b Hill sphere transit and hence, no evidence could be derived of an unusually higher or lower perturbation of the exocomets due to the predicted β Pic b Hill sphere transit.

CHAPTER 7

Conclusion and Future Work

This thesis contains an analysis of absorption features identified in Ca II H & K absorption profiles obtained via observations taken of β Pic at the University of Canterbury Mount John Observatory (UC MJO) in 2017. This study mainly focuses on analysing the absorptions identified on nights across 2017 by analysing the median spectrum for a night. However, for the specific night of the 3^{rd} of December 2017, the complete set of spectra obtained on the night were fitted individually to gain an insight into the variability of the different features throughout the course of the night. Although the lifetime of the different features throughout the course of the different nights were not analysed for the purposes of this thesis (with the exception of one night), the predictions of the FEB model by Beust et al.(1990) [1] were found to be true in regards to the expected increase in the FWHM of the features with an increase in radial velocity and also the expected decrease in depths of the features with an increase in radial velocity. These results agreed well with similar studies carried out by previous authors such as Lagrange-Henri et al.(1996) [2] , Petterson et al.(1999) [3] and Persson et al. [4] as was discussed by these authors. Several LVFs(v <40 kms^{-1})responsible for assymetric broadening of the circumstellar feature were observed on successive nights which also supported the FEB model's prediction in regards to the high possible lifetime of the LVFs (over the order of days). While several HVFs(v> 40 kms^{-1}) were identified, only one HVF was identified on two consecutive nights(5^{th} December to 6^{th} December 2017) with sufficiently close radial velocities and FWHM. This feature could not be well explained by the FEB model as HVFs are expected to have a variability timescale over

the order of hours [51]. The HVFs identified on the specific night starting on the 3^{rd} of December 2017 were presumably present throughout the course of the night which also supported the FEB model's prediction that HVFs have a lifetime over the order of hours. By plotting the depths of the different absorption features in the H & K lines against each other, it was found that the majority of absorptions lied beyond the optically thin limit and between the optically thin and thick limits. It was found that the LVFs(v<40 kms^{-1}) had the highest depths of the different features and also could have very high filling factors (approaching unity). Some features in the velocity regime(40 kms^{-1} - 60 kms^{-1}) were also found to have high depths and filling factors with one of these features having a filling factor approaching 1. HVFs with velocities beyond 60 kms^{-1} were found to be restricted mainly to low depths which agreed with the findings of Petterson et al.(1996) [5] and Persson et al.(1998) [4] as shown in their unpublished MSc. Thesis but as some HVFs lying in the velocity range of 40 kms^{-1}-60 kms^{-1} were found to have high depths, this didnot agree with the published studies of Lagrange-Henri et al.(1996) [2] and Petterson et al.(1999) [3] who only found HVFs(v> 40 kms^{-1}) restricted to low depths. It was attempted to produce a plot of the log of the absorption depth against the surface ratio, α, as produced by Kiefer et al.(2014) [6] to confirm their findings in regards to the two family hypothesis of the exocomets around β Pic, however, due to the lack of a sufficient quantity of absorptions due to transiting exocomets with values of α lying between 0 and 1 , no major clustering of points could be observed in the plot based on the two depth regimes ($p_K < 0.4$ and $p_K > 0.4$) or the two velocity regimes (v<40 kms^{-1} and v > 40 kms^{-1}) which didnot allow reinforcement of the findings of Kiefer et al.(2014). Due to a predicted β Pic b Hill sphere transit event in 2017 starting from the start of April 2017 till January 2018, Ca II H & K absorption profiles collected in 2017 lying within this duration were analysed to look for any effects of a β Pic b Hill sphere transit. It was hypothesised that the Hill sphere transit could have an impact on the depth of the circumstellar feature or the frequency of exocometary transits due to accretion of circumstellar material or perturbations induced by the gravitational field of the body. However, no discernible variation could be observed on the depth of the circumstellar feature when compared to the study conducted by Barnes et al.(2000) [7] or on the frequency of exocometary transits when compared to the rate of exocometary transits as observed by other authors such as Lagrange-Henri et al.(1992) [2],Barnes et al.(2000) [7] and Kiefer et al.(2014) [6] who conducted their studies when a β Pic Hill

sphere transit was not predicted.

Future work on the study of β Pictoris, and other such possible protoplanetary systems, would be required to continue to improve our understanding of the processes involved in the formation of planets, and to lend clues as to how our own solar system may have been formed.

Future work at the University of Canterbury Mount John observatory could include:

- Continual monitoring of the Ca II H & K absorption profiles to further refine the Falling Evaporating Bodies(FEB) model and also to gain a greater insight into the variability timescales of the different features across the course of the night which was not a main focus of this thesis.
- Monitoring and analysis of the absorption profiles of other moderately ionized ions such as Mg II, Al III and Al II which have also been understood to be affected due to exocometary transits, to further understand and refine the FEB model.
- Improvement of the signal to noise ratio for the obtained spectra by increasing the exposure time of the different observations to around 30 minutes.
- Examining issues with the HERCULES spectrograph or the CCD detector that resulted in faulty spectra to be obtained for specific observational runs so that such errors don't occur in the future. The faulty spectra for the specific runs for the different orders led to their exclusion from the processing step which did not allow study of variable absorptions due to exocomets for several nights between different runs.
- Assuming the conclusions of Wang et al.(2016) are correct in regards to the orbital period and the Hill sphere transit of β Pic b, the next Hill sphere transit of β Pic b will occur sometime around September 2040 and last for a duration of around 300 days. Hence, a similar study could be performed using observations taken within this period in the future to look for any effects on the Ca II absorption profiles due to a β Pic b Hill sphere transit and compared with the results obtained in this study.

Bibliography

[1] H. Beust, A. Lagrange-Henri, A. V. Madjar, and R. Ferlet, "The beta pictoris circumstellar disk. x-numerical simulations of infalling evaporating bodies," *Astronomy and Astrophysics*, vol. 236, pp. 202–216, 1990.

[2] A.-M. Lagrange, F. Plazy, H. Beust, D. Mouillet, M. Deleuil, R. Ferlet, J. Spyromilio, A. Vidal-Madjar, W. Tobin, J. Hearnshaw, *et al.*, "The beta pictoris circumstellar disk. xxi. results from the december 1992 spectroscopic campaign.," *Astronomy and Astrophysics*, vol. 310, pp. 547–563, 1996.

[3] O. K. Petterson and W. Tobin, "β pictoris: the variable ca ii h & k absorptions from 1994 to 1996," *Monthly Notices of the Royal Astronomical Society*, vol. 304, no. 4, pp. 733–742, 1999.

[4] S. Persson, "Caii absorption in the circumstellar disk of beta pictoris and 51-opiuchi (unpublished msc. thesis)," 1998.

[5] O. K. Petterson, "Caii absorption in the circumstellar disk of beta pictoris and other a-type stars (unpublished msc. thesis)," 1996.

[6] F. Kiefer, A. L. des Etangs, J. Boissier, A. Vidal-Madjar, H. Beust, A.-M. Lagrange, G. Hébrard, and R. Ferlet, "Two families of exocomets in the β pictoris system," *Nature*, vol. 514, no. 7523, p. 462, 2014.

[7] S. Barnes, W. Tobin, and K. Pollard, "The variable ca ii absorption in β pictoris during 1998," *Publications of the Astronomical Society of Australia*, vol. 17, no. 3, pp. 241–243, 2000.

[8] F. Palla and S. W. Stahler, "The pre-main-sequence evolution of intermediate-mass stars," *The Astrophysical Journal*, vol. 418, p. 414, 1993.

[9] G. Schaller, D. Schaerer, G. Meynet, and A. Maeder, "New grids of stellar models from 0.8 to 120 solar masses at z= 0.020 and z= 0.001," *Astronomy and Astrophysics Supplement Series*, vol. 96, pp. 269–331, 1992.

[10] C. Burrows, J. Krist, K. Stapelfeldt, and W. I. D. Team, "Hst observations of the beta pictoris circumstellar disk," in *Bulletin of the American Astronomical Society*, vol. 27, p. 1329, 1995.

[11] D. A. Golimowski, D. R. Ardila, J. Krist, M. Clampin, H. C. Ford, G. D. Illingworth, F. Bartko, N. Benítez, J. Blakeslee, R. Bouwens, *et al.*, "Hubble space telescope acs multiband coronagraphic imaging of the debris disk around β pictoris," *The Astronomical Journal*, vol. 131, no. 6, p. 3109, 2006.

[12] A. L.H, "The atmospheres of the sun and the stars," *The atmospheres of the sun and the stars, by LH Aller. New York 2nd Edition,Ronald Press Company, 1963*, 1963.

[13] A. Lagrange-Henri, E. Gosset, H. Beust, R. Ferlet, and A. Vidal-Madjar, "The beta pictoris circumstellar disk. xiii-survey of the variable ca ii lines," *Astronomy and Astrophysics*, vol. 264, pp. 637–653, 1992.

[14] H. Beust and J. Lissauer, "The effects of stellar rotation on the absorption spectra of comets orbiting beta pictoris," *Astronomy and Astrophysics*, vol. 282, pp. 804–810, 1994.

[15] A.-M. Lagrange, D. Gratadour, G. Chauvin, T. Fusco, D. Ehrenreich, D. Mouillet, G. Rousset, D. Rouan, F. Allard, É. Gendron, *et al.*, "A probable giant planet imaged in the β pictoris disk-vlt/naco deep l'-band imaging," *Astronomy & Astrophysics*, vol. 493, no. 2, pp. L21–L25, 2009.

[16] F. Crifo, A. Vidal-Madjar, R. Lallement, R. Ferlet, and M. Gerbaldi, "beta pictoris revisited by hipparcos. star properties.," *Astronomy and Astrophysics*, vol. 320, pp. L29–L32, 1997.

[17] E. E. Mamajek and C. P. Bell, "On the age of the β pictoris moving group," *Monthly Notices of the Royal Astronomical Society*, vol. 445, no. 3, pp. 2169–2180, 2014.

[18] B. Zuckerman, I. Song, M. Bessell, and R. Webb, "The β pictoris moving group," *The Astrophysical Journal Letters*, vol. 562, no. 1, p. L87, 2001.

[19] G. Neugebauer, H. Habing, R. van Duinen, H. Aumann, B. Baud, C. Beichman, D. Beintema, N. Boggess, P. Clegg, T. d. Jong, *et al.*, "The infrared astronomical satellite (iras) mission," *Astrophysical Journal*, vol. 278, p. L1, 1984.

[20] F. Paresce, "On the evolutionary status of beta pictoris," *Astronomy and Astrophysics*, vol. 247, pp. L25–L27, 1991.

[21] M. Gerbaldi, J. Zorec, F. Castelli, and R. Faraggiana, "Peculiar vs normal phenomena in a-type stars'," in *ASP Conference Series*, vol. 44, p. 413, 1993.

[22] H. Holweger and I. Rentzsch-Holm, "High-resolution spectroscopy of lambda bootis stars anddusty'normal a stars: circumstellar gas, rotation, and accretion.," *Astronomy and Astrophysics*, vol. 303, p. 819, 1995.

[23] T. Lanz, S. R. Heap, and I. Hubeny, "Hst/ghrs observations of the β pictoris system: Basic parameters and the age of the system," *The Astrophysical Journal Letters*, vol. 447, no. 1, p. L41, 1995.

[24] A. Brunini and O. Benvenuto, "β pictoris: Its evolutionary status," *Monthly Notices of the Royal Astronomical Society*, vol. 283, no. 3, pp. L84–L88, 1996.

[25] V. Ortega, R. De La Reza, E. Jilinski, and B. Bazzanella, "The origin of the β pictoris moving group," *The Astrophysical Journal Letters*, vol. 575, no. 2, p. L75, 2002.

[26] A. Binks and R. Jeffries, "A lithium depletion boundary age of 21 myr for the beta pictoris moving group," *Monthly Notices of the Royal Astronomical Society: Letters*, vol. 438, no. 1, pp. L11–L15, 2013.

[27] D. B. y Navascués, J. R. Stauffer, I. Song, and J.-P. Caillault, "The age of β pictoris," *The Astrophysical Journal Letters*, vol. 520, no. 2, p. L123, 1999.

[28] E. Mentuch, A. Brandeker, M. H. van Kerkwijk, R. Jayawardhana, and P. H. Hauschildt, "Lithium depletion of nearby young stellar associations," *The Astrophysical Journal*, vol. 689, no. 2, p. 1127, 2008.

[29] R. O. Gray, C. Corbally, R. Garrison, M. McFadden, E. Bubar, C. McGahee, A. ODonoghue, and E. Knox, "Contributions to the nearby stars (nstars) project: spectroscopy of stars earlier than m0 within 40 pcthe southern sample," *The Astronomical Journal*, vol. 132, no. 1, p. 161, 2006.

[30] F. Van Leeuwen, "Validation of the new hipparcos reduction," *Astronomy & Astrophysics*, vol. 474, no. 2, pp. 653–664, 2007.

[31] G. Gontcharov, "Pulkovo compilation of radial velocities for 35 495 hipparcos stars in a common system," *Astronomy Letters*, vol. 32, no. 11, pp. 759–771, 2006.

[32] F. Royer, J. Zorec, and A. Gómez, "Rotational velocities of a-type stars-iii. velocity distributions," *Astronomy & Astrophysics*, vol. 463, no. 2, pp. 671–682, 2007.

[33] H. Aumann, "Iras observations of matter around nearby stars.," *Publications of the Astronomical Society of the Pacific*, vol. 97, no. 596, p. 885, 1985.

[34] P. Artymowicz, F. Paresce, and C. Burrows, "The structure of the beta pictoris disk and the properties of its particles," *Advances in Space Research*, vol. 10, no. 3-4, pp. 81–84, 1990.

[35] B. A. Smith and R. J. Terrile, "A circumstellar disk around β pictoris," *Science*, vol. 226, no. 4681, pp. 1421–1424, 1984.

[36] B. Smith and R. Terrile, "The beta pictoris disk: recent optical observations," in *Bulletin of the American Astronomical Society*, vol. 19, p. 829, 1987.

[37] C. Telesco and R. Knacke, "Detection of silicates in the beta pictoris disk," *The Astrophysical Journal*, vol. 372, pp. L29–L31, 1991.

[38] D. Aitken, T. Moore, P. Roche, C. Smith, and C. Wright, "Mid-infrared spectroscopy of beta pictoris: constraints on the dust grain size," *Monthly Notices of the Royal Astronomical Society*, vol. 265, no. 1, pp. L41–L43, 1993.

[39] D. Backman, F. Gillett, and F. Witteborn, "Infrared observations and thermal models of the beta pictoris disk," *The Astrophysical Journal*, vol. 385, pp. 670–679, 1992.

[40] T. Gledhill, S. Scarrott, and R. Wolstencroft, "Optical polarization in the disc around β pictoris," *Monthly Notices of the Royal Astronomical Society*, vol. 252, no. 1, pp. 50P–54P, 1991.

[41] A. Vidal-Madjar, A.-M. Lagrange-Henri, P. Feldman, H. Beust, J. Lissauer, M. Deleuil, R. Ferlet, C. Gry, L. Hobbs, M. McGrath, *et al.*, "Hst-ghrs observations of beta pictoris: additional evidence for infalling comets," *Astronomy and Astrophysics*, vol. 290, pp. 245–258, 1994.

[42] P. Kalas and D. Jewitt, "Asymmetries in the beta pictoris dust disk," *The Astronomical Journal*, vol. 110, p. 794, 1995.

[43] S. R. Heap, D. J. Lindler, T. M. Lanz, R. H. Cornett, I. Hubeny, S. P. Maran, and B. Woodgate, "Space telescope imaging spectrograph coronagraphic observations of β pictoris," *The Astrophysical Journal*, vol. 539, no. 1, p. 435, 2000.

[44] C. M. Telesco, R. S. Fisher, M. C. Wyatt, S. F. Dermott, T. J. Kehoe, S. Novotny, N. Marinas, J. T. Radomski, C. Packham, J. De Buizer, *et al.*, "Mid-infrared images of β pictoris and the possible role of planetesimal collisions in the central disk," *Nature*, vol. 433, no. 7022, p. 133, 2005.

[45] D. Mouillet, J. Larwood, J. Papaloizou, and A. Lagrange, "A planet on an inclined orbit as an explanation of the warp in the β pictoris disc," *Monthly Notices of the Royal Astronomical Society*, vol. 292, no. 4, pp. 896–904, 1997.

[46] J. Larwood and P. Kalas, "Close stellar encounters with planetesimal discs: the dynamics of asymmetry in the β pictoris system," *Monthly Notices of the Royal Astronomical Society*, vol. 323, no. 2, pp. 402–416, 2001.

[47] G. Olofsson, R. Liseau, and A. Brandeker, "Widespread atomic gas emission reveals the rotation of the β pictoris disk," *The Astrophysical Journal Letters*, vol. 563, no. 1, p. L77, 2001.

[48] M. Ahmic, B. Croll, and P. Artymowicz, "Dust distribution in the β pictoris circumstellar disks," *The Astrophysical Journal*, vol. 705, no. 1, p. 529, 2009.

[49] H. Beust, A. Lagrange-Henri, A. V. Madjar, and R. Ferlet, "The beta pictoris circumstellar disk. ix-theoretical results on the infall velocities of ca ii, al iii and mg ii," *Astronomy and Astrophysics*, vol. 223, pp. 304–312, 1989.

[50] A. Lagrange, R. Ferlet, and A. Vidal-Madjar, "The beta pictoris circumstellar disk. iv-redshifted uv lines," *Astronomy and Astrophysics (ISSN 0004-6361), vol. 173, no. 2, Feb. 1987, p. 289-292.*, vol. 173, pp. 289–292, 1987.

[51] H. Beust, A. V. Madjar, A. Lagrange-Henri, and R. Ferlet, "The beta pictoris circumstellar disk. xi-new ca ii absorption features reproduced numerically," *Astronomy and Astrophysics*, vol. 241, pp. 488–492, 1991.

[52] P. Eberhardt, R. Hodges, D. Krankowsky, J. Berthelier, W. Schulte, U. Dolder, P. Lammerzahl, J. Hoffman, and J. Illiano, "The d/h and o18 o16 isotopic ratios in comet halley," in *Lunar and Planetary Science Conference*, vol. 18, 1987.

[53] A.-M. Lagrange, H. Beust, D. Mouillet, M. Deleuil, P. Feldman, R. Ferlet, L. Hobbs, A. Lecavelier Des Etangs, J. Lissauer, M. McGrath, *et al.*, "The beta pictoris circumstellar disk. xxiv. clues to the origin of the stable gas," *Astronomy and Astrophysics*, vol. 330, pp. 1091–1108, 1998.

[54] D. F. Gray, "The observation and analysis of stellar photospheres," *The Observation and Analysis of Stellar Photospheres, by David F. Gray, Cambridge, UK: Cambridge University Press, 2008*, 01 2005.

[55] A.-M. Lagrange, M. Bonnefoy, G. Chauvin, D. Apai, D. Ehrenreich, A. Boccaletti, D. Gratadour, D. Rouan, D. Mouillet, S. Lacour, *et al.*, "A giant planet imaged in the disk of the young star β pictoris," *Science*, p. 1187187, 2010.

[56] P. Artymowicz, "Radiation pressure forces on particles in the beta pictoris system," *The Astrophysical Journal*, vol. 335, pp. L79–L82, 1988.

[57] P. Artymowicz, C. Burrows, and F. Paresce, "The structure of the beta pictoris circumstellar disk from combined iras and coronagraphic observations," *The Astrophysical Journal*, vol. 337, pp. 494–513, 1989.

[58] A. Lecavelier Des Etangs, M. Deleuile, A. Vidal-Madjar, R. N. C. Ferlet, B. Nicolet, and A. Lagrange-Henri, "Vizier online data catalog: Light variations on beta pic (lecavelier des etangs+, 1995)," *VizieR Online Data Catalog*, vol. 329, 1995.

[59] N. Gorkavyi, S. Heap, L. Ozernoy, T. Taidakova, and J. Mather, "Indicator of exo-solar planet (s) in the circumstellar disk around β pictoris," in *Symposium-International Astronomical Union*, vol. 202, pp. 331–334, Cambridge University Press, 2004.

[60] J. Augereau, R. Nelson, A. Lagrange, J. Papaloizou, and D. Mouillet, "Dynamical modeling of large scale asymmetries in the β picto ris dust disk," *Astronomy & Astrophysics*, vol. 370, no. 2, pp. 447–455, 2001.

[61] P. Thébault and H. Beust, "Falling evaporating bodies in the β pictoris system-resonance refilling and long term duration of the phenomenon," *Astronomy & Astrophysics*, vol. 376, no. 2, pp. 621–640, 2001.

[62] H. Beust and A. Morbidelli, "Mean-motion resonances as a source for infalling comets toward β pictoris," *Icarus*, vol. 120, no. 2, pp. 358–370, 1996.

[63] J. Henrard and A. Lemaître, "A mechanism of formation for the kirkwood gaps," *Icarus*, vol. 55, no. 3, pp. 482–494, 1983.

[64] H. Beust and A. Morbidelli, "Falling evaporating bodies as a clue to outline the structure of the β pictoris young planetary system," *Icarus*, vol. 143, no. 1, pp. 170–188, 2000.

[65] Y. K. Okamoto, H. Kataza, M. Honda, T. Yamashita, T. Onaka, J.-i. Watanabe, T. Miyata, S. Sako, T. Fujiyoshi, and I. Sakon, "An early extrasolar planetary system revealed by planetesimal belts in β pictoris," *Nature*, vol. 431, no. 7009, p. 660, 2004.

[66] F. Freistetter, A. V. Krivov, and T. Löhne, "Planets of β pictoris revisited," *Astronomy & Astrophysics*, vol. 466, no. 1, pp. 389–393, 2007.

[67] G. Rousset, F. Lacombe, P. Puget, N. N. Hubin, E. Gendron, T. Fusco, R. Arsenault, J. Charton, P. Feautrier, P. Gigan, *et al.*, "Naos, the first ao system of the vlt: on-sky performance," in *Adaptive Optical System Technologies II*, vol. 4839, pp. 140–150, International Society for Optics and Photonics, 2003.

[68] R. Lenzen, M. Hartung, W. Brandner, G. Finger, N. N. Hubin, F. Lacombe, A.-M. Lagrange, M. D. Lehnert, A. F. Moorwood, and D. Mouillet, "Naos-conica first on

sky results in a variety of observing modes," in *Instrument Design and Performance for Optical/Infrared Ground-based Telescopes*, vol. 4841, pp. 944–953, International Society for Optics and Photonics, 2003.

[69] G. Chauvin, A.-M. Lagrange, H. Beust, M. Bonnefoy, A. Boccaletti, D. Apai, F. Allard, D. Ehrenreich, J. Girard, D. Mouillet, *et al.*, "Orbital characterization of the β pictoris b giant planet," *Astronomy & Astrophysics*, vol. 542, p. A41, 2012.

[70] J. Chilcote, L. Pueyo, R. J. De Rosa, J. Vargas, B. Macintosh, V. P. Bailey, T. Barman, B. Bauman, S. Bruzzone, J. Bulger, *et al.*, "1–2.4 μm near-ir spectrum of the giant planet β pictoris b obtained with the gemini planet imager," *The Astronomical Journal*, vol. 153, no. 4, p. 182, 2017.

[71] A.-M. Lagrange, A. Boccaletti, J. Milli, G. Chauvin, M. Bonnefoy, D. Mouillet, J. Augereau, J. Girard, S. Lacour, and D. Apai, "The position of β pictoris b position relative to the debris disk," *Astronomy & Astrophysics*, vol. 542, p. A40, 2012.

[72] H. Beust, "Falling evaporating bodies in the beta pictoris system." `https://betapic30.sciencesconf.org/data/program/betaPic30proc_HerveBeust.pdf`, note = Accessed: 2018-10-12, September 2014.

[73] J. J. Wang, J. R. Graham, L. Pueyo, P. Kalas, M. A. Millar-Blanchaer, J.-B. Ruffio, R. J. De Rosa, S. M. Ammons, P. Arriaga, V. P. Bailey, *et al.*, "The orbit and transit prospects for β pictoris b constrained with one milliarcsecond astrometry," *The Astronomical Journal*, vol. 152, no. 4, p. 97, 2016.

[74] J. Hearnshaw, S. Barnes, G. Kershaw, N. Frost, G. Graham, R. Ritchie, and G. Nankivell, "The hercules echelle spectrograph at mt. john," *Experimental Astronomy*, vol. 13, no. 2, pp. 59–76, 2002.

[75] S. Barnes, "The design and performance of high resolution échelle spectrographs in astronomy," 2004.

[76] "Applying flat field and dark frame corrections." `http://www.cfht.hawaii.edu/~baril/Pyxis/Help/flatdarkfield.html`. Accessed: 2019-01-09.

[77] "Ccd artifacts." `https://www.eso.org/~ohainaut/ccd/CCD_artifacts.html`. Accessed: 2018-12-01.

[78] D. J. Wright, "Spectroscopic mode identification in a sample of non-radially pulsating stars," 2008.

[79] E. Brunsden, "The music of the stars: Spectroscopy of pulsations in gamma doradus stars," 2013.

[80] A. J. Greenwood, "Spectroscopic analysis of γ doradus variable stars," 2014.

[81] "The atmosphere and observing a guide to astronomical seeing." `http://www.ifa.hawaii.edu/~meech/a281/handouts/seeing.pdf`, note = Accessed: 2018-12-02.

[82] "Barycentric correction." `https://fermi.gsfc.nasa.gov/ssc/data/analysis/documentation/Cicerone/Cicerone_Pulsars/barycentric_correction.html`, note = Accessed: 2018-08-10.

[83] C. E. Moore, "A multiplet table of astrophysical interest-pt. 1: Table of multiplets-pt. 2: Finding list of all lines in the table of multiplets," *NSRDS-NBS, Washington: US Department of Commerce, 1972, Rev. edition*, 1972.

[84] "The gaussian or normal distribution." `https://ned.ipac.caltech.edu/level5/Leo/Stats2_3.html`, note = Accessed: 2019-03-10.

[85] H. Beust, A.-M. Lagrange, F. Plazy, and D. Mouillet, "The beta pictoris circumstellar disk. xxii. investigating the model of multiple cometary infalls.," *Astronomy and Astrophysics*, vol. 310, pp. 181–198, 1996.

[86] R. Heller, D. Williams, D. Kipping, M. A. Limbach, E. Turner, R. Greenberg, T. Sasaki, E. Bolmont, O. Grasset, K. Lewis, *et al.*, "Formation, habitability, and detection of extrasolar moons," *Astrobiology*, vol. 14, no. 9, pp. 798–835, 2014.

[87] R. Stuik, J. Bailey, P. Dorval, G. Talens, I. Laginja, S. Mellon, B. Lomberg, S. Crawford, M. Ireland, E. Mamajek, *et al.*, "bring: An observatory dedicated to monitoring the β pictoris b hill sphere transit," *Astronomy & Astrophysics*, vol. 607, p. A45, 2017.

[88] A. Roberge, P. D. Feldman, A. J. Weinberger, M. Deleuil, and J.-C. Bouret, "The carbon-rich gas in the beta pictoris circumstellar disk," *arXiv preprint astro-ph/0604412*, 2006.

[89] A. Brandeker, "Exposing the gas braking mechanism of the β pictoris disk," *The Astrophysical Journal*, vol. 729, no. 2, p. 122, 2011.

APPENDIX A

Appendix

Table A.1: Table showing the obtained parameters for the different fitted absorptions in the median spectra for all analysed nights across 2017. The acronyms FWHM, R.V and E.W. represent the Full Width at Half Maximum, Radial velocity and Equivalent Width of the absorption. σ represents the uncertainty on the specific value of the parameter. Note that for some of the really poor fits, the uncertainty can be larger than the value of the parameter itself.

Date	Julian Date	Line	Classification	Depth	σ_{Depth}	FWHM	σ_{FWHM}	R.V.	$\sigma_{R.V.}$	EW	$\sigma_{E.W.}$
12th January 2017	J7766	H	p.s.	0.001	0.003	102.501	28.848	-42.600	15.263	0.427	2.037
		K	p.s.	0.030	0.004	102.501	28.848	-42.600	15.263	21.283	6.524
		H	p.b.	0.588	0.012	11.882	0.235	20.363	0.068	48.976	1.395
		K	p.b.	0.585	0.014	11.882	0.235	20.363	0.068	48.745	1.481
		H	p.b.	0.141	0.009	46.480	2.367	22.839	0.586	46.007	3.880
		K	p.b.	0.268	0.014	46.480	2.367	22.839	0.586	87.332	6.307
		H	p.b.	0.009	0.004	41.354	3.982	80.475	1.837	2.581	1.245
		K	p.b.	0.084	0.005	41.354	3.982	80.475	1.837	24.284	2.759
14th January 2017	J7768	H	g.b.	0.692	0.010	13.868	0.185	20.000	0.072	67.299	1.346
		K	g.b.	0.779	0.011	13.868	0.185	20.000	0.072	75.713	1.477
		H	p.b.	0.034	0.004	103.387	3.735	52.877	1.852	24.356	2.809
		K	p.b.	0.125	0.004	103.387	3.735	52.877	1.852	90.331	4.540

Continued on next page

Table A.1 – continued from previous page

15th January 2017	J7769	H	g.s.	0.675	0.012	13.400	89.503	20.023	0.080	63.436	1.469
		K	g.s.	0.747	0.012	13.400	89.503	20.023	0.080	70.221	1.606
		H	p.b.	0.039	0.004	89.503	3.262	47.668	1.647	24.542	2.910
		K	p.b.	0.145	0.005	89.503	3.262	47.668	1.647	91.284	4.683
16th January 2017	J7770	H	p.b.	0.038	0.012	8.643	3.227	-4.763	1.280	2.284	1.107
		K	p.b.	0.008	0.012	8.643	3.227	-4.763	1.280	0.456	0.752
		H	p.b.	0.617	0.010	12.083	0.197	20.422	0.069	52.321	1.206
		K	p.b.	0.613	0.011	12.083	0.197	20.422	0.069	51.976	1.255
		H	g.b.	0.106	0.005	68.112	1.401	31.941	0.734	50.432	2.605
		K	g.b.	0.246	0.006	68.112	1.401	31.941	0.734	117.586	3.705
6th April 2017	J7850	H	g.s.	0.668	0.009	17.844	0.200	23.437	0.082	83.540	1.450
		K	g.s.	0.864	0.010	17.844	0.200	23.437	0.082	108.106	1.703
		H	g.s.	0.038	0.004	63.116	4.532	84.992	1.768	16.704	2.323
		K	g.s.	0.090	0.005	63.116	4.532	84.992	1.768	39.947	3.703
7th April 2017	J7851	H	g.s.	0.054	0.010	8.926	1.506	-7.068	0.640	3.383	0.844
		K	g.s.	0.051	0.010	8.926	1.506	-7.068	0.640	3.182	0.818
		H	g.b.	0.631	0.010	10.831	0.296	20.960	0.167	47.938	1.519

Continued on next page

Table A.1 – continued from previous page

		K	g.b.	0.803	0.011	10.831	0.296	20.960	0.167	60.956	1.876
		H	g.b.	0.350	0.016	8.525	0.387	30.918	0.228	20.918	1.329
		K	g.b.	0.462	0.018	8.525	0.387	30.918	0.228	27.610	1.670
		H	g.b.	0.044	0.005	29.305	4.029	63.207	1.708	8.991	1.637
		K	g.b.	0.087	0.006	29.305	4.029	63.207	1.708	17.929	2.765
		H	g.b.	0.037	0.005	29.319	4.154	98.649	1.991	7.702	1.531
		K	g.b.	0.078	0.006	29.319	4.154	98.649	1.991	16.020	2.592
8th April 2017	J7851	H	p.b.	0.009	0.002	99.309	8.710	-62.675	4.134	5.941	1.414
		K	p.b.	0.041	0.002	99.309	8.710	-62.675	4.134	28.674	3.014
		H	p.b.	0.007	0.006	9.356	2.574	-42.232	0.965	0.431	0.144
		K	p.b.	0.031	0.007	9.356	2.574	-42.232	0.965	2.038	0.721
		H	g.s.	0.082	0.005	14.361	0.817	-7.896	0.277	8.216	0.672
		K	g.s.	0.110	0.006	14.361	0.817	-7.896	0.277	11.059	0.898
		H	g.b.	0.634	0.005	11.828	0.164	20.733	0.075	52.550	0.855
		K	g.b.	0.811	0.006	11.828	0.164	20.733	0.075	67.235	1.073
		H	g.b.	0.270	0.009	7.528	0.225	31.256	0.113	14.261	0.622
		K	g.b.	0.371	0.010	7.528	0.225	31.256	0.113	19.596	0.790
		H	g.s.	0.019	0.002	61.209	2.795	72.146	1.090	8.197	0.995
		K	g.s.	0.084	0.003	61.209	2.795	72.146	1.090	35.965	1.998
9th April 2017	J7851	H	p.s.	0.001	0.005	14.696	5.044	-101.871	2.074	0.078	0.543
		K	p.s.	0.024	0.006	14.696	5.044	-101.871	2.074	2.469	1.080
		H	p.s.	0.003	0.004	21.351	3.340	-72.068	1.247	0.520	0.094

Continued on next page

Table A.1 – continued from previous page

		K	p.s.	0.048	0.006	21.351	3.340	-72.068	1.247	7.125	1.391
		H	p.s.	0.015	0.006	12.260	1.811	-42.258	0.755	1.322	0.541
		K	p.s.	0.056	0.007	12.260	1.811	-42.258	0.755	4.821	0.933
		H	g.b.	0.598	0.007	11.528	0.215	21.410	0.105	48.350	1.056
		K	g.b.	0.766	0.008	11.528	0.215	21.410	0.105	61.904	1.314
		H	g.b.	0.217	0.011	7.446	0.336	31.482	0.175	11.334	0.782
		K	g.b.	0.317	0.013	7.446	0.336	31.482	0.175	16.570	1.014
		H	p.s,	0.042	0.002	72.647	2.275	77.009	0.895	21.587	1.426
		K	p.s.	0.129	0.003	72.647	2.275	77.009	0.895	65.794	2.547
10th April 2017	J7854	H	p.s,	0.005	0.006	18.386	9.988	-70.740	4.182	0.610	0.873
		K	p.s.	0.016	0.007	18.386	9.988	-70.740	4.182	2.014	1.457
		H	p.s,	0.007	0.008	11.157	3.646	-41.167	1.536	0.548	0.648
		K	p.s.	0.034	0.010	11.157	3.646	-41.167	1.536	2.660	1.150
		H	g.b.	0.558	0.010	11.808	0.276	20.988	0.101	46.216	1.360
		K	g.b.	0.703	0.013	11.808	0.276	20.988	0.101	58.221	1.758
		H	g.b.	0.194	0.013	6.772	0.422	32.006	0.190	9.221	0.842
		K	g.b.	0.274	0.015	6.772	0.422	32.006	0.190	12.996	1.068
		H	p.b.	0.112	0.005	44.947	1.814	47.177	0.987	35.296	2.063
		K	p.b.	0.201	0.005	44.947	1.814	47.177	0.987	63.412	3.050
8th May 2017	J7882	H	g.s.	0.555	0.014	14.427	0.297	20.052	0.118	56.169	1.800
		K	g.s.	0.702	0.015	14.427	0.297	20.052	0.118	71.070	2.095
		H	g.b.	0.072	0.020	6.730	1.441	41.054	0.595	3.412	1.180
		K	g.b.	0.098	0.021	6.730	1.441	41.054	0.595	4.613	1.399

Continued on next page

Table A.1 – continued from previous page

		H	p.b.	0.018	0.004	158.994	10.518	78.527	5.138	20.580	4.716
		K	p.b.	0.077	0.005	158.994	10.518	78.527	5.138	85.972	7.831
9th May 2017	J7883	H	g.b.	0.547	0.008	15.564	0.205	19.877	0.074	59.748	1.165
		K	g.b.	0.710	0.010	15.564	0.205	19.877	0.074	77.439	1.461
		H	g.b.	0.034	0.003	78.241	2.901	55.316	1.503	18.810	1.993
		K	g.b.	0.132	0.004	78.241	2.901	55.316	1.503	72.523	3.441
11th May 2017	J7885	H	g.b.	0.577	0.008	13.253	0.170	20.410	0.065	53.627	1.044
		K	g.b.	0.723	0.009	13.253	0.170	20.410	0.065	67.214	1.232
		H	g.b.	0.033	0.003	85.017	2.736	52.534	1.404	19.639	2.035
		K	g.b.	0.129	0.004	85.017	2.736	52.534	1.404	77.130	3.360
12th May 2017	J7886	H	g.s.	0.558	0.008	12.555	0.162	20.845	0.062	49.167	0.950
		K	g.s.	0.758	0.010	12.555	0.162	20.845	0.062	10.131	0.183
		H	p.b.	0.011	0.011	6.057	2.478	41.429	0.884	0.455	0.517
		K	p.b.	0.042	0.014	6.057	2.478	41.429	0.884	1.800	0.946
		H	p.b.	0.074	0.004	54.723	2.098	67.330	0.879	28.241	1.801
		K	p.b.	0.187	0.004	54.723	2.098	67.330	0.879	71.633	3.216
13th May 2017	J7887	H	g.s.	0.010	0.004	21.175	2.383	-34.252	1.012	1.425	0.601

Continued on next page

Table A.1 – continued from previous page

		K	g.s.	0.048	0.005	21.175	2.383	-34.252	1.012	7.101	1.063
		H	g.s.	0.568	0.006	12.111	0.113	21.262	0.041	48.241	0.657
		K	g.s.	0.757	0.007	12.111	0.113	21.262	0.041	64.283	0.840
		H	g.b.	0.076	0.003	46.674	2.320	59.846	0.693	24.846	1.536
		K	g.b.	0.185	0.003	46.674	2.320	59.846	0.693	60.455	3.215
		H	g.b.	0.078	0.004	29.932	1.186	104.452	0.607	16.363	1.018
		K	g.b.	0.167	0.005	29.932	1.186	104.452	0.607	35.007	1.803
14th May 2017	J7888	H	g.b.	0.566	0.010	13.511	0.214	21.501	0.081	53.630	1.265
		K	g.b.	0.739	0.012	13.511	0.214	21.501	0.081	69.979	1.559
		H	p.b.	0.078	0.005	52.557	2.116	62.682	0.811	28.898	2.109
		K	p.b.	0.200	0.006	52.557	2.116	62.682	0.811	73.554	3.626
15th May 2017	J7889	H	p.b.	0.530	0.007	13.858	0.166	21.297	0.059	51.648	1.049
		K	p.b.	0.662	0.008	13.858	0.166	21.297	0.059	64.751	1.264
		H	g.b.	0.089	0.003	65.370	1.451	45.778	0.751	39.933	1.973
		K	g.b.	0.199	0.004	65.370	1.451	45.778	0.751	90.849	3.031
		H	p.s,	0.016	0.003	57.617	5.754	140.110	2.312	9.707	1.734
		K	p.s,	0.045	0.003	57.617	5.754	140.110	2.312	17.845	2.461
18th May 2017	J7892	H	U.D	0.009	0.002	241.847	17.981	-43.238	9.337	15.786	2.901
		K	U.D	0.034	0.002	241.847	17.981	-43.238	9.337	58.328	5.642
		H	g.b.	0.617	0.007	12.402	0.134	22.148	0.047	53.677	0.820

Continued on next page

Table A.1 – continued from previous page

		K	g.b.	0.753	0.009	12.402	0.134	22.148	0.047	65.450	1.027
		H	g.b.	0.027	0.003	55.042	5.733	47.489	2.341	10.402	1.725
		K	g.b.	0.080	0.004	55.042	5.733	47.489	2.341	30.973	3.647
		H	g.b.	0.001	0.005	22.858	5.143	89.422	1.982	0.178	0.805
		K	g.b.	0.037	0.007	22.858	5.143	89.422	1.982	5.954	1.793
5th June 2017	J7910	H	g.s.	0.025	0.011	3.477	1.061	-5.757	0.443	0.600	0.335
		K	g.s.	0.045	0.013	3.477	1.061	-5.757	0.443	1.101	0.460
		H	g.b.	0.667	0.007	12.706	0.157	22.363	0.046	59.407	0.982
		K	g.b.	0.798	0.012	12.706	0.157	22.363	0.046	71.142	1.371
		H	g.b.	0.052	0.004	38.927	2.738	41.459	1.390	14.138	1.476
		K	g.b.	0.116	0.005	38.927	2.738	41.459	1.390	31.778	2.553
		H	g.b.	0.041	0.003	48.773	2.005	105.301	0.786	13.870	1.167
		K	g.b.	0.126	0.004	48.773	2.005	105.301	0.786	42.961	2.153
6th June 2017	J7911	H	p.s.	0.029	0.012	4.672	1.955	-5.003	0.830	0.941	0.546
		K	p.s.	0.017	0.011	4.672	1.955	-5.003	0.830	0.560	0.417
		H	g.s.	0.700	0.007	12.467	0.102	22.221	0.043	61.237	0.768
		K	g.s.	0.858	0.007	12.467	0.102	22.221	0.043	74.995	0.865
		H	g.b.	0.045	0.005	28.722	2.251	56.207	0.846	8.994	1.245
		K	g.b.	0.111	0.008	28.722	2.251	56.207	0.846	22.287	2.380
		H	g.b.	0.071	0.003	60.084	2.718	101.681	1.264	29.990	1.842
		K	g.b.	0.165	0.003	60.084	2.718	101.681	1.264	69.355	3.458

Continued on next page

Table A.1 – continued from previous page

7th June 2017	J7912	H	g.s.	0.703	0.009	11.745	0.123	21.966	0.052	57.861	0.955
		K	g.s.	0.879	0.009	11.745	0.123	21.966	0.052	72.371	1.085
		H	p.s.	0.148	0.004	60.274	1.036	88.461	0.428	62.742	1.944
		K	p.s.	0.271	0.004	60.274	1.036	88.461	0.428	114.676	2.681
8th June 2017	J7913	H	g.s.	0.693	0.007	11.994	0.108	21.589	0.045	58.287	0.817
		K	g.s.	0.859	0.008	11.994	0.108	21.589	0.045	72.266	0.936
		H	g.b.	0.027	0.004	64.252	3.537	83.109	2.511	11.957	2.052
		K	g.b.	0.112	0.006	64.252	3.537	83.109	2.511	50.469	3.907
		H	p.b.	0.044	0.006	25.625	4.043	109.341	1.296	7.848	1.636
		K	p.b.	0.051	0.012	25.625	4.043	109.341	1.296	9.144	2.621
9th June 2017	J7914	H	p.s.	0.015	0.002	120.793	13.270	-78.902	4.740	12.586	2.249
		K	p.s.	0.032	0.002	120.793	13.270	-78.902	4.740	27.142	3.638
		H	g.s.	0.030	0.007	13.720	3.896	-2.838	1.573	2.879	1.068
		K	g.s.	0.007	0.007	13.720	3.896	-2.838	1.573	0.677	0.704
		H	g.s.	0.705	0.007	12.698	0.104	21.403	0.042	62.777	0.786
		K	g.s.	0.870	0.007	12.698	0.104	21.403	0.042	77.429	0.907
		H	g.b.	0.004	0.005	20.113	3.884	52.993	1.533	0.550	0.718
		K	g.b.	0.043	0.007	20.113	3.884	52.993	1.533	6.065	1.493
		H	g.b.	0.039	0.003	52.760	2.355	98.567	0.903	14.539	1.308
		K	g.b.	0.129	0.004	52.760	2.355	98.567	0.903	47.614	2.533

Continued on next page

Table A.1 – continued from previous page

10th June 2017	J7915	H	p.s.	0.015	0.002	152.182	25.000	-34.855	11.158	16.084	3.551
		K	p.s.	0.028	0.002	152.182	25.000	-34.855	11.158	29.622	5.527
		H	g.s.	0.676	0.008	13.003	0.131	21.688	0.050	61.669	0.939
		K	g.s.	0.841	0.008	13.003	0.131	21.688	0.050	76.708	1.091
		H	p.s.	0.061	0.005	42.615	1.736	68.686	0.568	18.141	1.599
		K	p.s.	0.169	0.006	42.615	1.736	68.686	0.568	50.363	2.772
11th June 2017	J7916	H	g.s.	0.718	0.011	12.329	0.164	21.677	0.069	62.059	1.283
		K	g.s.	0.869	0.012	12.329	0.164	21.677	0.069	75.115	1.437
		H	p.s,	0.056	0.005	53.503	2.399	78.525	0.975	21.116	2.139
		K	p.s.	0.157	0.006	53.503	2.399	78.525	0.975	58.825	3.481
13th June 2017	J7918	H	g.s.	0.655	0.018	13.176	0.310	21.951	0.130	60.532	2.210
		K	g.s.	0.835	0.019	13.176	0.310	21.951	0.130	77.144	2.556
		H	p.s.	0.095	0.010	39.458	2.554	63.959	1.009	26.190	3.266
		K	p.s.	0.217	0.012	39.458	2.554	63.959	1.009	60.063	5.076
14th June 2017	J7919	H	g.b.	0.695	0.015	13.917	0.317	22.718	0.146	67.813	5.292
		K	g.b.	0.869	0.018	13.917	0.317	22.718	0.146	84.795	6.589
		H	g.b.	0.246	0.023	25.910	4.510	50.175	2.541	44.621	1.360
		K	g.b.	0.389	0.041	25.910	4.510	50.175	2.541	70.629	2.191

Continued on next page

Table A.1 – continued from previous page

		H	g.b.	0.149	0.047	23.171	6.158	73.170	2.845	24.271	2.940
		K	g.b.	0.273	0.076	23.171	6.158	73.170	2.845	44.286	5.283
		H	g.b.	0.109	0.012	33.194	4.801	101.004	3.052	25.395	1.683
		K	g.b.	0.223	0.016	33.194	4.801	101.004	3.052	51.796	3.239
15th June 2017	J7920	H	p.b.	0.032	0.010	25.019	7.385	10.011	5.728	5.541	2.411
		K	p.b.	0.066	0.014	25.019	7.385	10.011	5.728	11.500	4.223
		H	g.b.	0.707	0.019	12.397	0.269	22.344	0.064	61.443	2.107
		K	g.b.	0.835	0.039	12.397	0.269	22.344	0.064	72.570	3.734
		H	p.s.	0.063	0.003	52.920	1.594	72.548	0.615	23.423	1.419
		K	p.s.	0.173	0.004	52.920	1.594	72.548	0.615	64.296	2.434
3rd July 2017	J7938	H	g.b.	0.255	0.024	9.268	0.455	13.387	0.343	16.597	1.753
		K	g.b.	0.449	0.027	9.268	0.455	13.387	0.343	29.201	2.276
		H	g.b.	0.703	0.012	11.205	0.365	22.765	0.205	55.265	2.034
		K	g.b.	0.831	0.020	11.205	0.365	22.765	0.205	65.293	2.646
		H	g.b.	0.063	0.006	26.326	2.851	47.020	0.917	11.605	1.711
		K	g.b.	0.138	0.011	26.326	2.851	47.020	0.917	25.515	3.393
		H	g.b.	0.071	0.004	46.904	2.944	84.483	1.498	23.393	1.956
		K	g.b.	0.175	0.005	46.904	2.944	84.483	1.498	57.419	3.924
4th July 2017	J7939	H	g.b.	0.267	0.020	9.478	0.464	13.791	0.336	17.768	1.616
		K	g.b.	0.457	0.021	9.478	0.464	13.791	0.336	30.403	2.057

Continued on next page

Table A.1 – continued from previous page

		H	g.b.	0.688	0.013	10.271	0.291	22.849	0.195	49.567	1.703
		K	g.b.	0.744	0.021	10.271	0.291	22.849	0.195	53.556	2.137
		H	g.b.	0.066	0.003	65.414	2.251	56.067	1.016	30.191	1.846
		K	g.b.	0.158	0.004	65.414	2.251	56.067	1.016	72.501	3.034
5th July 2017	J7940	H	g.b.	0.648	0.008	16.031	0.208	20.595	0.066	72.868	1.301
		K	g.b.	0.770	0.011	16.031	0.208	20.595	0.066	86.584	1.664
		H	g.b.	0.073	0.004	56.342	2.149	46.647	1.262	28.668	1.972
		K	g.b.	0.160	0.005	56.342	2.149	46.647	1.262	63.034	3.031
		H	p.s.	0.024	0.004	47.222	4.799	191.980	2.038	8.012	1.545
		K	p.s.	0.047	0.004	47.222	4.799	191.980	2.038	15.474	2.159
6th July 2017	J7941	H	g.b.	0.632	0.010	13.865	0.219	21.191	0.075	61.479	1.371
		K	g.b.	0.743	0.012	13.865	0.219	21.191	0.075	72.261	1.627
		H	g.b.	0.121	0.004	66.495	1.694	55.781	0.819	56.554	2.482
		K	g.b.	0.256	0.005	66.495	1.694	55.781	0.819	119.387	3.774
7th July 2017	J7942	H	g.b.	0.610	0.014	12.428	0.296	20.745	0.094	53.180	1.738
		K	g.b.	0.701	0.017	12.428	0.296	20.745	0.094	61.097	2.108
		H	g.b.	0.184	0.006	47.430	1.473	45.874	0.748	61.080	2.875
		K	g.b.	0.339	0.007	47.430	1.473	45.874	0.748	112.744	4.216

Continued on next page

Table A.1 – continued from previous page

8th July 2017	J7943	H	p.s.	0.725	0.025	12.319	0.349	20.322	0.147	62.618	2.791
		K	p.s.	0.918	0.026	12.319	0.349	20.322	0.147	79.261	3.192
		H	U.D	0.163	0.013	43.388	2.466	70.366	1.010	49.531	4.851
		K	U.D	0.274	0.014	43.388	2.466	70.366	1.010	83.345	6.456
9th July 2017	J7944	H	g.s.	0.690	0.009	13.348	0.143	20.978	0.060	64.549	1.067
		K	g.s.	0.843	0.009	13.348	0.143	20.978	0.060	78.878	1.202
		H	p.s.	0.113	0.005	45.088	1.142	69.542	0.458	35.646	1.690
		K	p.s.	0.237	0.005	45.088	1.142	69.542	0.458	74.833	2.511
13th July 2017	J7948	H	g.b.	0.642	0.008	14.681	0.270	21.961	0.118	66.125	1.483
		K	g.b.	0.813	0.009	14.681	0.270	21.961	0.118	83.651	1.783
		H	g.b.	0.083	0.015	7.170	0.644	33.603	0.272	4.181	0.852
		K	g.b.	0.213	0.017	7.170	0.644	33.603	0.272	10.702	1.271
		H	p.s.	0.033	0.003	95.224	5.527	127.094	2.264	22.295	2.393
		K	p.s.	0.066	0.003	95.224	5.527	127.094	2.264	44.078	3.432
		H	p.s.	0.053	0.024	2.390	1.315	190.478	0.496	0.885	0.632
		K	p.s.	0.012	0.018	2.390	1.315	190.478	0.496	0.201	0.329
14th July 2017	J7949	H	g.b.	0.624	0.008	15.156	0.263	21.465	0.105	66.298	1.457
		K	g.b.	0.743	0.009	15.156	0.263	21.465	0.105	78.969	1.660

Continued on next page

Table A.1 – continued from previous page

		H	g.b.	0.132	0.013	7.464	0.517	34.720	0.223	6.925	0.827
		K	g.b.	0.240	0.014	7.464	0.517	34.720	0.223	12.550	1.129
		H	p.s.	0.013	0.002	225.140	11.339	42.057	4.524	20.155	3.461
		K	p.s.	0.055	0.003	225.140	11.339	42.057	4.524	86.781	6.090
25th July 2017	J7960	H	g.b.	0.675	0.009	13.309	0.198	21.946	0.067	63.012	1.284
		K	g.b.	0.762	0.013	13.309	0.198	21.946	0.067	71.148	1.643
		H	g.b.	0.035	0.005	47.103	2.957	42.612	1.634	11.640	1.827
		K	g.b.	0.127	0.006	47.103	2.957	42.612	1.634	41.814	3.282
		H	g.b.	0.061	0.005	53.564	2.421	125.766	0.965	22.798	2.787
		K	g.b.	0.126	0.005	53.564	2.421	125.766	0.965	47.270	2.787
27th July 2017	J7962	H	g.b.	0.720	0.008	12.919	0.129	21.582	0.051	65.189	0.944
		K	g.b.	0.869	0.008	12.919	0.129	21.582	0.051	78.719	1.057
		H	g.b.	0.028	0.008	9.357	1.171	38.542	0.479	1.864	0.583
		K	g.b.	0.100	0.010	9.357	1.171	38.542	0.479	6.539	1.037
		H	g.b.	0.063	0.003	56.295	1.588	96.708	0.650	25.028	1.499
		K	g.b.	0.158	0.004	56.295	1.588	96.708	0.650	62.547	2.346
28th July 2017	J7963	H	g.b.	0.688	0.008	13.277	0.179	22.007	0.059	64.027	1.163
		K	g.b.	0.782	0.013	13.277	0.179	22.007	0.059	72.786	1.536
		H	g.b.	0.047	0.004	48.259	3.801	47.621	1.500	15.868	1.911
		K	g.b.	0.153	0.005	48.259	3.801	47.621	1.500	51.800	4.399

Continued on next page

Table A.1 – continued from previous page

		H	g.b.	0.022	0.004	38.626	4.632	100.627	2.274	5.863	1.392
		K	g.b.	0.077	0.006	38.626	4.632	100.627	2.274	20.764	2.940
30th July 2017	J7965	H	g.b.	0.735	0.010	12.213	0.158	20.828	0.060	62.950	1.186
		K	g.b.	0.852	0.012	2.183	0.725	20.828	0.060	72.968	1.380
		H	p.b.	0.056	0.022	2.183	0.725	37.453	0.299	0.858	0.440
		K	p.b.	0.083	0.028	70.449	4.709	37.453	0.299	1.278	0.601
		H	g.b.	0.028	0.004	70.449	4.709	69.481	1.928	14.063	2.161
		K	g.b.	0.100	0.005			69.481	1.928	49.510	4.038
31st July 2017	J7966	H	g.b.	0.752	0.008	12.730	0.114	20.867	0.046	67.156	0.910
		K	g.b.	0.894	0.008	12.730	0.114	20.867	0.046	79.784	1.023
		H	p.b.	0.029	0.009	9.136	1.224	40.430	0.468	1.854	0.599
		K	p.b.	0.095	0.011	9.136	1.224	40.430	0.468	6.062	1.057
		H	g.b.	0.049	0.003	62.745	2.467	83.919	0.939	21.472	1.659
		K	g.b.	0.140	0.004	62.745	2.467	83.919	0.939	61.407	2.961
29th Septem-ber 2017	J8026	H	g.b.	0.741	0.006	13.684	0.131	21.215	0.042	71.104	0.906
		K	g.b.	0.853	0.010	13.684	0.131	21.215	0.042	81.868	1.254
		H	g.b.	0.041	0.003	46.567	3.369	46.357	1.301	13.377	1.457
		K	g.b.	0.143	0.004	46.567	3.369	46.357	1.301	46.651	3.595
		H	g.b.	0.068	0.004	33.888	1.559	92.983	0.810	16.171	1.148

Continued on next page

Table A.1 – continued from previous page

		K	g.b.	0.152	0.005	33.888	1.559	92.983	0.810	36.120	2.112
30th September 2017	J8027	H	p.b.	0.699	0.009	16.820	0.201	21.999	0.075	82.475	1.430
		K	p.b.	0.781	0.010	16.820	0.201	21.999	0.075	92.147	1.604
		H	p.b.	0.056	0.004	100.160	2.701	62.890	1.392	39.142	2.675
		K	p.b.	0.167	0.004	100.160	2.701	62.890	1.392	117.586	4.233
4th December 2017	J8092	H	p.s.	0.023	0.003	50.646	4.623	-38.170	1.879	8.183	1.325
		K	p.s.	0.043	0.003	50.646	4.623	-38.170	1.879	15.398	1.871
		H	g.b.	0.715	0.006	13.959	0.135	21.239	0.044	70.035	0.910
		K	g.b.	0.861	0.010	13.959	0.135	21.239	0.044	84.259	1.276
		H	g.b.	0.044	0.003	52.349	8.438	61.442	3.381	16.075	2.845
		K	g.b.	0.135	0.005	52.349	8.438	61.442	3.381	49.556	8.209
		H	g.b.	0.011	0.009	28.307	5.508	96.036	2.167	2.219	1.933
		K	g.b.	0.069	0.025	28.307	5.508	96.036	2.167	13.709	5.582
5th December 2017	J8093	H	p.s.	0.014	0.004	39.157	5.138	-43.656	2.180	3.764	1.103
		K	p.s.	0.035	0.004	39.157	5.138	-43.656	2.180	9.635	1.708
		H	g.b.	0.720	0.006	14.422	0.124	21.379	0.050	72.854	0.906

Continued on next page

Table A.1 – continued from previous page

		K	g.b.	0.885	0.007	14.422	0.124	21.379	0.050	89.530	1.053
		H	g.b.	0.024	0.008	10.781	1.713	40.119	0.519	1.844	0.699
		K	g.b.	0.101	0.016	10.781	1.713	40.119	0.519	7.616	1.710
		H	g.b.	0.038	0.008	32.023	7.819	92.212	7.905	8.473	2.764
		K	g.b.	0.108	0.034	32.023	7.819	92.212	7.905	24.332	9.714
		H	g.b.	0.020	0.007	42.930	9.314			6.083	2.561
		K	g.b.	0.094	0.020	42.930	9.314			28.290	8.551
6th December 2017	J8094	H	p.s.	0.018	0.003	52.891	4.000	-42.161	1.642	6.769	1.140
		K	p.s.	0.050	0.003	52.891	4.000	-42.161	1.642	18.616	1.851
		H	g.b.	0.741	0.006	14.692	0.122	21.407	0.046	76.384	0.863
		K	g.b.	0.890	0.008	14.692	0.122	21.407	0.046	91.654	1.120
		H	g.b.	0.088	0.006	11.157	0.726	40.185	0.272	6.895	0.672
		K	g.b.	0.150	0.009	11.157	0.726	40.185	0.272	11.709	1.036
		H	g.b.	0.012	0.003	70.946	5.534	74.737	2.007	6.000	1.372
		K	g.b.	0.084	0.003	70.946	5.534	74.737	2.007	41.620	3.616
		H	p.s.	0.006	0.002	213.605	86.995	276.903	30.795	8.837	4.314
		K	p.s.	0.016	0.002	213.605	86.995	276.903	30.795	23.308	9.891
7th December 2017	J8095	H	p.s.	0.017	0.003	46.564	5.272	-47.194	2.200	5.409	1.242
		K	p.s.	0.041	0.004	46.564	5.272	-47.194	2.200	13.516	2.000

Continued on next page

Table A.1 – continued from previous page

		H	g.b.	0.797	0.006	14.557	0.110	20.629	0.041	81.337	0.896
		K	g.b.	0.914	0.007	14.557	0.110	20.629	0.041	93.282	1.030
		H	p.b.	0.018	0.002	126.838	6.341	86.576	2.570	15.892	1.967
		K	p.b.	0.075	0.002	126.838	6.341	86.576	2.570	66.615	3.973
9 th December 2017	J8097	H	p.s.	0.013	0.002	191.770	29.370	-39.161	11.840	16.987	5.284
		K	p.s.	0.035	0.003	191.770	29.370	-39.161	11.840	1.819	2.552
		H	g.s.	0.735	0.008	16.067	0.153	20.191	0.056	83.161	1.327
		K	g.s.	0.883	0.009	16.067	0.153	20.191	0.056	97.646	1.298
		H	p.s.	0.016	0.002	148.488	19.008	222.993	6.710	23.428	8.281
		K	p.s.	0.033	0.003	148.488	19.008	222.993	6.710	5.348	9.229